1984

Trace detection in gases using photoacoustic spectroscopy and Fabry-perot interferometry

Bernard Cheuk-Yuen Yip
Iowa State University

INFORMATION TO USERS

This reproduction was made from a copy of a document sent to us for microfilming. While the most advanced technology has been used to photograph and reproduce this document, the quality of the reproduction is heavily dependent upon the quality of the material submitted.

The following explanation of techniques is provided to help clarify markings or notations which may appear on this reproduction.

1. The sign or "target" for pages apparently lacking from the document photographed is "Missing Page(s)". If it was possible to obtain the missing page(s) or section, they are spliced into the film along with adjacent pages. This may have necessitated cutting through an image and duplicating adjacent pages to assure complete continuity.

2. When an image on the film is obliterated with a round black mark, it is an indication of either blurred copy because of movement during exposure, duplicate copy, or copyrighted materials that should not have been filmed. For blurred pages, a good image of the page can be found in the adjacent frame. If copyrighted materials were deleted, a target note will appear listing the pages in the adjacent frame.

3. When a map, drawing or chart, etc., is part of the material being photographed, a definite method of "sectioning" the material has been followed. It is customary to begin filming at the upper left hand corner of a large sheet and to continue from left to right in equal sections with small overlaps. If necessary, sectioning is continued again -beginning below the first row and continuing on until complete.

4. For illustrations that cannot be satisfactorily reproduced by xerographic means, photographic prints can be purchased at additional cost and inserted into your xerographic copy. These prints are available upon request from the Dissertations Customer Services Department.

5. Some pages in any document may have indistinct print. In all cases the best available copy has been filmed.

University Microfilms International
300 N. Zeeb Road
Ann Arbor, MI 48106

Yip, Bernard Cheuk-Yuen

TRACE DETECTION IN GASES USING PHOTOACOUSTIC SPECTROSCOPY AND FABRY-PEROT INTERFEROMETRY

Iowa State University PH.D. 1984

PLEASE NOTE:

In all cases this material has been filmed in the best possible way from the available copy. Problems encountered with this document have been identified here with a check mark ✓.

1. Glossy photographs or pages _____
2. Colored illustrations, paper or print _____
3. Photographs with dark background ✓
4. Illustrations are poor copy _____
5. Pages with black marks, not original copy _____
6. Print shows through as there is text on both sides of page _____
7. Indistinct, broken or small print on several pages ✓
8. Print exceeds margin requirements _____
9. Tightly bound copy with print lost in spine _____
10. Computer printout pages with indistinct print _____
11. Page(s) _____ lacking when material received, and not available from school or author.
12. Page(s) _____ seem to be missing in numbering only as text follows.
13. Two pages numbered _____. Text follows.
14. Curling and wrinkled pages _____
15. Dissertation contains pages with print at a slant, filmed as received _____
16. Other _____

_____

_____

Trace detection in gases using photoacoustic spectroscopy and Fabry-perot interferometry

by

Bernard Cheuk-Yuen Yip

A Dissertation Submitted to the
Graduate Faculty in Partial Fulfillment of the
Requirements for the Degree of
DOCTOR OF PHILOSOPHY

Department: Chemistry
Major: Analytical Chemistry

Approved:

Signature was redacted for privacy.

In Charge of Major Work

Signature was redacted for privacy.

For the Major Department

Signature was redacted for privacy.

For the Graduate College

Iowa State University
Ames, Iowa

1984

TABLE OF CONTENTS

		Page
I.	INTRODUCTION	1
	A. Air Pollution and its Effect on the Environment	2
	B. Survey of Current Methodology on Air Analysis	5
	1. Chemical methods	5
	2. Physical methods	7
	3. Nonlaser-based techniques	7
	4. Properties of lasers as related to atmospheric analysis	10
	5. Types of lasers used in atmospheric monitoring	11
	6. Laser-based techniques	20
	C. Conclusion	30
II.	PHOTOACOUSTIC DETECTION OF GASEOUS AIR POLLUTANTS	31
	A. Historical Background	31
	B. Theory	33
	C. Noise Considerations	47
	D. Background Signal Consideration	50
	E. Background Signal Reduction	54
	1. Cell design approach	54
	2. Different techniques for modulation	61
	F. Conclusion	67
III.	PHOTOACOUSTIC SPECTROSCOPY IN GASES BASED ON WAVELENGTH MODULATION	68
	A. Introduction	68
	B. Experimental	74
	1. Laser and wavelength modulation	74
	2. PAS cell	81
	3. Gas handling	86

		Page
	C. Results and Discussion	87
	1. Extent of modulation	87
	2. Improvement in the detection limit	103
	3. Deviations from unit slope	106
	D. Conclusion	107
IV.	TRACE DETECTION IN GASES BY FABRY-PEROT INTERFEROMETRY	109
	A. Introduction	109
	B. Interferometry	114
	C. Fabry-Perot Interferometer	123
	1. Finesse	124
	2. Throughput or transmission	129
	3. Detectability of FP interferometry	130
	4. FP as an absorption detector	132
	5. Noise considerations	134
	D. Experiment Based on Dual-Beam Fabry-Perot Interferometry for Gas Detection	137
	1. Experimental section	137
	2. Results and discussion	144
	3. Conclusion	147
	E. Single-beam Fabry-Perot Interferometry for Gas Detection	149
	1. Experimental section	153
	2. Results and discussion	159
	F. Conclusion	172
V.	CONCLUSION	173
VI.	BIBLIOGRAPHY	176
VII.	ACKNOWLEDGEMENTS	189
VIII.	APPENDIX: COMPUTER PROGRAMS USED	190

LIST OF FIGURES

		Page
Figure 1.	Diagram of a typical lead-salt semiconductor diode laser. The dashed line shows the position of the p-n junction (63)	14
Figure 2.	Schematic representation of a spin-flip Raman laser. B is the magnetic field	16
Figure 3.	Frequency shifts of Q-branch of vibrational-rotational Raman spectra of typical molecules present in ordinary and polluted atmosphere relative to the exciting laser frequency (99)	21
Figure 4.	Schematic representation of the photoacoustic effect. τ_c- collisional lifetime; τ_r- radiative lifetime	34
Figure 5.	Typical instrumental set-up of a spectrophone. C-chopper; L- focusing lens	36
Figure 6.	Generation of pressure signal. (A) Time fluctuating mean radiation power in the cell. (B) Time fluctuating pressure in the cell produced by absorption of the radiation shown in (A). I-power; P = pressure signal; t_r-rise time; T-period time (127)	38
Figure 7.	Photoacoustic signal as a function of the pressure inside the cell for 10 torr of CH_4 in various nonabsorbing gases. Solid lines are the theoretical predictions of equation (2.7). Modulation frequency is 50 Hz (158)	44
Figure 8.	Photoacoustic signal as a function of modulation frequency for 10 torr CH_4 in H_2. Solid lines are the theoretical predictions of equation (2.7) (158)	48
Figure 9.	Absorption model for window heating background	52
Figure 10.	PAS cell design for background reduction (127). (A) Two-cell detector; (B) Two-path detector	55

		Page
Figure 11.	Longitudinal, azimuthal, and radial modes of a cylindrical sample chamber	59
Figure 12.	Schematic representation of the set-up for the PAS experiment. HV-high voltage operational amplifier; WG-wave generator; LIA-lock-in amplifier; L1, L2-focusing lenses; S- sample cell; R- reference cell; BS- beam splitter; SA- Spectrum analyzer; T- thermopile; C- Chopper, optional	75
Figure 13.	CO_2 laser energy levels	77
Figure 14.	CO_2 laser gain curve	79
Figure 15.	Schematic representation of the vibrating grating mount. X-horizontal movement; Y-vertical length from center; $\Delta\theta$-angular movement	80
Figure 16.	Mechanical arrangement for wavelength modulation. P1-piezoelectric pusher; P2-coarse adjustment screw; G-grating; L-laser cavity; B-ball bearing	82
Figure 17.	Photoacoustic cell. A through D-vacuum stopcocks; J-o-ring glass joint; F-flexible stainless steel coupling; M-microphone	83
Figure 18.	The dimensions, wiring and sensitivity curve of the Knowles BT-1759 electret microphone	85
Figure 19.	Comparison of photoacoustic signals. A,B. Photoacoustic signal for C_2H_4/N_2 mixtures. Lock-in amplifier output for A) 4.3 ppm B) .90 ppm. Left -amplitude modulation; Right -wavelength modulation	89
Figure 19.	Comparison of photoacoustic signals. C,D. Photoacoustic signal for C_2H_4/N_2 mixtures. Lock-in amplifier output for C) .53 ppm D) .17 ppm. Left -amplitude modulation; Right -wavelength modulation	90
Figure 19.	Comparison of photoacoustic signals. E,F. Photoacoustic signal for C_2H_4/N_2 mixtures. Lock-in amplifier output for E) .076 ppm F) .040 ppm. Left -amplitude modulation; Right -wavelength modulation	91

Page

Figure 20. Schematic representation of wavelength modulation. (A) Modulation waveform; BIAS-DC bias voltage level; V-AC modulation voltage, (B) Resultant CO_2 laser output, assuming 100% modulation 93

Figure 21. Approximation of a square wave by summation of a few sinusoidal components. A-sin(ωt); B-sin(ωt) + 1/3sin(3ωt); C-sin(ωt) + 1/3sin(3ωt) + 1/5sin(5ωt); D-sin(ωt) + 1/3sin(3ωt) + 1/5sin(5ωt) + 1/7sin(7ωt) 96

Figure 22. Trapezoidal waveform used in this study; BIAS - DC bias voltage level; V-Ac modulation voltage 97

Figure 23. Two-cell configuration; L-focusing lens; F-focal point. The sample and reference cells are symmetrical with respect to F 99

Figure 24. Comparison of wavelength modulation signal a) P(14)-P(12) b) P(22)P(20). Sample: 10 ppm C_2H_4/N_2 102

Figure 25. Analytical working curve for amplitude modulation 104

Figure 26. Analytical working curve for wavelength modulation 105

Figure 27. Schematic representations of some thermooptic-based methods. a) Experimental set-up for photothermal deflection detection. SM-spherical mirror; M_1, M_2 - steering mirrors; PD-position detector; LIA - lock-in amplifier (204). b) Optical system for detecting the thremal lens effect. A sample cell is placed a distance Z_1, from the beam waist O. Z_2 indicates the distance between the cell and a pin-hole, which samples the intensity at the beam center I_{bc}. The spot size of the beam at the waist, sample cell, the pinhole are W_0, W_1, W_2, respectively (194) 112

Figure 29. Schematic representations of several types of interferometers. A) Michelson interferometer B) Mach-Zender interferometer, BS-beam splitter; M-plane mirror C) Jamin interferometer. G1, G2 - gas chambers; C1, C2 - compensators; M1, M2 - equally thick plane parallel glass plates of the same refractive index, opaquely silvered on one surface 116

Page

Figure 29. Superposition of waves in a Michelson interferometer. A) Constructive interference when path difference is zero. B) Destructive interference when path difference is $\lambda/2$. C) Constructive interference when path difference is 121

Figure 30. The Fabry-Perot interferometer. A) Multiple reflections within the Fabry-Perot cavity. The actual reflections are not separated in space, as shown, but move back and forth upon themselves, in a manner which cannot be drawn clearly. B) Upper: linear voltage ramp supplied to the scanning mirror. Lower: resultant interference fringe pattern, Finesse = W/w 123

Figure 31. Intensity contours of fringes due to multiple reflections as a function of reflectivity. a) reflectivity = 4% b) reflectivity = 50% c) reflectivity 80%. I_t - percent intensity transmitted; I_r - percent intensity reflected (220) 127

Figure 32. Reflectivity finesse vs. reflectivity (220) 128

Figure 33. Throughput vs. reflectivity as a function of absorption (A) 0.1% absorption (B) 0.2% absorption (C) 0.5% absorption (D) 1.0% absorption (220) 131

Figure 34. Schematic of the set-up for the dual-beam Fabry-Perot experiment. S-mechanical shutter; F1, F2 - optical flats; PMT1, PMT2 - photomultiplier tubes, FP-Fabry-Perot interferometer 138

Figure 35. Brewster's angle arrangement. M-Fabry-Perot interferometer mirrors; OF - optical flat made of BaF_2. θ-Brewster's angle 141

Figure 36. Transient temperature rise and decay model. T_0 - time when the shutter is opened; T_1 - first time delay; T_2 - second time delay. T_1 and T_2 are varied empirically to yield maximum change in terms of temperature, ΔY 143

Page

Figure 37. Oscilloscope display of the dual-beam Fabry-Perot interference fringe pattern. Horizontal scale = 10 ms/cm. Vertical scale = 2.0 v/cm 145

Figure 38. A diagram depicting the generation of a modulated signal in the single-beam Fabry-Perot experiment. FP represents the optimum point of operation at half maximum of a peak slope. PMT represents the corresponding signal observed by the photo-multiplier tube. I- light intensity at half maximum; ΔI- instantaneous change in light intensity due to peak shift; V- initial DC output of the photomultiplier tube; ΔV- AC component corresponding to ΔI 152

Figure 39. Schematic of the set-up for the single-beam Fabry-Perot experiment with position stabilization feedback system. C - chopper, optional; BS - beam splitter; FP - Fabry-Perot interferometer; PD - photo-diode; PMT - photomultiplier tube 154

Figure 40. Schematic of the position stabilization circuit 157

Figure 41. Oscilloscope display of the reduction of the 120 Hz interference by the feedback system. a) No feedback. b) Feedback on. Horizontal scale: 5 ms/cm. Vertical scale: 0.2 V/cm 162

Figure 42. Oscilloscope display of the modulation signal. a) N_2 flown into the chamber. b) C_2H_4/N_2 (~500 ppm) flown into the chamber. Modulation frequency: 100 Hz. Power = 2.5 W. Horizontal scale: 10 ms/cm. Vertical scale: 0.2 V/cm. Note: upper trace corresponds to zero output of PMT 163

Page

Figure 43. Noise profile reduction. a) Background signal plus noise profile with no vibration and acoustic isolation. Sensitivity: 500 mV full scale (F.S.). b) Background signal plus noise with CO_2 laser isolated from the bench. Sensitivity: 500 mV F.S. c) Background plus noise with the experimental set-up isolated by air mattress from the CO_2 laser. Sensitivity: 50 mV F.S. d) Background plus noise with the set-up on a different bench. Sensitivity: 20 mV F.S. e) Noise profile with sound proof box. Sensitivity: 20 mV F.S. f) Best noise profile obtained at 3:00 a.m. Friday morning. Sensitivity: 20 mV F.S. 167

LIST OF TABLES

		Page
Table 1.	Operating characteristics of lasers commonly used in air pollutant monitoring	12
Table 2A.	Representative gases suitable for quantitative Stark spectroscopy	65
Table 2B.	Representative gases suitable for quantitative Zeeman spectroscopy	66
Table 3.	Experimental components for photoacoustic detection based on wavelength modulation	76
Table 4.	List of absorption coefficients of ethylene at CO_2 laser wavelengths used in this study	88
Table 5.	PAS signal normalized for laser power	88
Table 6.	Components for dual-beam Fabry-Perot experiment	139
Table 7.	Components for single-beam Fabry-Perot experiment	155

I. INTRODUCTION

Global attention to the environment during the past two decades has vaulted the term "environmental pollution" from relative obscurity to the limelight. This is reflected in the steady growth in the quantity of published literature (1-12), both in the U.S. and around the world on the subject since 1963. The passage of the Clean Air Act of 1970 and its subsequent amendment by the U.S. Congress has helped accentuate the vigor with which the environmental movement has forged ahead. The general public's awareness and understanding of mankind's impact on our environment have led to the inevitable conclusion that in order to preserve the living quality on earth, it is important to control and reduce the relentless onslaught made on the environment by increased industrial activities (5). This task is by no means a trivial one, and in recent years has been compounded by the development of new sources of energy.

One of the suggested solutions to allay the problem was made by the American Chemical Society's Committee on Environmental Improvement in 1978, was to strive for "continued improvement in the analytical chemical methods needed to monitor, control and study the environment" (13). Such analytical chemical methods must be able to meet the need for accuracy (14), have sufficient sensitivity to detect typical ambient concentrations of common pollutants (15) and be relatively simple to use (16).

It is with this philosophy as the backdrop that two analytical detection systems, one based on photoacoustic effects, the other on Fabry-Perot interferometry were explored and studied. The purpose of this research is to develop new analytical methods for monitoring gaseous pollutants by taking advantage of certain characteristics of photoacoustic spectrometry (PAS), Fabry-Perot interferometry (FPI), and wavelength modulation.

A brief introduction on air pollution and its effects on the environment, and a survey of current methods in measuring and monitoring air pollutants with special emphasis on those that are based on lasers will be presented in this chapter.

A. Air Pollution and its Effect on the Environment

Since the bulk of man-made and natural pollutants are either in the form of gases, solid particulates, or liquid aerosols emitted to the atmosphere, it stands to reason that much of the effort and attention to curtail environmental pollution has been concentrated on air pollutants. Of the various forms of air pollutants, gaseous pollutants constitute 90% of the total mass, while particulates and aerosols make up the remaining 10% (8,11-13,17). Most of the substances originate primarily from the combustion of fuels and waste materials. For example, the burning of sulfur containing fuel is responsible for sulfur dioxide emission, and motor vehicles account for most of the carbon monoxide and hydrocarbon emissions in the atmosphere. A small percentage of air

pollutants do come from natural sources. For example, an estimated 1% of the sulfur dioxide that enters the atmosphere is produced by volcanic eruption (15).

Once in the atmosphere, the subsequent pathways taken by these pollutants vary. Some may travel through the air and disperse. Some may react among themselves and with other substances both chemically and physically. It is the various pathways taken by these pollutants that ultimately determines the effects of air pollution on our environment.

A prime example of air pollutants reacting chemically to affect our atmosphere is the production of smog via a photochemical cycle involving nitrogen dioxide, nitric oxide, and ozone. The cycle is initiated by the dissociation of nitrogen dioxide by sunlight into an oxygen atom and nitric oxide. The oxygen atom reacts rapidly with molecular oxygen (O_2) to form ozone (O_3), which in turn reacts rapidly with nitric oxide to form nitrogen dioxide again. This reaction cycle by itself does not change the relative concentrations of the three reactants, nitric oxide, nitrogen dioxide, and ozone. When hydrocarbons are present (exhaust from automobiles), however, they enter the reaction scheme via a hydroxyl radical (HO) chain to effect a net conversion of nitric oxide to nitrogen dioxide with a concomitant build up of ozone, a telling characteristic of smog.

The presence of yet another pollutant, ammonia, speeds the atmospheric sulfate production (18). It also combines with nitrate to form ultrafine particles which not only causes an acidic precipitate (19) but also reduces visibility.

In addition to these direct adverse effects, air pollution can also exert its toll on our long term climatic trends. Chlorofluorocarbon, e.g. freons, deplete the stratospheric ozone layer (20,21,22) which protects living matter from excessive exposure to ultraviolet rays (23). Carbon dioxide, a normally nontoxic gas, can play havoc in the global temperature balance if too much of it is released into the atmosphere through extensive burning of fossil fuels (24). The so-called "greenhouse effect" caused by an increase in the atmospheric level of carbon dioxide tends to reduce the amount of energy radiated by the earth into the outer space. As a result, the overall global temperature rises. It has been pointed out that even a relatively small increase in average global temperature could be detrimental to the well-being of the human race. The disruption of the food production cycle and the melting of ice in the arctic poles to the point that flooding can occur in a large part of the world are two of the most ominous consequences.

Finally, there is the aspect of health hazards presented by some air pollutants, such as CO, H_2S, NH_3, SO_2, NO, and various mercaptans because of their toxic nature. Other pollutants, such as polycyclic aromatic hydrocarbons, aromatic amines, nitrosamines and vinyl chloride, are carcinogens or potential carcinogens (5). In addition to the adverse effects on human health, these pollutants may also cause deterioration of textiles, corrosion of metals and building materials and damage to vegetation (4,5,8,12).

The preceding passages give a brief glimpse into the direct effects of air pollutants on our environment. However, to fully appreciate the scope of air pollution, one must also have an understanding of the correlation between the sources of pollutants and their respective receptors (25). This involves studying such physical processes as transport, diffusion, and dispersion of the pollutants through the atmosphere. Various mathematical models have been formulated (26,27) to calculate the distribution and concentrations of ambient pollutants in local areas. Such models have made it possible to predict emission limits for various sources in consonance with changing conditions so as to achieve the desired air quality at minimum cost.

B. Survey of Current Methodology on Air Analysis

Current analytical techniques for gaseous air pollutant monitoring and analysis can be classified into two categories, chemical and physical methods (28).

1. Chemical methods

Air pollution analysis based on chemical methods utilize the chemical properties of the species to be analyzed. These include such varied areas as colorimetry, acidimetry, and electrochemistry. For example, Brodelius and Smith (29) have developed a procedure which involves bubbling compressed nitrogen through an aqueous sulfide solution to displace H_2S which is then collected in a glass bead concentration column and measured colorimetrically. To permit accurate determination

of H_2S, strict control of temperature and pH must be observed. A simultaneous detection scheme for SO_2, NO, and NO_2 in air based on pulse polarography has been developed by Bruno et al. (30). Detection limits as low as 7 ul/m^3 for SO_2 and about 50 ul/m^3 for NO_2 were reported. Still another example of a chemical method for the analysis of air pollutants is the Reference Method promulgated by the Environmental Protection Agency for measuring NO_2 in the atmosphere (31). The method involves first bubbling air through a sodium hydroxide solution. Nitrogen dioxide in the air reacts to form a stable solution of sodium nitrite and this reaction product is subsequently measured by standard titrimetric techniques.

Generally speaking, these chemical methods suffer one distinct disadvantage, the need for sample collection and preconcentration steps (29-32). Such steps have to be well designed in order to obtain quantitatively representative results. Besides, a sampling step can be time-consuming and hence render continuous monitoring difficult. Another disadvantage with wet chemical methods is the difficulty in controlling such reaction variables as pH, temperature, reaction kinetics, etc. A case in point is the last example cited in the preceding paragraph. The reaction efficiency between NO_2 and the NaOH solution is strongly concentration dependent. It is believed that only 35% of the NO_2 in the air reacted with the solution when the NO_2 concentration was at the ambient trace level. As a result, this scheme was withdrawn by the EPA as a Reference Method (33).

2. Physical methods

The thrust in air pollution monitoring in recent years is toward physical techniques. These techniques involve direct measurements of the physical properties of either the pollutants themselves, or following their interactions with other compounds. In general, they have the advantage of avoiding the problem of sample handling. That is, sometimes the pollutant can be monitored *in situ*. A specific class of physical techniques - optical techniques - looms very large in the annals of air pollution analysis. They offer several interesting advantages (16), one of which is the possibility of remote or long path measurements. Since laser-based optical techniques for air pollution analysis constitute the bulk of this chapter, their discussion will be deferred till later.

3. Nonlaser-based techniques

A brief survey and discussion on nonlaser-based techniques for air pollution analysis is in order here to complete the presentation. They include chromatographic methods, chemiluminescence, fluorescence, absorption spectrometry, and mass spectrometry.

a. Gas chromatography Gas chromatography (GC) is by far the most widely used analytical technique for organic atmospheric pollutants. Different detection schemes based on GC have been developed with varying degrees of success (34-38). Unfortunately, they all suffer one disadvantage, sensitivity is not high enough to measure ambient level pollutants without sample preconcentration, which will then introduce additional errors and make continuous monitoring difficult.

In recent years, combining GC with detectors other than the conventional ones, i.e. the electron capture detector and the flame ionization detector, has gained in popularity. This is largely due to technological advances made in these detectors in the past decade. Heading the line of GC-interfaced detection schemes is GC-mass spectrometry (GC/MS). This combination has been used for analyses of complex air pollutant mixtures. Pellizzari described application of GC/MS to the analysis of vapor phase organics in ambient air near industrial sites (39). Other classes of organic pollutants measured by GC/MS include polyhalogenated hydrocarbons (40), and airborne phthalates (41). Once again, the need for a preconcentration step has made these schemes less than desirable for continuous monitoring purposes.

b. Chemiluminescence Chemiluminescence refers to the emission of light due to a chemical reaction (42). When an exoenergetic chemical reaction occurs, one of the product molecules may be left in an excited state which decays to a lower energy state by emitting a photon. The emitted light may have a characteristic spectrum. With proper optical detectors, the emitted photons can be quantitatively monitored. Several common air pollutants, such as organic sulfides (43) and nitrogen oxides (NO, NO_2) (44) have been successfully detected by chemiluminescence analyzers. A detection limit of sub-part-per billion (ppb) has been obtained (28). A chemiluminescence detector for the selective monitoring of H_2S and CH_3SH has been developed by Yeung and Spurlin (45).

This detector, which is based upon the room temperature, reduced-pressure reaction with the reagent ClO_2 has the added attractive feature of being capable of on-line measurement.

Chemiluminescence methods have several advantages. The reactions are usually specific and detectability is generally good enough to allow measurement at ambient pollutant levels. A major disadvantage is that a reagent is still necessary.

c. Miscellaneous There are numerous other methods for air pollution analysis currently being used. For example, SO_2 can be detected by flame photometry (46), and by fluorescence photometry using conventional ultra-violet light sources (47). It is beyond the scope of this chapter to delve into each of them. However, one particular class of detectors is worth mentioning before proceeding to the discussion of laser-based techniques.

Detectors based on infrared absorption spectrometry using conventional infrared sources have been historically used to measure and to identify the constituents of air pollutants (48). In fact, it was officially recommended by the National Institute for Occupational Safety and Health (NIOSH) for the carbon monoxide measurement in air (49). Today, many commercially available gas analyzers for in-plant measurements are based upon this principle and their sensitivities can reach the 0.02 parts-per-million (ppm) level for some gases with a 20 meter path-length (50).

These automated physical methods are generally precise, accurate and simple. They are, however, limited to single-point measurement and are usually reliable to about 0.01 ppm only. For the monitoring and study of trace gases in the atmosphere at ppb level and below, this sensitivity is far from satisfactory. There is clearly a need to develope new techniques with adequate sensitivity to monitor, control and study the atmosphere.

4. Properties of lasers as related to atmospheric analysis

Optical (spectroscopic) methods as a specific class of physical methods for applications in air pollutant monitoring have attracted a lot of interest since 1970 (51). This is due mainly to the relative simplicity, sensitivity, selectivity, speed of measurement, and the potential of multipollutant detection (16) that are generally offered by these methods. With the advent of laser technology, spectroscopic methods with lasers replacing the conventional incandescent light sources have gained in popularity in the field of pollutant monitoring. Various areas of application, such as remote sensing, pollutant transport monitoring, spatial distribution monitoring, point sensing, etc., all based on laser spectroscopic methods, have been extensively explored (52-55). For routine atmospheric monitoring, it is increasingly clear that laser spectroscopic monitoring technique may be the only answer.

The laser as a source offers several unique properties (52,53,56) that distinguish it from the conventional optical source: (1) the extremely coherent and unidirectional nature of the radiation, (2) the

high power over a small spectral region, (3) the monochromaticity coupled with fine tuning ability, and (4) the low divergence of the beam which makes spatial collimation very easy to accomplish.

Most laser monitoring techniques take full advantage of these properties in their measurements. Because of coherence and spatial collimation, long path measurement (16) and remote sensing (57,58) of the atmosphere are possible. The high power guarantees detectability (59) which is needed for the trace level analysis of common ambient pollutants (13). The monochromaticity coupled with a fine tuning ability ensures selectivity (60).

Another feature that makes the laser as a source for air pollutant monitoring attractive is the range of output wavelengths provided by commercial IR lasers. It spans the 2-20 um of the IR spectrum, the so-called "fingerprint" region where most atmospheric pollutant gases have strong characteristic absorption lines. It is therefore not surprising that IR lasers have attracted great attention for their uses in atmospheric monitoring techniques.

5. Types of lasers used in atmospheric monitoring

Before proceeding to survey the various laser-based techniques for atmospheric monitoring, a brief discussion on the types of lasers now commonly used will be presented here. The operating characteristics of each of these are presented in Table 1.

Tunable diode lasers, arguably the most widely used infrared lasers for line parameter studies of gaseous pollutants, are also called semiconductor diode lasers (SDL). They are made of semiconductor

Table 1. Operating characteristics of lasers commonly used in air pollutant monitoring

Source	Wavelength Region		Highest Resolution (cm^{-1})	Typical Power (W)	
	overall (m)	continuous (cm^{-1})		cw	pulsed
Diode laser	1-34	2	3×10^{-6}	10^{-3}	10
SFR laser	3(HF-pumped)	15		1	10^{-3}
	5-6(CO-pumped)	50	1×10^{-6}		
	9-14(CO-pumped)2	100	3×10^{-5}		
HPG	9-11(CO_2)	10	3×10^{-2}		10^5
OPO	0.55-3.5($LiNbO_3$)	3000	1×10^{-3}	10^{-2}	10^5
	1.2-8.5 (Ag_3AsS_3)				
	8-12(CdSe)				
OM	2-4(dye laser and argon laser in $LiNbO_3$)	1	5×10^{-6}	10^{-3}	10^3
Dye laser	0.34-1.2	1×10^5	3×10^{-4}	10^{-1}	10^8
Color-center laser	0.88-3.3	500	10^{-5}	10^{-2}	
Low pressure gas laser	5.1-6.5(CO)				
	9.2-9.8, 10.1-10.9(CO_2)		1×10^{-3}	10	

diodes, and include binary compounds such as InSb, InAs, GaSb, PbSe, PbS, PbTe, and pseudo-binary alloys such as $Pb_{1-x}Sn_xTe$, $PbS_{1-x}Se_x$, $Pb_{1-x}Se_x$, $Pb_{1-x}Sn_xSe$, $GaAs_xSb_{1-x}$, $Hg_{1-x}Cd_xTe$, and $In_{1-x}Ga_xAs$. Among them, the lead-salt diode lasers (Figure 1) are the most useful in pollution monitoring. Detailed discussions on their operational principles and characteristics can be found in recent review articles (61-63). Only the basics as related to atmospheric monitoring will be discussed here.

Diode (semiconductor) lasers operate by stimulating emission across the gap between conduction and valence bands. Population inversion is achieved by electron injection across the band gap either with an electrical current, by optical pumping, or electron-beam excitation. Most diode lasers emit radiation in several modes whose infrared frequency increases with an increase in the driving current (64). The continuous tuning range of a single mode typically spans from 0.5 to several cm^{-1}, and is achieved by changing the chemical composition, temperature, applied pressure, magnetic field, or injection current (65).

The diode laser linewidth is extremely narrow. Hinkley and Freed (66) reported linewidths as narrow as 54 KH_z (1.8×10^{-6} cm^{-1}) by heterodyning a $Pb_{0.88}Sn_{0.12}Te$ laser, operating cw at 10.6 um, with a stabilized single frequency CO_2 gas laser. Because of this characteristic diode lasers have been successfully used for line parameter studies of gaseous pollutants (67). Other applications include the

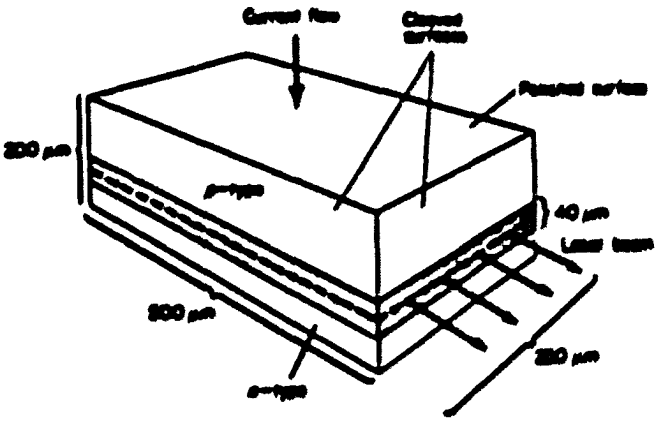

Figure 1. Diagram of a typical lead-salt semiconductor diode laser. The dashed line shows the position of the p-n junction (63)

detection of CO, NO, C_2H_4, and H_2O in samples of automobile exhaust (68-70) both at ambient and reduced pressure. Application would have been wider except for the following two reasons: relatively low output power (typically 1 mW), and the need to operate at cryogenic temperatures (usually $\leq$ 77 K). The former limits the use of diode lasers in techniques such as photoacoustic detection and saturation spectroscopy, where power in the radiation source is a necessity. The latter generally renders the diode lasers cumbersome and impractical for in situ type of analysis. The spin-flip Raman (SFR) laser, schematically illustrated in Figure 2, is a device that uses a fixed-frequency laser (CO_2, CO, or HF gas laser) to pump a semiconductor crystal in a magnetic field (62). The pump-laser photons are inelastically (Raman) scattered by the electrons in the crystal. Because of the presence of the magnetic field, there is a separation in energy levels between those electrons whose spins are aligned along the field and those with opposite spins. As a result, scattered photons may be shifted to a lower frequency (Stokes component) or a higher one (anti-Stokes component). Both of these, plus some weaker components, constitute the output frequency range of SFR lasers. Continuous tuning is done by varying the magnetic field. Typical field strengths range from a few Gauss (71), to hundreds of kG (72).

Some of the properties of the SFR lasers which make it attractive for air pollution study are its potential for wide-range tunability, high output power (> SDL) and good mode quality (62). Already they have been applied to balloon borne in situ measurement of NO at a

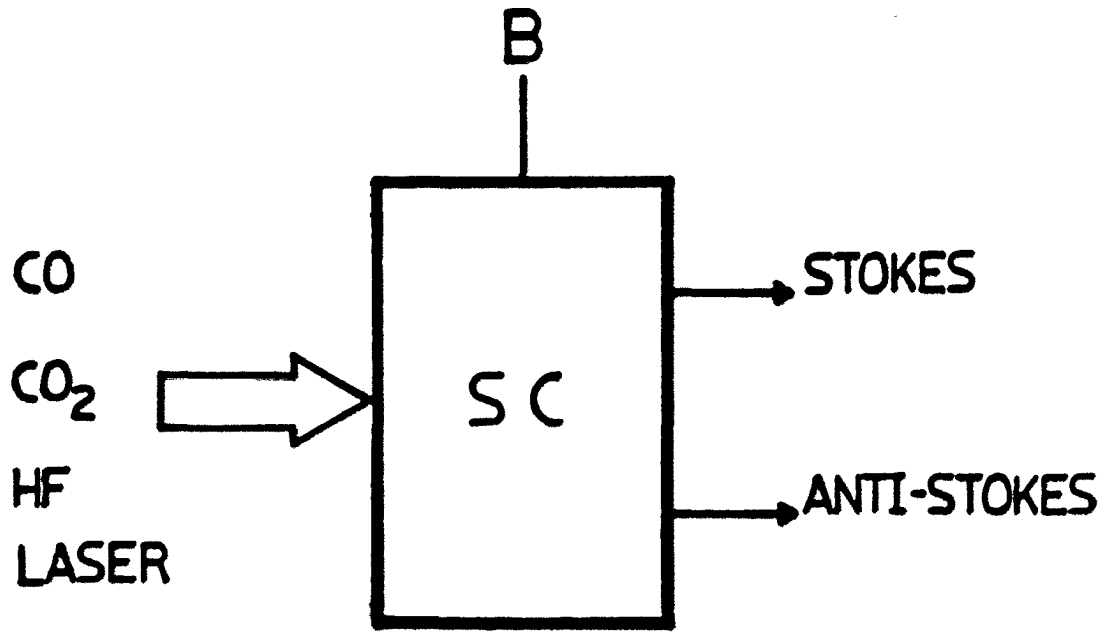

Figure 2. Schematic representation of a spin-flip Raman laser. B is the magnetic field

height of 28 km in the stratosphere by Patel et al. (73). Another use of SFR lasers include the monitoring of NO in automobile exhaust and in the atmosphere (74). The one disadvantage against SFR lasers is that their operation is too complex (cryogenic cooling required) for routine use.

Conventional fixed-frequency gas lasers such as CO_2, CO, and HF have most frequently been operated at pressures of around 10 torr. Consequently, the gain band widths are essentially Doppler-limited to approximately 50 MHz. Continuous tuning usually does not exceed a small fraction of a cm^{-1} (e.g. ~ 0.0002 cm^{-1} for a CO_2 laser transition). For this reason they are generally considered to be discreet-line sources and seldom match perfectly with the absorption lines of molecules to be detected which results in reduced sensitivity. Fortunately, this apparent shortcoming is somewhat compensated for by the relatively high power output of these lasers (~ 50 W cw). In techniques whose sensitivity depends strongly on the photon intensity of the radiation source, e.g. photoacoustic spectrometry (75), there is still extensive use of these lasers (76-79).

Even in cases where the difficulty in matching becomes acute, techniques based on Zeeman and Stark tuning of some molecular absorption lines into coincidence with fixed frequency lasers can still find application in the field of atmospheric monitoring (80,81). Freund et al. (82) have successfully demonstrated the quantitative detection

of NO_2 by a CO laser (6.2 um) based on Zeeman effect. Sweger and Travis (83) have also reported the detection of a series of trace organic gases tuned in coincidence with a CO_2 laser by the Stark effect.

A number of improvements in laser technology have led to the development of a high pressure gas (HPG) laser (84-87). Operating under pressures ranging from 1-15 atm., the range of continuous tuning of these lasers has increased (0.2 cm^{-1}) due to pressure broadening of the gain bandwidth. HPG lasers generally have higher peak and average power than any other current tunable infrared sources, and this feature lends itself well for use in differential absorption systems using natural reflectors (67).

Several important sources of tunable infrared radiation are based on the principle of frequency mixing in a material possessing a non-linear index of refraction. These devices operate at room temperature, and thus have at least one operational advantage over the SDL and SFR laser described earlier.

One example of these nonlinear optical sources is the optical parametric oscillator (OPO). It consists of a laser pump source in the visible or infrared and a nonlinear birefringent crystal (e.g. $LiNbO_3$). The output frequency is established by the unique conditions required to simultaneously satisfy energy and momentum conservation for the parametric process occurring within the pumped material (88). By rotating the nonlinear crystal, by varying the refractive index through temperature changes, or by applying pressure, or an electric field, a

tunable infrared output can be achieved. Although OPO's operate both cw and pulsed, the latter is by far the more popular choice as an infrared source for air pollutant monitoring. Remote detection of CO using differential absorption and topographical backscattering targets has been demonstrated (89) using an OPO operating at 2.3 um. Because of their high power (tens of watts to several hundred kilowatts peak, and tens of watts average), the pulsed OPO showed promise for remote space-resolved monitoring of atmospheric pollutants (90). However, this type of laser is hampered by the fact that they do not offer a very narrow linewidth. The best obtained was only of the order of 10^{-3} cm^{-1} (91), which is not enough for the high resolution study of line parameters of atmospheric pollutants.

Another class of lasers based on the interaction between radiation and a nonlinear crystal is the so-called optical mixers (OM). This type of optical device usually involves two tunable lasers in the same or different regions of the spectrum mixed in a nonlinear medium to produce tunable output at shorter or longer wavelengths with sum-frequency (92) and difference-frequency (93) generation. High power (1 watt to tens of kilowatts) are generally available from these lasers. However, they suffer the same disadvantage as the OPO - broad linewidth, typically ranging from 1-15 cm^{-1}. One noted exception is the system reported by Pine (94). By mixing in $LiNbO_3$ the output of a dye laser with that of an argon laser, cw output in the 2-4 um region with power

of about 1 uw with linewidth of 15 kHz and continuous turning of ~ 1 cm^{-1} is generated. This system has been useful for laser spectroscopic studies of the C-H stretch region of hydrocarbons.

There is yet another class of lasers that has found its way into application for atmospheric monitoring, namely, the dye laser. These lasers generally offer narrow linewidth ($10^{-3} cm^{-1}$) and moderately high power (100 mW - 100 W). However, their output wavelengths do not quite cover the atmospheric window region and as such have limited use in the study of air pollution. Still, detection of a limited number of pollutants (e.g. SO_2, NO_2, O_3) by differential absorption or fluorescence techniques has been reported (95-97).

6. Laser-based techniques

Most of the laser-based monitoring techniques for gaseous air pollutants under development today are based on the principles of Raman scattering, resonance fluorescence, and resonance absorption (54,55,98).

In Raman scattering, the wavelength of backscattered radiation is shifted by an amount which is characteristic of the vibrational frequencies of the pollutants. Figure 3 shows the frequency shifts of the rotational-vibrational Raman spectra of typical trace molecules present in the atmosphere, as well as the major atmospheric constituents, with respect to the transmitted laser frequency (99). The estimation of the absolute concentration of each species can then be performed by comparing the Raman backscattered intensity with that of the Raman line from N_2 molecules which occupy the same volume (59,100). Since Raman

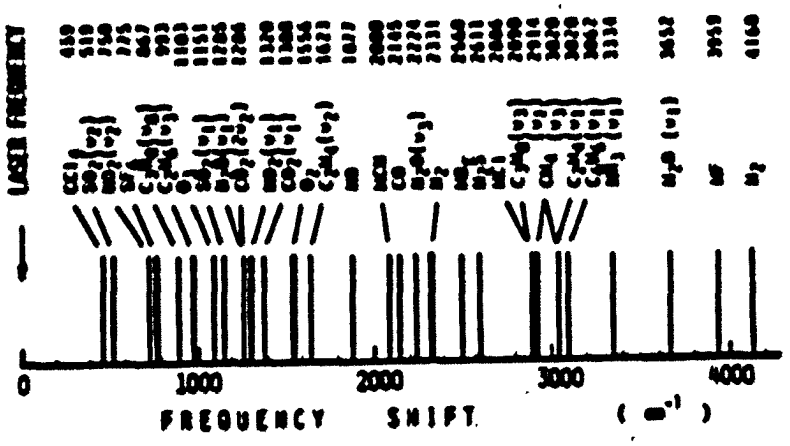

Figure 3. Frequency shifts of Q-branch of vibrational-rotational Raman spectra of typical molecules present in ordinary and polluted atmosphere relative to the exciting laser frequency (99)

features are generally sharp and can be readily recognized, it is therefore possible at monitor a variety of gases using one single, fixed-frequency laser. Besides being readily adaptable to point sampling, it also shows promise as a remote sensing method. Menzies and Shumate (101) have used a heterodyne detection scheme to detect scattered radiation from CO and CO_2 lasers. Unfortunately, conventional Raman techniques suffer one disadvantage - the minuteness of the effect. Even in the most favorable cases, only the order of 10^{-8} of the incident intensity is converted into signal. Translated into atmospheric monitoring terms, this means a relatively high power laser is required to achieve low detection limits of trace level pollutants. As a result, Raman methods will probably be limited to major atmospheric constituents in point or source monitoring.

The resonance fluorescence process has a higher quantum yield than Raman scattering. On this merit alone, it has attracted considerable attention in applications to atmospheric monitoring. Perhaps the best studied air pollutant based on resonance fluorescence is NO_2 (102-106). Most of the research done to date has been limited to point sampling of ambient NO_2 (107-109) based on visible light sources. This is due to the fact that fluorescence intensity suffers from quenching in the atmosphere because of the collisions with air molecules when used as a remote sensing technique.

Techniques based on fluorescence induced by infrared source excitation have also been studied. The most widely used IR source is the CO_2 laser. The fluorescence wavelength is generally shorter than

that of the excitation source (10.4 u to 5.3 u). Using the 10.6 u lasing line, feasibility studies of C_2H_4 (110) and H_2SO_4 aerosol (111) were conducted. Robinson et al. (112) also did a real-time monitoring of hydrocarbons in the atmosphere by a laser-induced IR fluorescence system that included a large gathering mirror, a modulated laser source to eliminate interference from thermal emission and phase-shift equipment to eliminate interferences from back-scattering.

Of the three optical monitoring techniques, resonance absorption is generally accepted as the most sensitive (55). This is because absorption cross-sections are the largest of all the optical interactions. Methods based on resonance absorption are the most widely used in atmospheric monitoring, especially in cases where pollutant gases exist in trace quantities. Detection of these gases usually means very sensitive measurements of small amounts (or increments) of transmitted or absorbed laser energy. There are generally three techniques commonly used for such measurements: direct transmitted photon detection, photoacoustic detection, and heterodyne detection.

a. Direct transmitted photon detection This technique of detecting infrared radiation (also known as incoherent detection) is the most commonly used of the three to be discussed. It basically involves direct conversion of incident photons to charge carriers by means of photoconduction, photodiode operation, or thermal conversion. Based on the temperatures under which they operate, these detectors can be classified into two types: room-temperature and cooled (77 K) detectors.

Examples of the first type include the PbS, Golay cell, InSb, pyroelectric, and the bolometer detectors. As a general-purpose infrared detector, the pyroelectric is the best choice in terms of spectral coverage and response speed, and its sensitivity is adequate for routine analysis (70). For the cooled infrared detectors, the most sensitive ones are usually the extrinsic or intrinsic photoconductive (PC) or photovoltaic (PV) detectors composed of various semiconductor materials, e.g. PbSnTe(PV), HgCdTe(PC), and InSb(PV). These detectors are generally more sensitive than a pyroelectric one, and the detection of weak atmospheric absorption lines or low-power laser radiation is correspondingly better. In addition, their response speed is typically three to four orders of magnitude faster than that of room-temperature detectors. Very often these detectors are used to sense the difference between incident and transmitted power. If this difference is minute, detection can become difficult.

Some efforts have been made to improve the signal-to-noise ratio (S/N), and hence the detection limit, for measurements based on direct transmitted photon detection. Derivative techniques were the most studied ones. This usually involves modulation of the radiation frequency so that the output wavelength of the light source is made to be on and off resonance with the absorption line of the molecule to be studied in a periodic fashion. The resulting signal is proportional to the derivative of the absorption line shape. It was found that for long path monitoring this technique considerably reduced the noise caused by atmospheric turbulance and by scattering from

aerosols. Ku et al. (70) have measured changes in transmission of 0.3% over a 0.6 km atmospheric path, using a derivative scheme with a pyroelectric detector. A detection limit of CO of 5 ppb has been reported. Reid et al. (113,114) were able to detect absorptions as small as 0.001% in a multipass cell with an effective pathlength of 100 meters at a reduced pressure of around 10 torr using a second-harmonic technique. This technique enabled them to measure absorption coefficients as low as 10^{-9} cm^{-1}. SO_2 concentration was measured in the low ppb range and other gases having stronger IR absorption than SO_2 (e.g. O_3, CO_2, NO, CO, CH_4 and NH_3) were measured down to less than 1 ppb.

b. Heterodyne detection Heterodyne techniques have been in general use in radio engineering for many decades. In a typical set-up, a weak signal is mixed with the strong signal of a local oscillator, and the resulting signal is detected by a sensor responsive to a narrow band of frequencies determined by the beat frequencies on each side of the local oscillator frequency. There are many advantages of the technique, not the least being that it is convenient to control the gain and selectivity of the sensitive bandwidth (115). The combination of heterodyne detection with atmospheric monitoring is a logical step when the following factors are considered. First, the infrared laser with its stable and narrow output frequency is an obvious choice for a local oscillator. Second, high-speed infrared detectors, such as the ones mentioned in the previous paragraph are readily available. Third, the intensity of radiation emanated from atmospheric constituents, whether it be backscattered radiation or thermal emission, is usually weak.

For it to be detected, a sensitive technique is necessary. Last but not least is the fact that high spectral resolution is generally available in heterodyne techniques (116). The spectral resolution is important in remote observation and measurement of atmospheric constituents, as it makes the technique selective, thus minimizing interference problems due to overlapping lines or bands.

There are numerous applications of heterodyne detection in the field of atmospheric monitoring. By the mixing of radiation from a characteristic emission line with that from a tunable laser, and a wideband infrared detector, passive remote sensing of several gases was possible (68,69,117). A balloon-borne laser heterodyne radiometer using a $^{14}C^{16}O_2$ laser as the local oscillator was built by Menzies et al. (118) for the stratospheric measurement of ClO. In systems which detect radiation scattered from such reflectors as atmospheric aerosols or natural terrain at long distances, the return signal is usually very small. Consequently, heterodyne detection has been used (101) to detect scattered radiation from CO and CO_2 lasers whose lines were selected to match pollutant gas absorption lines. In yet another system, a pair of CW CO_2 lasers were used in conjunction with long range scattering targets for the topographic study of atmospheric pollutants by heterodyne detection (53). One laser served as the local oscillator and was operated at a power level that placed the photodetector in a favorable regime. The second laser is used as the source of radiation transmitted into the atmosphere, a portion of

which was backscattered and was incident on the detector. A signal at the difference frequency was processed using narrow band radiofrequency detection electronics. Since the detected bandwidth was 3-4 orders of magnitude smaller than that possible with direct detection, this system had good discrimination against the background blackbody radiation prevalent in the atmosphere, so a very weak signal could be detected.

A related system which was developed by Davis (119) and Davis and Petuchowski (120), shows promise in trace detection of gases. The technique, christened phase fluctuation optical heterodyne (PFLOH) spectroscopy, employs a Mach-Zender interferometer as the detection chamber, with its two arms illuminated by the splitted beams of a single-frequency HeNe laser. One arm of the interferometer provides the local oscillator beam, the other contains the gaseous sample under study. A second laser with frequencies matching the absorption lines of the molecules of interest, is used as an excitation source for the sample. Subsequent de-excitation of the gaseous molecules by collisional quenching leads to local heating and expansion of the background gas. The resultant change in refractive index causes a shift in the phase of the HeNe beam in the sample arm, which is detected by heterodyne detection. Although limited mostly to point monitoring, the system has good detectability. By incorporating Stark modulation to discriminate against background signals caused by interfering absorbing species, a detection limit of 5 ppb NH_3 in air was reported (121).

c. Photoacoustic detection Detection based on photoacoustic spectroscopy (PAS) directly measures the absorption of laser power. The technique uses acoustic (over-pressure) signals to detect the heating of a gaseous sample by absorbed radiation. Although it has a long history, the use of photoacoustic spectroscopy for air pollutant detection was first proposed only in the early seventies by Kreuzer (122). With the availability of powerful infrared lasers, this technique has gained in popularity because of the low detectability generally possible (75).

A PAS detection instrument consisting of a radiation source of excitation, a modulator, and an acoustic detector (microphone) is often called a spectrophone. The detected photoacoustic signal is proportional to both the power of the incident radiation and the concentration of the absorbing species. There are numerous applications of photoacoustic detection to air pollutant monitoring, using either fixed-frequency or tunable lasers. Kreuzer and Patel (74) used the technique in conjunction with a tunable spin-flip Raman laser to detect NO in vehicle exhaust and ambient air samples at a detection limit of 10 ppb. Patel et al. (123) and Burkhardt et al. (124) constructed and launched a balloon-borne SFR laser-spectrophone detection system to monitor NO and H_2O in the stratosphere. The power of the SFR lasers used in these systems was in the order of 50 mW. Kreuzer et al. (79) studied the application of photoacoustic detection employing CO and CO_2 discreetly tunable lasers to detect a variety of

pollutant gases. Photoacoustic detection of NO_2 by both cw (123) and pulsed (125) dye layers have also been reported. Because of the low power of the diode lasers, there has been only one study done on the PAS technique with this type of laser (126). A detection limit of 50 ppm was achieved for carbon monoxide in nitrogen using a doublepass cell with a 96 uW diode laser source.

The ultimate detectable PAS signal is limited by noise in the transducer preamplifier and noise caused by Brownian motion of the molecules (122,127). In practice, this ultimate limit is not reached because of absorption in the cell windows and cell walls, which also generates an acoustic signal. This background signal limits the PAS technique when it detects very weak absorptions. Some attempts have been made to reduce it. They include a) the use of an acoustically resonant spectrophone (128-130); b) the use of a differential system consisting of two cells in series, with a common window (131); c) the modulation of either the laser wavelength or the absorption wavelength by Stark or Zeeman effect (132-134); d) the positioning of the spectrophone inside a laser cavity (135,136). Detailed discussion of these methods will be deferred until the next chapter.

Many atmospheric pollutants have been successfully studied by the PAS technique. By using an acoustically resonant detector, Gerlach and Amer (137) were able to measure CO concentration at the 150 ppb level. By combining acoustically resonant operation and a multipass arrangement, detection of SO_2 concentrations as low as 0.12 ppb was reported by Koch and Lahman (138), who used a frequency-doubled dye

laser of 1 mW ultraviolet output power. Other examples include the trace detection of C_2H_4 by laser intracavity operation (136), the detection of explosive vapors in the atmosphere (139), the monitoring of absorption and scattering of visible light by aerosols in the atmosphere (140), and the study of methane at normal atmospheric concentration by a pulsed DF laser (141).

In addition to point sampling (both ambient and reduced pressure) or in situ monitoring, the PAS technique can also be adapted for remote sensing. Perlmutter et al. (142) devised a PAS radiometer for remote trace gas analysis. The results indicated that while the photoacoustic effect in gases can be used for radiometric analysis, there are practical limitations due to the sky background and interference by ambient remote pollutants.

C. Conclusion

In this chapter, a review of current methodology for air pollutant monitoring, both nonlaser-based and laser-based, was presented. It is evident from the volumes of literature on the latter that laser-based detection techniques are gaining in popularity because of certain advantages they offer. In the subsequent chapters, two laser-based detection schemes: one based on photoacoustic effect, the other on Fabry-Perot interferometry, will be presented in conjunction with a novel method of modulating the laser source.

II. PHOTOACOUSTIC DETECTION OF GASEOUS AIR POLLUTANTS

A. Historical Background

The photoacoustic effect was first discovered by Alexander Graham Bell (143) in the late nineteenth century. He reported the generation of an audible sound upon focusing intensity modulated light on a solid substance in a sample cell. Tyndall (144) followed up on the reported observation and observed similar results with gas samples. Bell later noticed the same effect in liquids. He also investigated the effect at different light wavelengths. Rontgen (145) performed early work in this field too. The effect, while a novelty then, was deemed to lack practical value and was soon forgotten. It lay completely dormant for nearly 50 years until the advent of microphones. Viengerov (146), using a periodically intensity modulated thermal radiation source, and an acoustically resonant sample space in which a pressure transducer was mounted, then constructed the first gas concentration measurement instrument based upon this effect. He later recorded the first absorption spectra using the radiation from a carbon arc filtered by a prism monochromator to excite the gas in his photoacoustic detector (147). Other applications around that time focused primarily on studies of vibrational lifetimes and other aspects of radiationless deexcitation in gases, such as the determination of energy transfer rates between vibrational and translational degrees of freedom of gas molecules (148), deactivation rate measurements (149), and collisional relaxation rates (150).

Since its revival in the late 1940s, the photoacoustic effect has been used mainly in nondespersive-type IR gas analyzers (151). However, between 1950 and 1970, this type of gas analyzer, which employed a conventional IR source gradually gave way to the more sensitive gas chromatography. And the photoacoustic spectrometer was overtaken by the more versatile infrared spectrometer.

With the advent of coherent monochromatic optical radiation sources such as lasers, interest in the photoacoustic effect has been renewed and the application area widened. The three laser attributes of particular advantage to the photoacoustic effect are monochromaticity, high power, and collimation. The fact that lasers are highly monochromatic means that the potential exists for matching strong gas absorption lines with suitable laser sources to achieve specificity. The high power available from laser sources makes possible increases in the sensitivity of detection. The high degree of collimation of lasers allows the exciting energy to be focused on a small volume.

The earliest experiments with a laser illuminated photoacoustic detector were conducted by Kerr and Atwood (75). They measured a weak absorption spectrum of a water vapor line with a peak absorptivity of $3 \times 10^{-5} m^{-1}$ and absorptivities down to $1.2 \times 10^{-7} m^{-1}$ of $CO_2 - N_2$ mixtures. Kreuzer (122) performed the first gas concentration measurement using a photoacoustic detector and a laser. Later experiments by Kreuzer and collaborators have effectively demonstrated the extremely high sensitivity attainable with this method.

B. Theory

A simple physical description of the photoacoustic effect can be given by considering the following experiment. A cylindrical tube is filled with a gas mixture to be analyzed. Optical radiation containing wavelengths absorbed by the gas is directed along the axis of the tube. Infrared absorption produces excited vibrational-rotational states in the absorbing molecule, and ultraviolet radiation produces excited electronic levels. Subsequent deexcitation can take two routes (Figure 4). One is through the collisional process between the excited molecules and the molecules of the background gas (nonradiative process). The other is by means of the radiative process whereby a photon with wavelength corresponding to that of the transition from the upper to the lower state will be emitted. It is interesting to note, that in the infrared region, at atmospheric pressure, typical values of the collisional life-time, τ_C and the radiative lifetime, τ_R are approximately 10^{-6} sec and 10^{-3} sec, respectively (122). Most absorbed energy is therefore preferably transferred to air through the collision process.

The result of collisions between the excited molecules and the background gas is an increase in the translational energy (and hence the pressure) of the sample. The incoming radiation is modulated so that an acoustic signal is generated. A sensitive microphone connected to the wall of the chamber can be used to detect the periodic variation of the pressure (at the modulation frequency of the incoming radiation) which is then converted into an electrical signal. The electrical

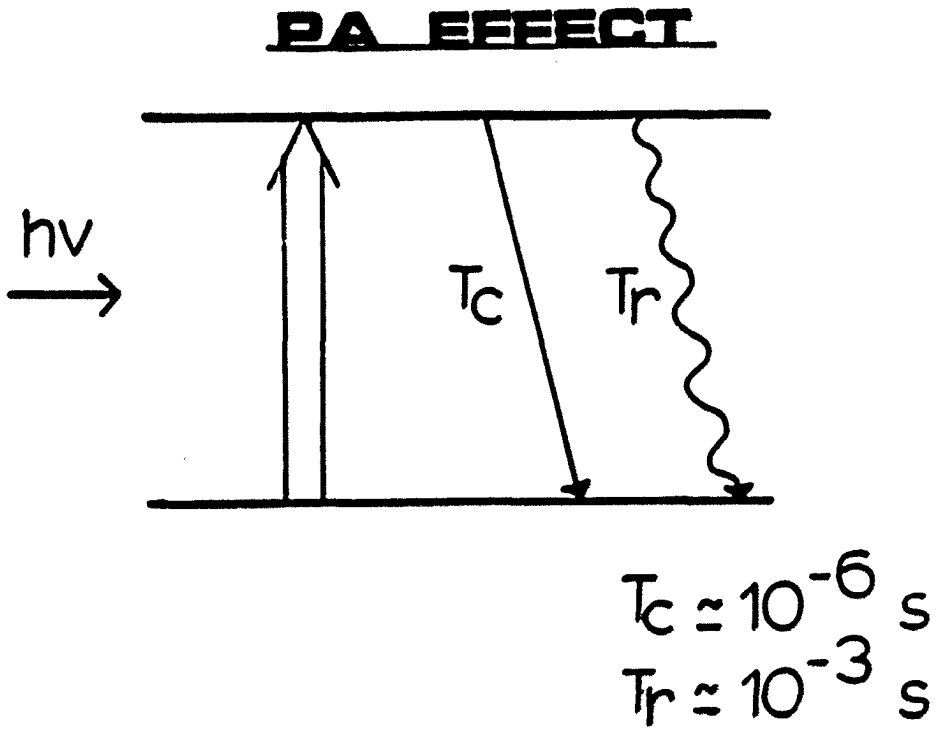

Figure 4. Schematic representation of the photoacoustic effect. τ_c- collisional lifetime; τ_r- radiative lifetime

signal is usually fed into the input of an amplifier. A typical instrumental set up is presented in Figure 5. Such a set up is often called a spectrophone.

Roessler and Faxvog (152) have derived a very simple theory for the photoacoustic signal, which assumes a uniform pressure rise and neglects thermal and viscous losses at the cell walls. The photoacoustic signal, p, derived by this theory is expressed as

$$p = \frac{RU}{L}[1-\exp(-\alpha CL)] \qquad (2.1)$$

where U is the incident optical power, L is the cell length, C is the sample concentration, α is the absorption coefficient, and R is the cell responsitity and is given by

$$R = \frac{(\bar{\gamma}-1)SL2/\overline{2}}{\pi\omega V} \qquad (2.2)$$

where S is the microphone sensitivity (mV/Pa), $\omega/2\pi$ is the modulation frequency, V is the cell volume, and $\bar{\gamma}$ is the ratio of the specific heats of the sample.

Combining equations (2.1) and (2.2), and assuming an optically thin cell, i.e. very small concentrations, we have

$$p = \frac{2/\overline{2}(\bar{\gamma}-1)USaCL}{\pi\omega V} \qquad (2.3)$$

Equation (2.3), although derived from a simplified model of photoacoustic signal generation does offer certain insights into the analytical basis of the photoacoustic effect. First, there is the

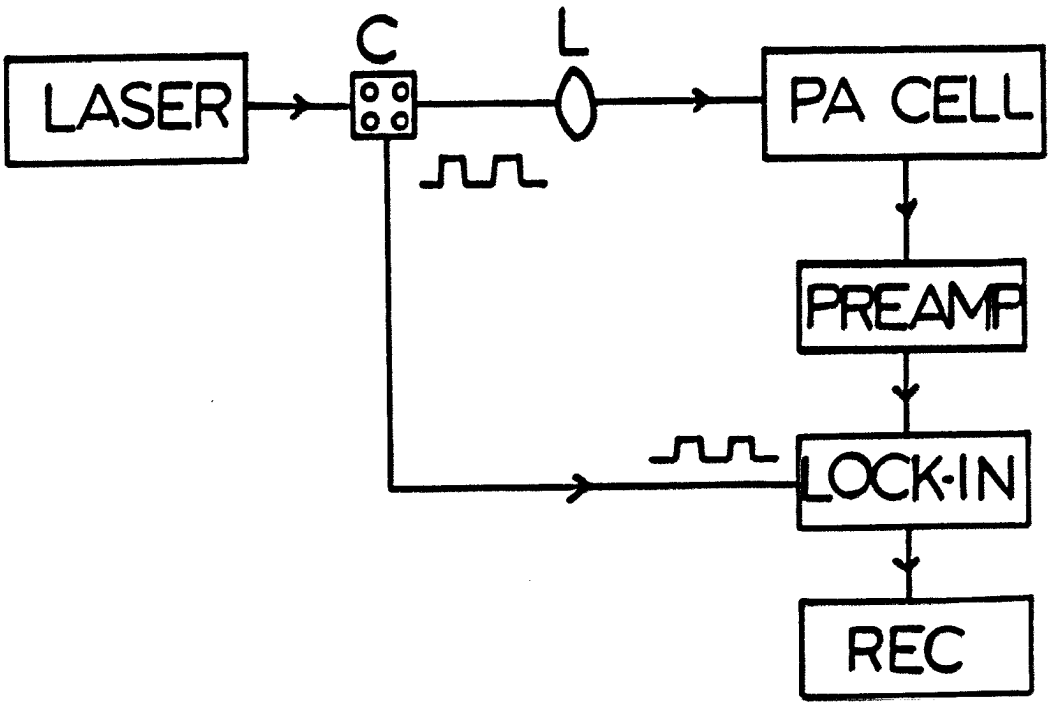

Figure 5. Typical instrumental set-up of a spectrophone. C- chopper; L- focusing lens

direct proportionality between the signal, p and the concentration of gas sample, C. Then, there is the linear relationship between p and the optical power U. The combined effects of these two factors are potentially greater sensitivity and dynamic range, as compared to conventional absorption, correlation (153), and derivative (68,154) spectroscopy. By simply employing a more powerful laser, the detectable concentration of a certain species can be lowered, thus extending the linear dynamic range. According to Dewey (155), the range is at least three orders of magnitude and limited primarily by the linearity of response of the microphone being used.

There are other factors and processes that govern the pressure rise in a photoacoustic cell which are omitted by the derivation of Roessler and Faxvog. They include molecular relaxations, energy transfer, thermodynamic properties of the gas, acoustic quality of the cell, and losses of energy due to thermal conductivity. Rosengren (127) has derived an expression that includes all of these factors. Assuming an optically thin cell, i.e. $NaL \ll 1$, where N is the density of molecules of interest, α the absorption cross section per molecule and L the cell length, the rms value of the first harmonic of the pressure signal generated by an approximately square-wave modulated light beam (Figure 6) is given by

$$p(\omega) = \frac{2^{3/2}\beta U N a L Q(\omega) T_t}{3\pi V(1+T_c T_r^{-1})[1+(\omega T_t)^2]^{\frac{1}{2}}\{1+[\omega(T_c^{-1}+T_r^{-1})^{-1}]^2\}^{\frac{1}{2}}} \qquad (2.4)$$

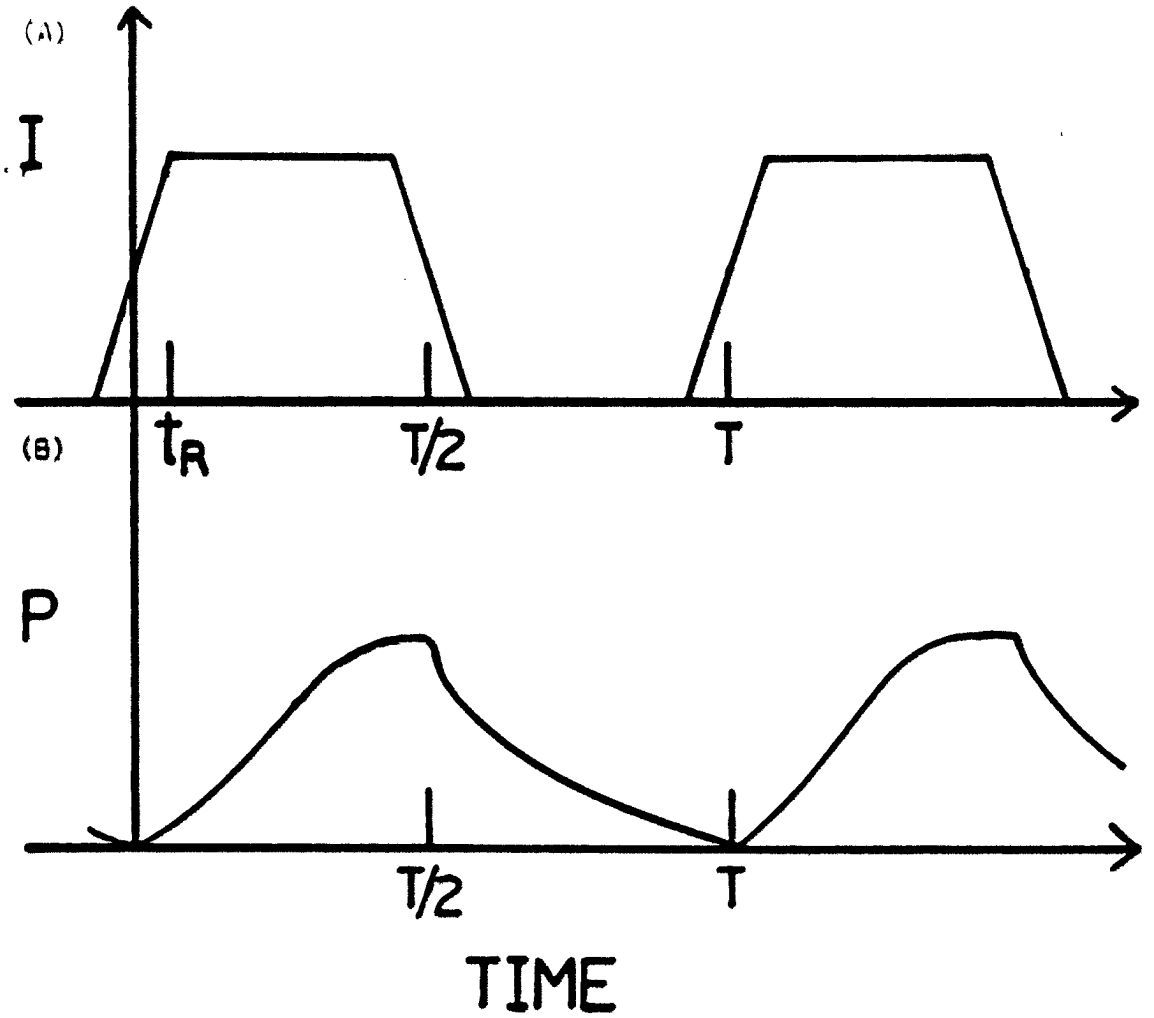

Figure 6. Generation of pressure signal. (A) Time fluctuating mean radiation power in the cell. (B) Time fluctuating pressure in the cell produced by absorption of the radiation shown in (A). I-power; P = pressure signal; t_r-rise time; T-period time (127)

where $\omega = 2\pi f$, the modulation frequency,

$\beta = (3/2)(C_p/C_v - 1)$, the fraction of laser energy absorbed by the gas and converted into translational energy (C_p and C_v are the specific heats at constant pressure and volume, respectively),

U = laser power within the cell

$Q(\omega)$ = acoustical quality factor of the cell,

V = cell volume,

τ_c = collisional relaxation time,

τ_r = radiative relaxation time,

τ_t = thermal relaxation time of the cell, a factor used to describe the dissipation of acoustic energy through losses by thermal conduction, diffusivity, and viscosity.

Equation (2.4) is simplified by making the following assumptions. Two relaxation processes from the excited state are considered, namely, collisional relaxation with relaxation time τ_c, and radiative relaxation with relaxation time τ_r, and $\tau_c \ll \tau_r$ (see above). The value of $Q(\omega)$, the acoustic quality factor, for a cell with fixed volume and with no acoustical resonance at the modulation frequency is equal to 1. Equation (2.4) becomes

$$p(\omega) = \frac{2^{3/2}\beta U N_0 L \tau_t}{3\pi V[1+(\omega\tau_t)^2]^{\frac{1}{2}}} \qquad (2.5)$$

From equation (2.5), several general observations can be made regarding the photoacoustic signal in an acoustically nonresonant cell (an acoustically nonresonant cell is understood to be one with a sample space so designed that no natural acoustical resonances influence the operation of the device in a noticeable manner):

(1) The signal dependence on optical power is still intact, as long as saturation of the absorption lines does not occur.

(2) The photoacoustic signal is proportional to the concentration of the absorbing species. The linearity holds up to a concentration level of about 1%.

(3) The photoacoustic signal is proportional to $1/a^2$, where a is the cell diameter. It is therefore advantageous to reduce the cell diameter. There is, of course, a practical limit to this reduction. Care must be taken not to heat the cell walls, which creates an extraneous background signal. Optical diffraction theoretically sets the lower limit for the cell diameter.

(4) The photoacoustic signal appears to be independent of the cell length. Simple application of the Beer - Lambert law would dictate that the longer the pathlength of a homogeneously distributed region is traversed by the incoming radiation, the more optical energy will be absorbed by the gas sample, and more will be converted into molecular-translational energy through subsequent collisional deactivation. While this reasoning is correct in essence, it neglects a subtle point - longer pathlength (cell length) means a larger volume of gas sample to be heated up for

the eventual pressure fluctuations. In addition, the transducers (microphones) used in most nonresonant photoacoustic cells are located in one particular spot along the cell length, and with their limited sensing areas, can only efficiently detect pressure fluctuations in their immediate vicinity. There is, however, one advantage in increasing the cell length. The relative phases of the acoustic signal of the gas and that of the background can be changed by increasing the cell length to the extent that discrimination against the background signal is enhanced (156). More detailed discussion on photoacoustic signal vs. cell design can be found in (127).

(5) The photoacoustic signal bears an inversely proportional relationship with the modulation frequency. It is therefore advantageous to operate the system at a low frequency, as close as possible to $1/T_t$, T_t being the thermal relaxation time of the cell.

The last point is not immediately obvious from equation (2.5). However, using Kreuzer's definition of noise-equivalent-power of a photoacoustic detector $(NEP)_{PA}$ (157) which states that $(NEP)_{PA}$ is the amount of power that would have to be absorbed by the gas to produce a signal amplitude equal to the noise amplitude, an expression can be derived to evaluate the sensitivity of a photoacoustic detector:

$$(NEP)_{PA} = (3\pi/2^{3/2})(V/\beta T_t)(N_B^2+N_e^2)^{\frac{1}{2}}[1+(\omega T_t)^2]^{\frac{1}{2}} \qquad (2.6)$$

where N_e = noise in the microphone preamplifier circuit, and

N_B = noise caused by the Brownian motion of the molecules.

Ideally $(NEP)_{PA}$ should be kept as small as possible for best sensitivity. According to equation (2.6), photoacoustic sensitivity appears to be highest at a low modulation frequency. However, amplifier and electronic circuits are usually noisiest at low frequencies, so a trade-off has to be made in order to achieve optimum sensitivity - i.e. the amplifier noise contribution to the overall photoacoustic signal cannot usually be neglected. More will be discussed on the noise considerations affecting the photoacoustic effect in a later section.

There is another operating parameter that exerts a great deal of influence on the strength of photoacoustic signal as sensed by a microphone - pressure within the photoacoustic cell. Wake and Amer (158) have derived an equation to describe the pressure dependence of the nonresonant PAS signal of a mixture of absorbing and nonabsorbing gases, based on the equation derived by Kerr and Atwood (75) for the total pressure rise in PAS detection. Several assumptions were made in this derivation. First, the cell was assumed long and thin, so that heat loss through the end windows was small compared with heat loss to the walls. Secondly, the laser beam was assumed to have a Gaussian intensity profile and cylindrical symmetry. Thirdly, an assumption of $\beta(P_o)<<1$ was made, where $\beta(P_o)$ was the gas absorptivity at pressure P_o. When the exciting light is approximately square-wave modulated, the first harmonic lock-in amplifier output is expressed as

$$V = S(P_o,\bar{\gamma},T)\beta(P_o)\frac{W}{L}\frac{P_o}{4\pi\bar{K}T}\sum_m \frac{D_m \exp(i\theta_m)}{[1+(\omega^2 a^4/\alpha^{-2}\xi_m^4)]^{\frac{1}{2}}} \qquad (2.7)$$

where $\beta(P_o)\frac{W}{L}$ is the power absorbed per unit length, P_o and T are the equilibrium pressure and temperature within the cell, respectively, a is the radius of the cell, $\bar{k}$ is the effective thermal conductivity and $\bar{\alpha}$ is the effective thermal diffusivity of the gas mixture, ξ_m is the mth root of the zeroth order Bessel function $J_o(\xi) = o, D_m(b)$ are numerically calculated coefficients which depend on b, the ratio of the Gaussian beam waist to the cell radius, $\Theta_m = \arctan[(\omega a^2/\bar{\alpha}\xi_m^2)^{-1}]$, and $S(P_o, \bar{\gamma}, T)$ is the sensitivity of the microphone.

Figure 7 is the graphic representation of the behavior of the PAS signal for CH_4 at a partial pressure of 10 torr in various buffer gases as a function of the total pressure inside the cell. It also includes the theoretical curves predicted by equation (2.7). All these curves (experimental and theoretical) exhibit a similar pattern for the PAS signal: first increasing until a maximum is reached, and then decreasing as the total pressure (P_o) goes up (beyond ~200 torr). The dependence of the PAS signal on pressure is therefore not a straightforward one. Fortunately, this can be explained by equation (2.7) which can be simplified by considering only the first member of the series.

$$V = S(P_o,\bar{\gamma},T)\beta(P_o)\frac{W}{L}\frac{P_o}{4\pi\bar{k}T}\frac{D_1 e^{i\Theta_1}}{[1+(\omega^2 a^4/\bar{\alpha}^2\xi_1^4)]^{\frac{1}{2}}} \qquad (2.8)$$

The initial rise is due to increasing P_o. This continues until the PAS signal reaches a maximum. At this point, the term $\omega^2 a^4/\bar{\alpha}^2\xi_1^4$ becomes much greater than 1, allowing the $1/P_o$ dependence of the

Figure 7. Photoacoustic signal as a function of the pressure inside the cell for 10 torr of CH_4 in various nonabsorbing gases. Solid lines are the theoretical predictions of equation (2.7). Modulation frequency is 50 Hz (158)

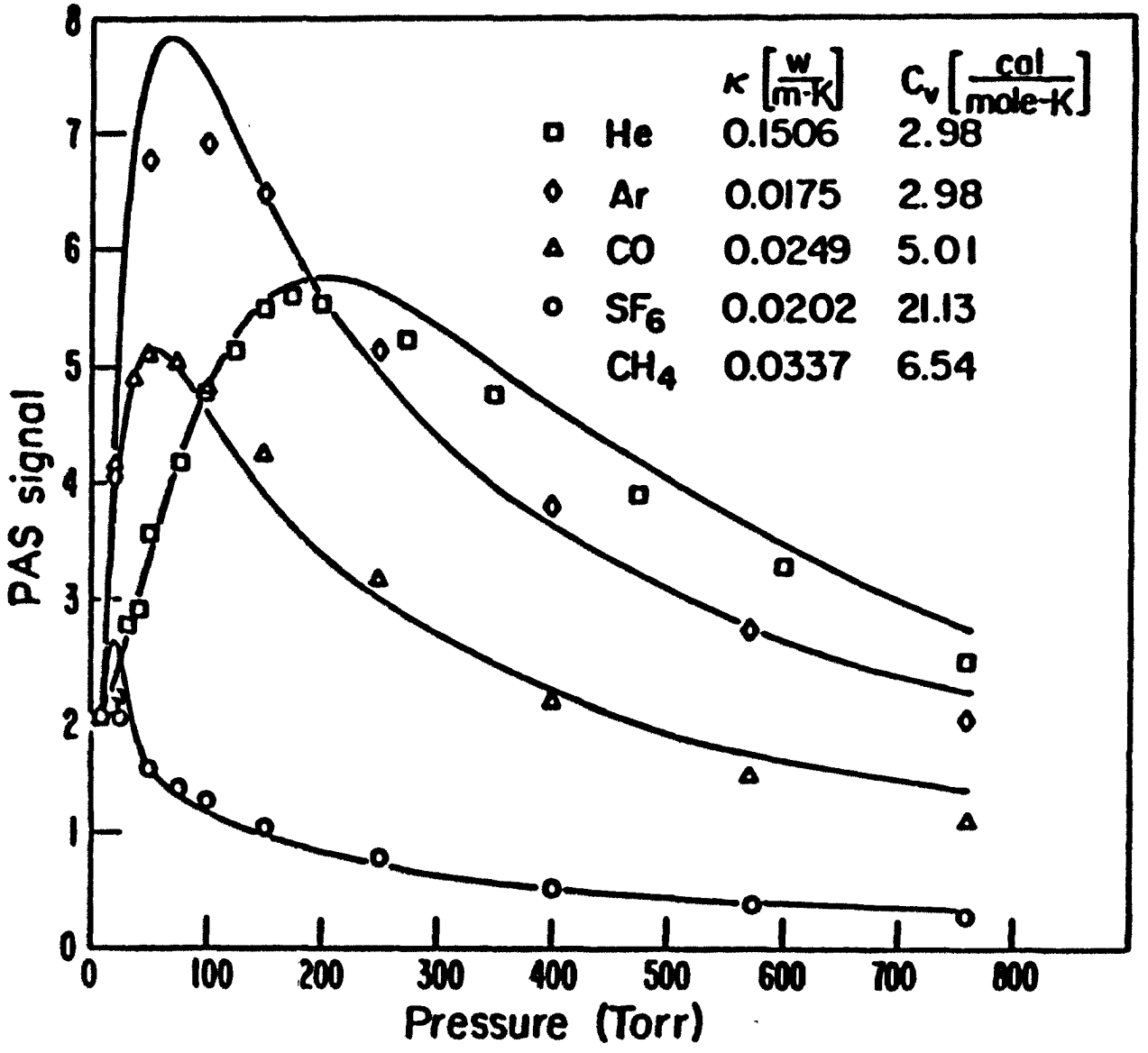
PAS signal
Pressure (Torr)
0
1
2
3
4
5
6
7
8
0
100
200
300
400
500
600
700
800
κ [w/m-K]
Cv [cal/mole-K]
He 0.1506 2.98
Ar 0.0175 2.98
CO 0.0249 5.01
SF6 0.0202 21.13
CH4 0.0337 6.54

effective thermal conductivity of the gas mixture to cancel the leading P_o factor and limit any further increase in signal. The fall-off in signal at high P_o can be explained by two factors. First, the 3.39 um output of the HeNe laser used in this experiment lies in near coincidence with the ν_3 absorption band of CH_4 (159), the absorbing species. Consequently, the power absorbed first rises, then falls with increasing pressure, P_o, as the CH_4 line is broadened into the laser line (Figure 8). Since the PAS signal is directly proportional to the power absorbed, it then follows that the signal falls off as the power absorption, $\beta(P_o)$, decreases. The second factor is the microphone sensitivity, $S(P_o,\bar{\gamma},T)$, which is also a function of P_o (160).

$$S(P_o,\bar{\gamma},T) = S_{rated}\frac{1+\beta}{1+\beta(P_o\bar{\gamma}T_{STP}/P_{atm}\gamma_{air}T)} \qquad (2.9)$$

where $\beta \cong 1$, $\bar{\gamma} = (\bar{C}_v+R)/\bar{C}_v$, and R is the gas constant. $\bar{C}_v$ is the effective specific heat at constant volume of the gas mixture and can be calculated by:

$$\bar{C}_v = \chi_i C_{pi}+(1-\chi_i)C_{pj}-R \qquad (2.10)$$

where C_p = specific heat at constant pressure,

i = mole fraction of i, and

j denotes the buffer gas.

Equation (2.9) indicates that the microphone sensitivity decreases as the total pressure, P_o, increases.

The combined effect of pressure and modulation frequency is depicted in Figure 8. It agrees, in general, with the previous discussion of the PAS signal dependence on modulation frequency, $\omega/2\pi$. It also indicates that an optimum pressure exists for each modulation frequency. Analytical detection based on the photoacoustic effect should therefore be performed at that pressure to achieve better results.

C. Noise Considerations

As with any detection system, noise is an inherent part of the photoacoustic signal. There are various sources of noise. The process of photoacoustic signal generation can be thought of as sequential stages of events. At each stage of the process, there will be mechanisms which add noise and degrade the ability to detect a small signal. In this section, the various noise sources will be discussed.

The ultimate noise limit for a pressure transducer stems from the Brownian motion of the sample gas molecules which gives the microphone diaphragm a random motion. The rms equivalent Brownian noise pressure in a frequency interval $\Delta\omega/2\pi = \Delta f$ around the modulation frequency $\omega/2\pi = f$ for a microphone with diaphragm area M and diaphragm damping force D, becomes (161)

$$N_B = \left(\frac{4kTD\Delta f}{M^2}\right)^{\frac{1}{2}} \qquad (2.11)$$

assuming that $\omega \ll \omega_M$ = microphone resonance frequency and where k = Boltzmann's constant and T = the gas temperature. Introducing the

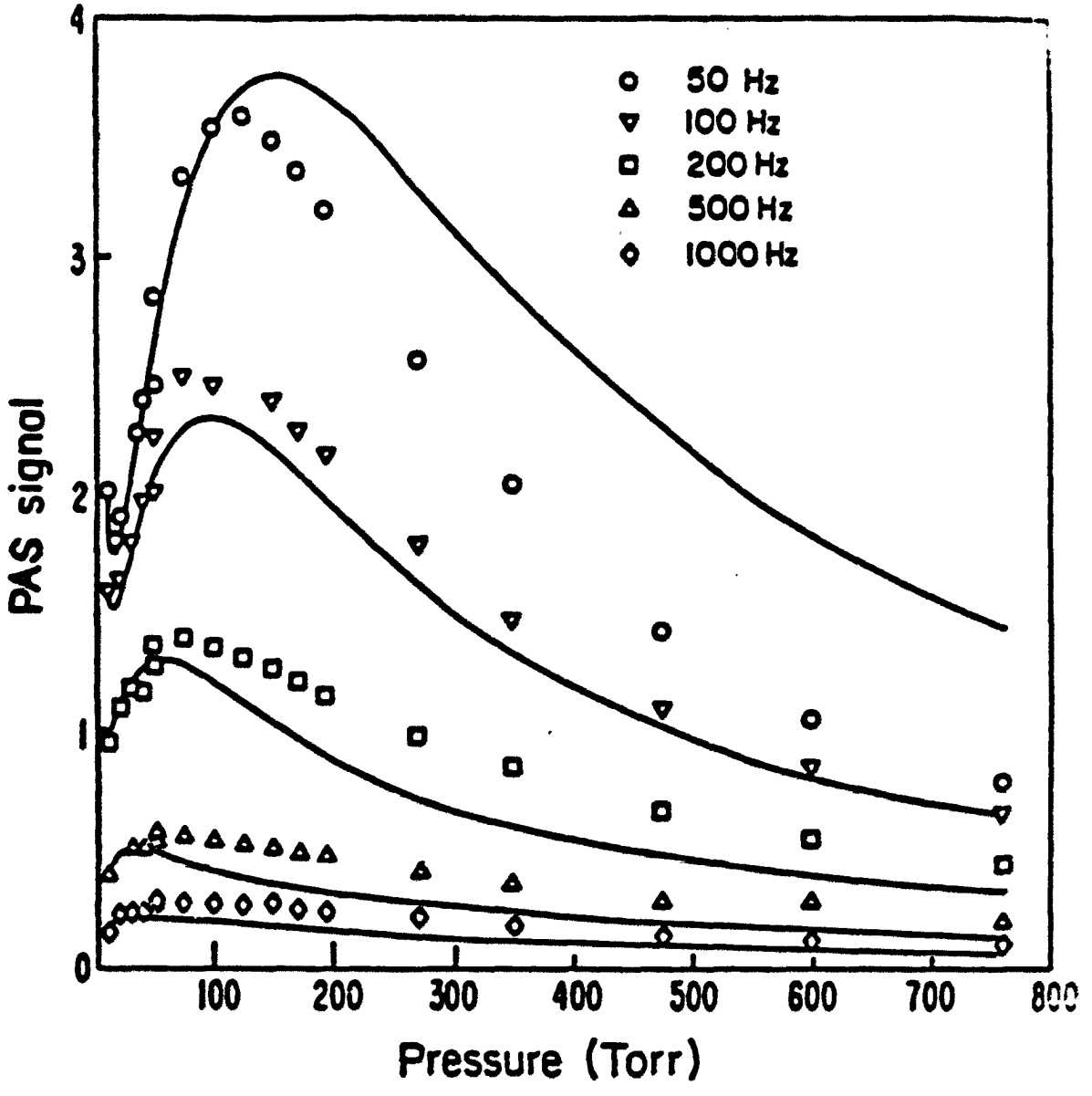

Figure 8. Photoacoustic signal as a function of modulation frequency for 10 torr CH_4 in H_2. Solid lines are the theoretical predictions of equation (2.7) (158).

damping time of the diaphragm, $T_M = 2\ m\ M/D$, where m = mass per unit area of the diaphragm, makes it possible to write equation (2.11) as

$$N_B^2 = \frac{8kTm\Delta f}{MT_m} \tag{2.12}$$

Equation (2.12) is the expression normally used in evaluating the Brownian noise. Judging from this expression, it can be concluded that a large diaphragm area decreases the Brownian noise. However, because of the fact that the microphone resonant frequency $\omega_M \alpha M^{-\frac{1}{2}}$, the area is limited from above by the maximal modulation frequency considered.

In addition to the Brownian noise, the electronic amplifier transferring the capacitance variation (as sensed by the microphone) to a voltage variation introduces noise. The rms value of this noise in an interval Δf around the frequency f expressed in an equivalent noise pressure is here denoted N_e, and is given by (161)

$$N_e = e(\Delta f)^{\frac{1}{2}}/R_t f \tag{2.13}$$

where R_t = resistance of the amplifier circuit and e is a constant calculated from the capacitance, and other characteristic of the microphone. From equation (2.13), it is clear that this noise is inversely proportional to the modulation frequency $\omega/2\pi = f$. In fact, this is true for almost all the electronic noise associated with the various stages of PAS signal processing, (amplification, etc.). Because of this, PAS operation at low frequencies is precluded.

The Brownian noise and the amplifier noise discussed so far determine the ultimate detector sensitivity. In practice, other noise contributions can dominate. Acoustical noise from the detector surroundings may be coupled into the detector sample space. When sample gas is flown continuously through a detector and if the gas flow is turbulent, if acoustical noise from the surroundings are coupled directly into the detector sample space or into the tubes connected to the detector and then propagated into the detector, or if acoustical disturbances from the pump running the sample gas through the detector are propagated through the tubes, acoustical noise can be produced. Proper insulation, thick detector and tube walls, small flow rates, etc., must be used to suppress these noise contributions. Finally, fluctuations in the radiation source output may produce a noise signal in the detector output. There is no general characterization of the behavior of these noise contributions to the signal. Each set of experimental conditions warrants a unique approach to solve the problem.

D. Background Signal Consideration

The most persistent difficulty encountered in achieving high sensitivity in PAS measurements has been the background signal that arises from absorption of the excitation beam by the sample cell windows and the radiation scattered to the cell walls. This background signal is proportional to excitation intensity, so with high-power laser

sources this effect can easily dominate the ultimate sensitivity limit imposed by Brownian noise and electronic noise discussed in the previous section.

The underlying physical processes involved in the production of the background signal have been investigated by Parker (162). From his calculation it is clear that the dominant source of acoustic disturbance is a thin film of absorbing material near the surface, rather than the bulk absorption. In the case of highly transparent windows with light incident from the solid side, the absorption region is sufficiently thin to allow the assumption that the heating takes place in a very small region at the gas-solid interface. This situation is depicted in Figure 9. The heat produced in this layer diffuses into the gas. This gives rise to a pressure increase in the cell. The rms value of the pressure amplitude for a chopped radiation beam with a uniform intensity distribution in a plane perpendicular to the propagation direction, which passes two windows becomes

$$P_b(\omega) = \frac{2^{5/3}\beta\alpha_s I}{3\pi\omega L}\left[\frac{kC_p}{k_w C_w}\right]^{\frac{1}{2}} \qquad (2.14)$$

assuming $\omega<<2v/L$, v = sound velocity in the gas; $k_w C_w/C_s^2$, $\alpha_s^2<<1$, where α_s = ratio of the absorbed radiation intensity by the surface layer to the incident intensity, C_s = heat capacity of the absorbing surface layer, k_w = thermal conductivity of the window, C_w = heat

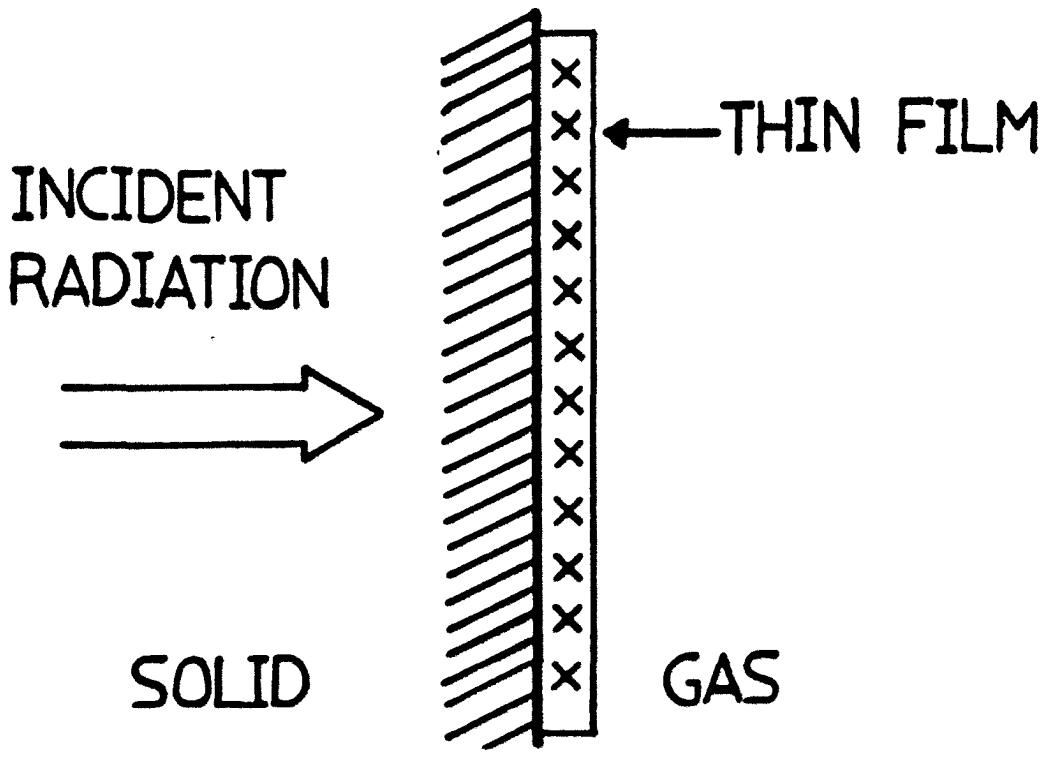

Figure 9. Absorption model for window heating background

capacity of the window, k = thermal conductivity of gas, C_p = heat capacity of gas at constant pressure. B, W, and L have the same denotations as in equation (2.4).

The window produced background can, in principle, be subtracted from the total pressure transducer output when its magnitude for a certain radiation power and sample gas has been measured. In fact, this has been done electronically with satisfactory results (122). However, due to the limited dynamic range of electronic amplifiers, the background signal should be minimized whenever possible. In addition, significant noise can be introduced in the subtraction process.

It is evident from equation (2.14) that the amplitude of the background signal can always be reduced by the judicious choice of window materials. The window material with the lowest $\alpha_s/(k_w C_w)^{\frac{1}{2}}$ ratio should be chosen if several materials with similar low refractive index and high transmittance are available. However, in the infrared region, the choice of window materials is somewhat limited. Most of the IR-transparent windows are made of halide salts of various alkaline or alkaline earth metals. Very often these materials are hygroscopic, i.e. they absorb water from the atmosphere. Since water has a continuum absorption in the 8-12 um region (163), this presents a problem.

The background signal produced by window absorption can also be reduced by increasing the cell length, L. In fact, the relative phases of the acoustic signal of the gas and that of the background was changed by increasing the cell length to the extent that discrimination

against the background signal was enhanced by a phase-sensitive amplifier (156). The extent of improvement is limited, especially since the volume must be increased substantially, which reduces the effective responsivity of the detector.

E. Background Signal Reduction

It is imperative from the previous discussion that many problems must be dealth with to minimize background contributions to the PAS signal. These background contributions present the major limitations upon the ability of the PAS technique to detect very weak absorptions. Several attempts have been made to solve this problem. Their approaches can generally be classified into two groups: 1) solution through cell design, and 2) solution through means of modulation other than the conventional chopper.

1. Cell design approach

Rosengren (127) has proposed two photoacoustic detector designs to combat the problem of window absorption. These designs are presented in Figure 10. In one of them he suggested the use of a two-cell detector as shown in Figure 10(A). It consists of a sample cell joined to the same sensor with an identical reference cell. The reference cell contains a gas that has similar thermodynamic properties as the gas mixture to be analyzed, but without the constituents that will be measured. The success of this design is predicated on the fact that the two background signals are identical both in magnitude and in phase, a nontrivial assumption.

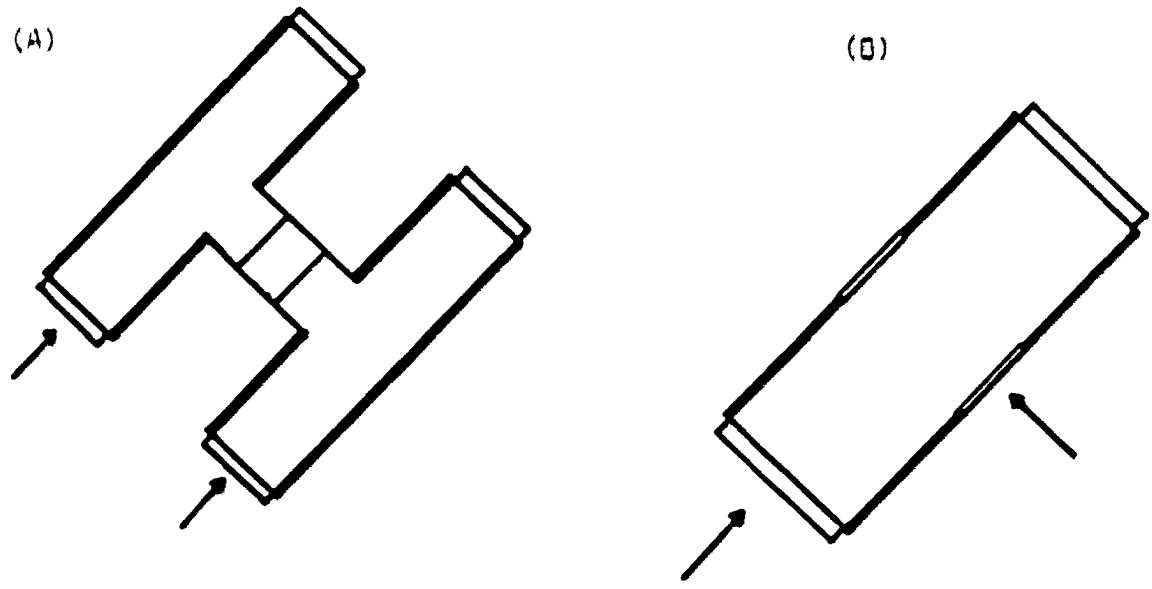

Figure 10. PAS cell design for background reduction (127). (A) Two-cell detector; (B) Two-path detector

The second design proposed by Rosengren is a two-path detector depicted in Figure 10(B). The cell has two propagation paths of different lengths L and L_r, where $L > L_r$. The radiation beam from the source is alternately propagated through these paths. The windows have $\alpha_s/(k_w C_w)^{\frac{1}{2}}$ ratios as equal as possible and are assumed to produce pressure rises of the same magnitude. Because a beam of radiation is always propagating through two detector windows, a constant background pressure signal is obtained. A varying pressure signal is, however, produced due to the periodic propagation pathlength change. The amplitude of the latter signal is given by equation (2.5) multiplied by the factor $(1-L_r/L)$. If, for some reason the background signals produced by the two pair of windows for equal radiation power differ, radiation attenuators can be used to balance out the background signal. One of the important advantages of this design is that if the radiation power varies, the adjustment of the power in the two radiation beams need not be changed. Another advantage with this reduction method is that no special reference gas mixture has to be prepared. However, the assumption that the pressure signals produced by the two sets of windows are identical may prove to be difficult to achieve in practice.

An approach somewhat similar to the two-cell design was the differential cell used by Deaton et al. (131). It consists of two chambers placed end to end with a bore in between and a window on the bore. The balanced window heating in the two cells reduces the background signal. Absorption measurements are made by filling one chamber

with a test gas mixture made up of the absorbing species and a non-absorbing gas, and the second chamber is filled with the same non-absorbing gas only, both to the same total pressure. The pressure difference between the two cells is then measured. This differential signal represents the absorption coefficient of the test gas. Using this design operating at a 1-Hz chopping frequency with an integration time of 2 minutes, the background signal was reportedly reduced to a value which corresponded to $3.3 \times 10^{-9} cm^{-1}$ per watt of laser power. One drawback of this scheme is the difficulty in matching the reference and sample chambers, both in magnitude and in the phase of the background signal.

By far the most popular approach to minimize background signal through cell design is the use of acoustically resonant detectors. In the nonresonant photoacoustic method originally proposed by Kreuzer (122), the optical excitation beam makes a single pass along the axis of the cylindrical sample cell. The modulation frequency, $\omega/2\pi = f$, is chosen to be sufficiently low that the magnitude of the pressure pulse within the tube at any instant is equal at all points. The microphone pressure is equal to the pressure increment induced by a single cycle of heating. In the acoustically resonant operation (128), the detector is designed as an acoustic resonance chamber so that the pressure fluctuations produced by spatially and temporally nonuniform excitation contribute to standing acoustic waves within the chamber. The excitation radiation, meanwhile, is modulated at a frequency which

is coincident with one of the natural resonant acoustic frequencies of the detector. Operating in this mode, the PAS signal is enhanced because each successive pulse contributes to a standing acoustic wave within the chamber, the magnitude of which is considerably greater than the pressure induced by a single cycle. The resonant enhancement can be measured by a factor called "acoustic Q", which is given by

$$Q = \frac{\omega_n}{\Delta\omega} \tag{2.15}$$

where ω_n is the resonant acoustic frequency, $\Delta\omega$ is the width of the standing wave at half maximum.

To determine the natural acoustic resonances of a cylindrical detector cell, a solution of the sound wave equation in cylindrical coordinates is required. There are oscillations in all three coordinate directions: longitudinal, azimuthal, and radial. These resonant frequencies are given by the equation (128)

$$\omega = \pi C_o[(k/L)^2+(a_{m,n}/R)^2]^{\frac{1}{2}} \tag{2.16}$$

where the integer eigenvalues, k, m, and n define the longitudinal, azimuthal, and radial modes, respectively, as depicted in Figure 11 and $a_{m,n}$ is the solution of the equation dJm/dr = o at r = R, the radius of the cylinder. Jm(z) is the mth order Bessel function of the argument at z, C_o is the speed of sound in the sample of gas in the chamber, and L is the length of the chamber. PAS operations based on longitudinal (156,164), radial (137,164), and azimuthal (138) modes of resonance have been reported.

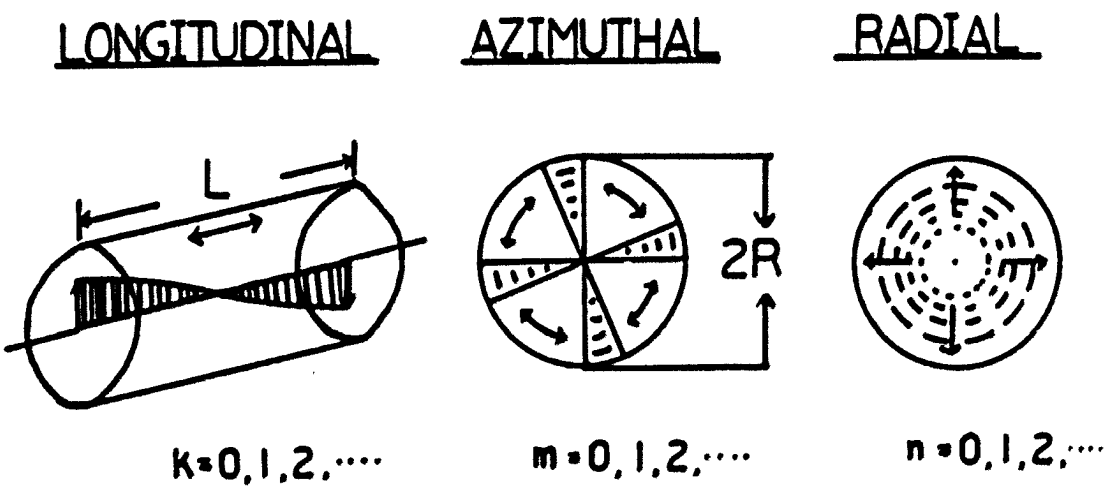

Figure 11. Longitudinal, azimuthal, and radial modes of a cylindrical sample chamber

In addition to the enhancement of the signal, resonant operation also reduces the window absorption background signal by locating the acoustic nodes of the standing wave on the windows, making the coupling between the pressure signal of the windows and the standing wave very inefficient. Moreover, it provides a means for the continuous monitoring of air samples. By placing the gas inlet and outlet where the standing wave has a node (window), air samples can be introduced into the cell in a flow-through fashion with minimal perturbation to the acoustic quality of the cell. Such a detector was in fact constructed and successfully demonstrated by Max and Rosengren (130). Shtrikman and Slatkine (136) also devised a resonant detector for continuous monitoring purposes. Their system operated in a windowless mode. By creating longitudinal standing waves with well defined nodes at points where the windows would normally be, they not only eliminated background signals caused by window absorption, but also solved the problem of power loss due to reflection. One drawback with continuous monitoring operation in this manner is the degradation of the acoustic quality of the cell because the inlet and outlet will constitute "pressure leaks".

Since the PAS signal is proportional to the power of the exciting beam, it is a natural extension to combine a resonant detection system with either intracavity or multipass operation. Leslie and Trusty (165) reported the operation of a resonant detector inside the cavity of a DF laser and demonstrated a detection limit of $7 \times 10^{-9} m^{-1}$ for a S/N of 1. The multipass resonant detector is judged as one of the most

promising designs for practical applications (129,164) and is expected to have a detection limit of sub-parts-per-billion per watt of laser power.

Despite their potential in S/N improvement, acoustically resonant detectors do have a few drawbacks. First of all, the natural resonance frequency is a function of the temperature and the gas composition of the sample. This makes it difficult to control the modulation frequency from one sample to the next. Secondly, the phase of the pressure signal around the resonance frequency is rapidly changing (127), thus putting a severe demand on the locking ability of the electronic device generally employed in PAS detection. Thirdly, the PAS signal strength is proportional to 1/f where f is the modulation frequency of the exciting beam. With the typical size of a resonant cell, the lowest natural frequency is usually above 1KHz while a nonresonant cell can use a modulation frequency as low as a few Hz to attain maximal signal strength, predominance of electronic noise at low frequencies notwithstanding. As a matter of fact, the most sensitive measurement reported to date was done with a carefully designed nonresonant cell employing six miniature microphones (166). Its minimum detectable absorption was $10^{-10}cm^{-1}$ per watt of laser power.

2. Different techniques for modulation

In a conventional PAS detection setup, the modulation of the exciting radiation is performed by a mechanical chopper. This type of periodic interruption of the beam from irradiating the sample is called

intensity modulation. An alternative to intensity modulation is to frequency-modulate the radiation source. Background signals due to radiation absorption in the detector windows and walls is proportional to the light intensity which is essentially constant with the small change of wavelength. This background signal is kept as a dc signal while the true photoacoustic signal produced by the absorbing gas is modulated at the frequency of modulation. By using a phase-sensitive detection device, the dc background can be rejected and only the true PAS signal is detected.

There are several ways to frequency-modulate the radiation source. The simplest way is called frequency switching, i.e. the source operates with constant output power on two discrete frequencies, one of them is coincident (or in near conincidence) with the absorption line of the monitored gas while the other is "off resonance". This is very similar to differential absorption techniques employed in long-path sensing of atmospheric pollutants (70). Frequency modulation can also be achieved by periodically shifting the laser frequency around the center of an absorption line of a monitored gas. This type of modulation has the best success with such tunable laser sources as semiconductor diode (69), and spin-flip Raman lasers (123). Modulation occurs in a sinusoidal fashion according to $\nu(t) = \nu_{\mu} (1+\mu\sin\omega t)$, where $\nu(t)$ = the laser line frequency, $\omega/2\pi = f$, modulation frequency, ν_{μ} = the laser line frequency around which the modulation occurs, and $\mu<<1$, normally. More commonly, the modulation is in the form of a small square wave superimposed on a current ramp which controls the laser output frequency,

as in Ref. 167. Photoacoustic detection schemes based on this type of frequency modulation are very similar to derivative spectroscopy used for high resolution studies. Dewey (168) has developed a simple theoretical model for frequency modulation in PAS techniques including derivative spectroscopy and wide modulation spectroscopy.

Modulation in PAS techniques is not necessarily confined to the radiation source. For molecules possessing a permanent electric or magnetic dipole moment the Stark or Zeeman effect may be used to perturb the molecular energy levels, and to tune some absorption lines into coincidence with fixed frequency lasers. The same perturbation can also be used to modulate the absorption in the PAS techniques. In these modulation modes, the spectral line of the absorbing species is shifted in and out of the laser frequency by applying a time-varying electric or magnetic field on the species. Photoacoustic signals due to the absorption of the monitored species will appear as an ac signal which can be detected by standard ac detection techniques. Since the laser radiation is incident on the cell consistently and unmodulated, the background signal due to window-absorption should be constant with the laser intensity and therefore, will not contribute to the detected signal. Both acoustical noise and light scattering due to mechanical chopping will also be eliminated. In addition, Stark and Zeeman modulations also provide a new degree of discrimination between molecules whose absorption spectra overlap, but exhibit different Stark or Zeeman effects. Discrimination will also be enhanced between signals due to

near-resonant weak absorption and signals due to the wings of a strong absorption line. These features become important in in situ type of monitoring of air samples as background interferences such as water vapor, aerosols, etc. will impose severe restrictions on the ability of the PAS system to detect trace amount of the gas molecules of interest.

Successful demonstrations of PAS detection systems based on Zeeman or Stark modulation have been reported. Boncyck and Ultee (132) and Kaldor et al. (133) used a magnetic field to Zeeman-modulate the frequency of a NO transition and a detection limit of a few ppm was obtained. Kavaya et al. (134) investigated the use of Stark modulation for PAS detection. Their results indicated that the background signal obtained by operating in this mode is 500 times less than that obtained by operating the same PAS detector in the conventional chopped radiation mode. The S/N was found to be greater in the Stark mode than in the chopped mode for pressures below 500 torr. The minimum detectable absorption strength was $1 \times 10^{-7} cm^{-1}$ per watt of laser power. There are other air pollutants which are suitable for quantitative Stark or Zeeman spectroscopy and are listed in Tables 2A and 2B.

The sensitivity of PAS detection based on Stark or Zeeman modulation depends on the extent of the modulation of individual molecules. Typical values of the extent of modulation are fairly limited because of the magnitudes of such molecular constants as electric dipole moment, magnetic moment, rotational constants, etc. (95,133). As a result,

Table 2A. Representative gases suitable for quantitative Stark spectroscopy

Molecule[a]	Laser
Acetonitrile	CO, Co_2
Acrylonitrile	CO_2
Allyl Chloride	CO_2
Formaldehyde	CO, CO_2
Methacrylonitrile	CO, CO_2
Methyl Chloride	CO_2
Methanol	CO_2
Tetrahydrofuran	CO_2
Tolulene	CO
Trichloroethylene	CO_2
Vinyl Chloride	CO, CO_2
Vinylidene Chloride	CO_2
Nitrobenzene	CO
Nitric Oxide	CO
Ozone	CO_2
Carbonyl Sulfide	CO_2
Methyl Fluoride (170)	CO_2
Ammonia (169)	CO_2
Carbon Monoxide (171)	PbSSe

[a]Unless otherwise stated, all molecules are cited from reference 95.

Table 28. Representative gases suitable for quantitative Zeeman spectroscopy

Molecule	Laser
Nitric Oxide (132,133)	CO
Nitrogen Dioxide (172)	CO_2, CO
Ammonia (173)	SbSnSe, PbSnTe
Sulfur Dioxide (174)	flash lamp source
Carbon Dioxide (175)	
Nitrous Oxide (175)	

frequency shifts by electric or magnetic fields are fairly small. For example, Stark shift in the most favorable case in NH_3 is 1.0×10^{-2}cm for an electric field of 1KV/cm (169). Typical values for the Zeeman shift in NO is $2.1 \times 10^{-3}cm^{-1}$ per KGauss (133). Large electric or magnetic fields are therefore required to ensure sufficient modulation depth. This can lead to two potential disadvantages: the difficulty in operating high fields at a frequency compatible with PAS techniques, and the introduction of additional noise in the microphone due to interactions between the electric or magnetic field and the microphone capacitance (134). There is yet another drawback common to the PAS technique based on frequency modulation as well as Zeeman or Stark modulation. This is the fact that to achieve high

resolution necessary for sufficient modulation depth, gas samples must be at low pressures to reduce the effect of pressure broadening (65). The PAS signal, however, in certain cases is dependent on the total pressure (158), and detectability may thus be compromised.

F. Conclusion

In this chapter, the theory of photoacoustic signal generation was presented along with the signal's dependence on such variables as pressure, modulation frequency, cell dimension, light intensity, and concentration of absorbing species. A brief discussion of the various noise and background contributions to the PAS signal was also included and the methods suggested for discriminating against background signal due to absorption by cell windows and walls were surveyed. While there are certain advantages to each of these methods, there are concomitant drawbacks which limit their uses in PAS detection.

In the next chapter, a promising scheme for reducing background contribution, wavelength modulation, will be presented along with experimental results to illustrate its operation in PAS detection.

III. PHOTOACOUSTIC SPECTROSCOPY IN GASES BASED ON WAVELENGTH MODULATION

A. Introduction

Wavelength or frequency modulation has long been a useful technique for improving the selectivity of a number of analytical methods based on optical spectrometry (176). It basically involves the following operation: the wavelength to which the monochromator (or filter, laser, or interferometer) is tuned is repetitively and rapidly scanned back and forth over a small spectral interval called the modulation interval, $\Delta\lambda$. In the photodetector signal, this results in a ripple or alternating current (ac) component that can be isolated and measured electronically. The success of this technique is predicated on the fact that there is a change in intensity or absorbance with wavelength.

One of the most popular applications of wavelength modulation is in the measurement of the intensity of a weak line superimposed on an intense and unstable spectral background in vapor phase atomic spectroscopy. The background arises as a result of the turbulent nature of the atomization device, or the complexity of the sample matrix and is usually broad and unstructured. The comparatively narrow atomic lines can be extracted and measured if the wavelength is modulated, say, sinusoidally, over an interval $\Delta\lambda$ centered on the desired line. The background by itself will generate an ac component in the signal at the same frequency as that of the applied wavelength modulation. The spectral line of interest, on the other hand, will

appear as a second harmonic component at twice the modulation frequency. The amplitude of this second harmonic component will remain unchanged even if the background fluctuates or drifts in intensity. This technique has been applied to the measurement of atomic emission in flames (177), graphite furnace atomizers (178), and plasmas (179), atomic absorption in flames (180) and in graphite furnace atomizers (181), and for atomic fluorescence in flames (182).

Wavelength modulation can also be applied in a square-wave fashion. Goff and Yeung (183) have reported a wavelength - modulated detection scheme for atomic fluorescence. By using a commercial electro-optical tuning element to provide two output wavelengths separated by 10 Å with a CW dye laser as the source for excitation of atoms in a premixed flame, they were able to eliminate most of the background emission in the flame as well as the background due to light scattering.

In addition to its capability of compensating for broad-band background spectral interference, wavelength modulation has the unique ability to correct for direct spectral line overlaps as well. Such overlaps occur occasionally in the analysis of alloys and other materials containing large concentrations of transition metals whose spectra are very complex. For example, the determination of traces of zinc in high-purity copper metal cannot be done directly by atomic absorption because copper has a weak absorption line only 0.003 nm away from the zinc 213-nm line, the only useful zinc absorption line. Since

the widths of the lines are about the same as the separation between them, increased spectrometer resolution alone cannot eliminate the interference. With conventional methods, a prior separation is necessary. Wavelength modulation, however, can be used to correct this interference, allowing a direct analysis without separation. The width and position of the modulation interval can be carefully adjusted so that the analyte peak generates a predominantly first harmonic signal, whereas the interfering peak generates a purely second harmonic signal with no first harmonic component. Subsequent selective detection of the first harmonic component would result in a signal due only to the analyte peak. This approach has actually been used to measure the zinc contamination in NBS Benchmark Copper without prior separation (184).

In the infrared region, wavelength modulation has also found extensive use (69,70,113,114). This is especially true in the long path monitoring of atmospheric pollutants. The benefits that can be derived from wavelength modulation include the potential reduction in background noises caused by atmospheric turbulence, and by scattering from aerosols.

Hinkley (69) used wavelength modulation in conjunction with a tunable $Pb_{0.93}Sn_{0.07}Te$ diode laser operating around 8.8 um to scan several lines in the ν_2 band of SO_2, a common pollutant usually present in smoke stack effluents. Ku et al. (70) have measured changes in transmission of 0.3% for pathlengths up to a few hundred

meters at atmospheric pressure using a derivative/ratio technique. A detection limit of 5 ppb of CO over a 0.61 km path has been obtained. Reid et al. (113,114) reported the detection of a number of pollutants in the ppb and sub-ppb range by a multipass cell with an effective pathlength of 100 meters at a reduced pressure of around 10 torr using a second-harmonic technique.

The benefits derived from wavelength modulation, namely, better specificity and background reduction, can in principle be translated into photoacoustic techniques. Indeed, this combination has been explored (167,185). Chang (167) used a diode laser operating in a square-wavelength-modulated mode to measure NH_3 photoacoustically. A signal-to-noise ratio improvement of 3 over the conventional PAS detection technique was obtained. Castleden et al. (185) modified a conventional photoacoustic spectrometer to perform wavelength modulation on the continuum radiation from a 300-W xenon arc. First and second derivative spectra of solid samples were obtained with apparent enhancement in the resolution of the system as well as increased precision in locating the position of absorption band edges and maxima and minima.

While it is possible to take advantage of the unique combination of photoacoustic measurements with wavelength modulation, the means to produce the latter are quite different in the visible and the infrared regions. In the visible region, among the experimental techniques used to produce wavelength modulation are:

(1) Vibration or oscillation of the slits, mirror, grating or prism of the monochromator.

(2) Oscillation of an interference filter.

(3) Oscillation of a Fabry-Perot interferometer or an etalon.

(4) Insertion of an oscillating or rotating refractor plate in the light beam inside the monochromator.

The relative advantages of these different approaches are compared in literature (186).

In the infrared region, the types of lasers available and the spectral line widths involved do not allow simple adaptation of techniques that work in the visible region. Diode lasers (113,114,167) can be wavelength modulated by imposing current pulses (either sinusoidal or square wave) on the current ramp which controls the output wavelength of the lasers, but their low powers have thus far limited their use in photoacoustic pollution applications. The spin-flip Raman laser has the potential for wavelength modulation. By imposing a time-varying magnetic field which governs the separation in the energy levels of the semiconductor crystal, the output wavelength of a SFR laser can be made to oscillate over a small spectral interval. The instrumentation involved however, is too complex for routine use. Color-center lasers (187) are similar to other visible lasers, but the output wavelengths are broad (ca. 0.1 cm^{-1}) and have yet to span the "atmospheric window" region. It is therefore of interest to develop wavelength modulation schemes based on discrete-line, moderate-power continuous wave gas lasers

such as the one reported in the next section, the CO_2 laser. The inherent widths of these lines are of the order of a few megahertz, so that modulation must involve consecutive vibration-rotation lines rather than be within the normal gain curve of a laser line.

When the laser is modulated by a square wave of frequency ω, the output waveform can be described as:

$$\lambda(\omega=0 \text{ to } \pi) = \lambda_1$$

$$\lambda(\omega=\pi \text{ to } 2\pi) = \lambda_2$$

If such a laser is used as the excitation source for photoacoustic spectrometry and is tuned such that λ_1 is in resonance with the molecular transition of the species of interest, and λ_2 is off resonance, then the resulting signal falling on the microphone can be given as:

$$I_{\lambda 1} = I_{PA}(\sigma\lambda_1)+I_B$$

$$I_{\lambda 2} = I_{PA}(\sigma\lambda_2)+I_B$$

where: $I_{PA}(\sigma\lambda_1)$ = photoacoustic signal amplitude at λ_1

$I_{PA}(\sigma\lambda_2)$ = photoacoustic signal amplitude at λ_2

$\sigma\lambda_1$, $\sigma\lambda_2$ = absorption coefficients at λ_1, and λ_2, respectively

I_B = acoustic signal due to background, including windows and cell wall heating.

Since the P.A. signal is proportional to the absorption coefficient, and λ_1 and λ_2 are selected such that $\sigma_{\lambda_1} >> \sigma_{\lambda_2}$, these two signals can be subtracted electronically with a lock-in amplifier to give a net signal

$$I_{net} = I_{\lambda_1} - I_{\lambda_2} = I_{PA}(\sigma_{\lambda_1})$$

which is independent of the background signal. The above expression is true only if the laser power is equal at the two λ's, and I_B is independent of the wavelength.

The evaluation of such a scheme based on wavelength modulation has been performed using a continuous wave CO_2 laser for the photoacoustic determination of ethylene, C_2H_4, and is described here.

B. Experimental

A schematic of the experimental arrangement for this work is shown in Figure 12. The individual components are summarized in Table 3. The details of some important components are given as follows.

1. Laser and wavelength modulation

The laser used is a continuous wave (CW) CO_2 laser of conventional design (Molectron, Sunnyvale, CA, Model C-250) with a flowing gas mixture of about 15 torr He and 2 torr CO_2. The output wavelengths range from 9.17 to 9.80, and 10.13 to 10.91 um. Figure 13 depicts the three vibrational levels that participate directly in most of the laser emissions: the initial (or upper) level (00°1) and one of the two final (or lower) levels, (10°0) giving the 10.6 um band, or (02°0) giving the 9.6 um band (see

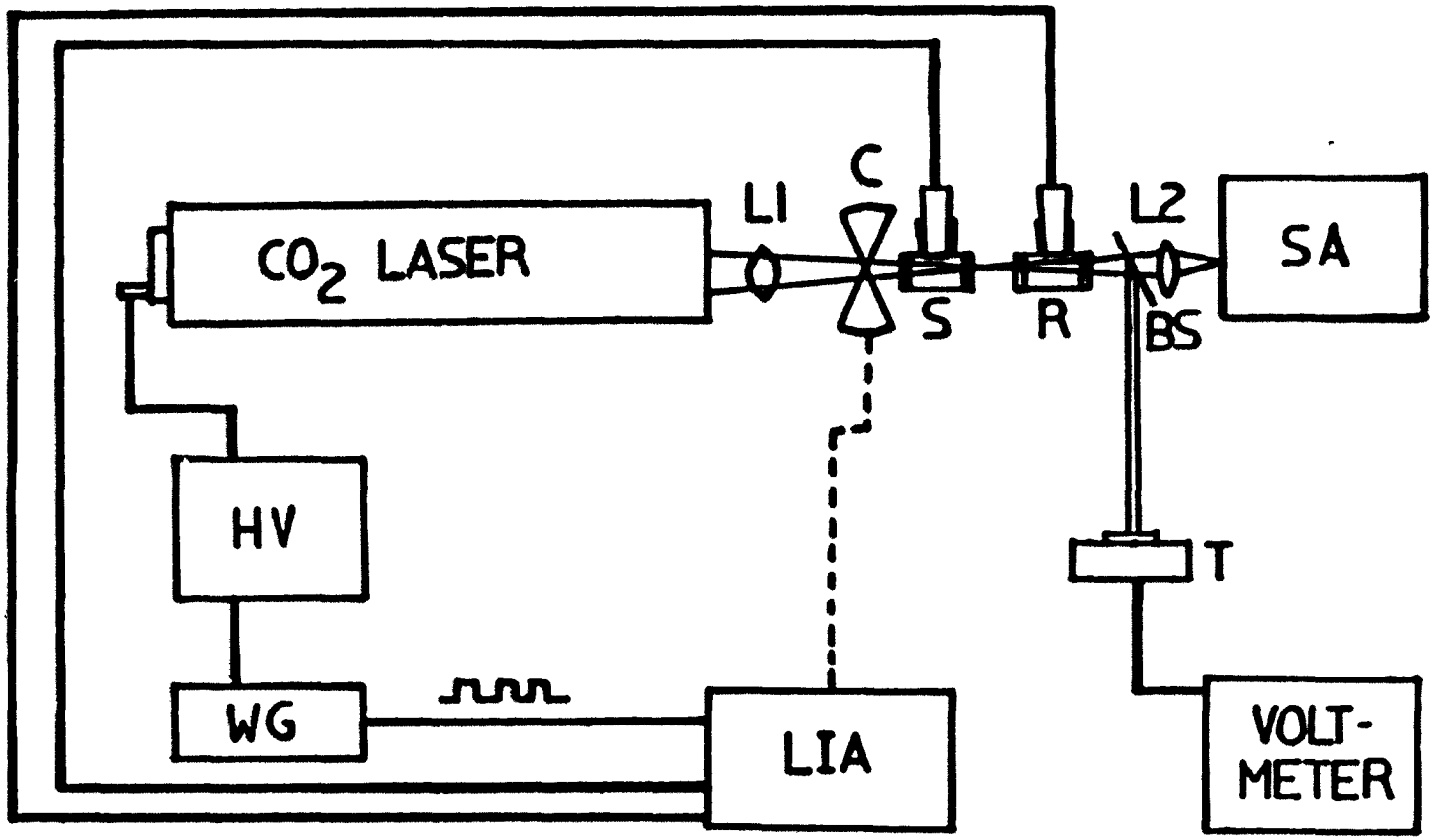

Figure 12. Schematic representation of the set-up for the PAS experiment. HV-high voltage operational amplifier; WG-wave generator; LIA-lock-in amplifier; L1, L2- focusing lenses; S- sample cell; R- reference cell; BS- beam splitter; SA- Spectrum analyzer; T- thermopile; C- Chopper, optional

Table 3. Experimental components for photoacoustic detection based on wavelength modulation

Component	Model No.	Manufacturer
CO_2 laser	C-230	Molection, Sunnyvale, CA
PZT pusher	PZ-44	Burleigh, Fishers, NY
Wave generator	162	Wavetek, San Diego, CA
High voltage operational amplifier	PZ-70	Burleigh, Fishers, NY
Mechanical chopper	7500	Rofin, Newton Upper Falls, MA
Microphone	BT-1759	Knowles Electronics, Franklin Park, IL
Thermopile	210	Coherent Radiation, Palo Alto, CA
Microvoltmeter	155	Keithley Instruments, Cleveland, OH
CO_2 Spectrum analyzer		Optical Engineering, Santa Rosa, CA
HeNe laser	134	Spectra Physics, Mountain View, CA
Lock-amplifier	HR-8	Princeton Applied Research, Princeton, NJ
Capacitance monometers	221A	MKS Instruments, Burlington, MA
Thermocouple couple gauge	0531	Varian, Lexington, MA
Chart recorder	B5117-5I	Houston Instrument, Austin, TX

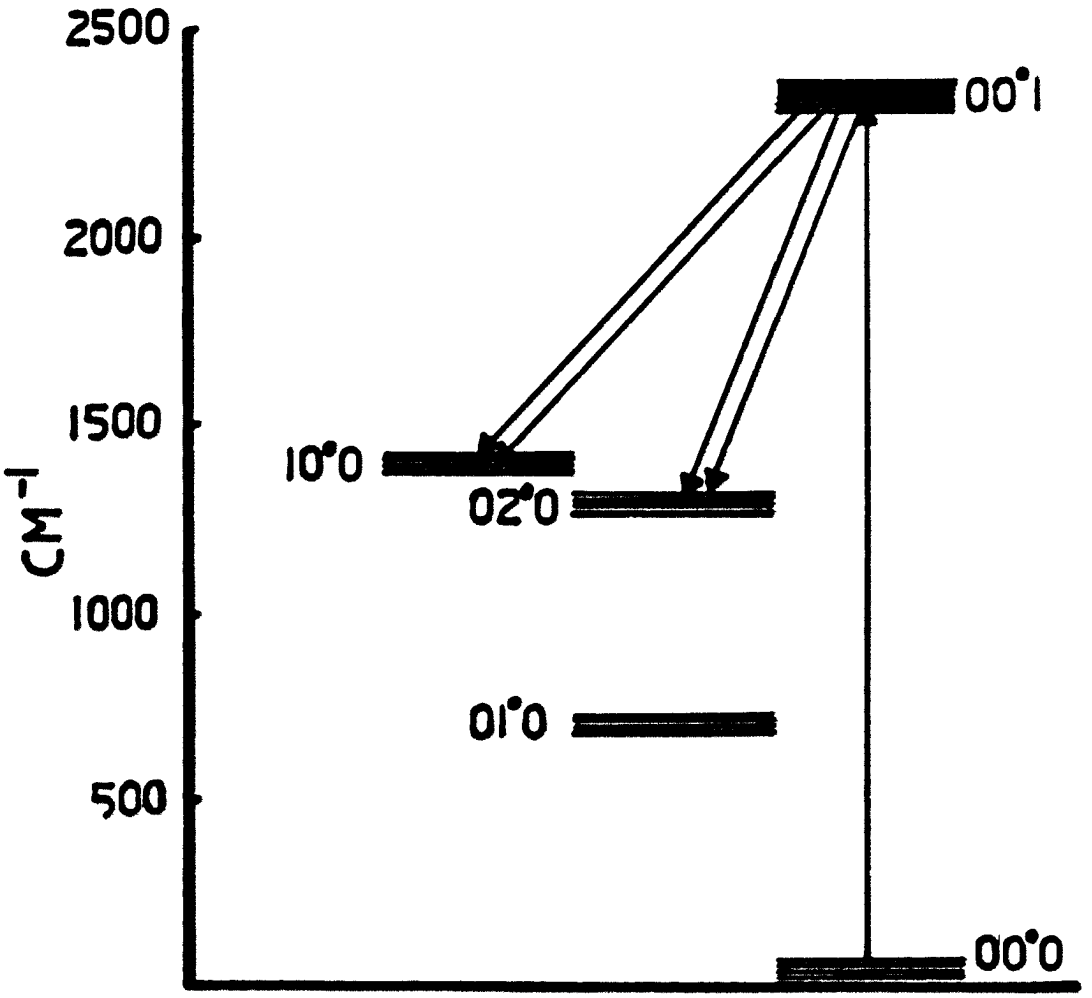

Figure 13. CO_2 laser energy levels

Figure 13). Because the rotational sublevels in the vibrational levels are closely coupled together through collisions, only one line oscillates at one time, however, a grating can be used to select a particular line. In the absence of a tuning device, a line in the higher gain 10.6 um band oscillates preferentially to the 9.6 um band. With a grating inside the laser cavity, any of the R and P branch lines with sufficient gain in each vibrational band can be selected. The CO_2 laser gain curve is shown in Figure 14.

Even though the laser is capable of 50 W output at the main laser lines (10.6 um band), only 2-3 W was used in this study. The laser is equipped with 80 lines/mm (=1/d) grating and a piezoelectric transducer to fine-tune the cavity length. Since it is necessary to tune from one rotational line to the next (see Figure 14), modulation of the grating angle at a fixed cavity length seems best. To go from, for example, λ = 10.513 um to λ = 10.532 um, corresponding to the P(12) and P(14) lines, respectively, the grating equation for the Littrow arrangement,

$$\lambda = 2d \sin \theta,$$

shows that the angle must change approximately 8.4×10^{-4} rad. For the grating mount in this laser, this translates to a 113 um movement (horizontal) on a 13.5 cm center. This is schematically represented in Figure 15.

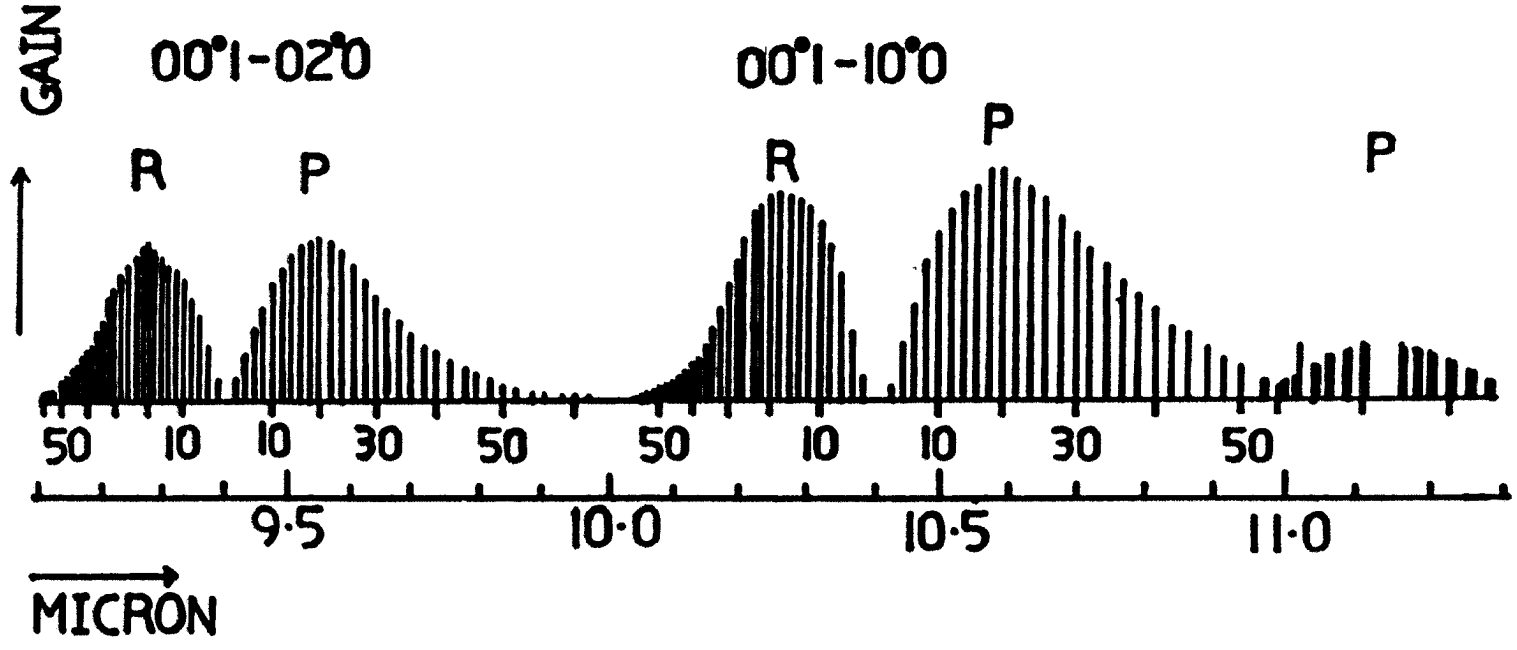

Figure 14. CO_2 laser gain curve

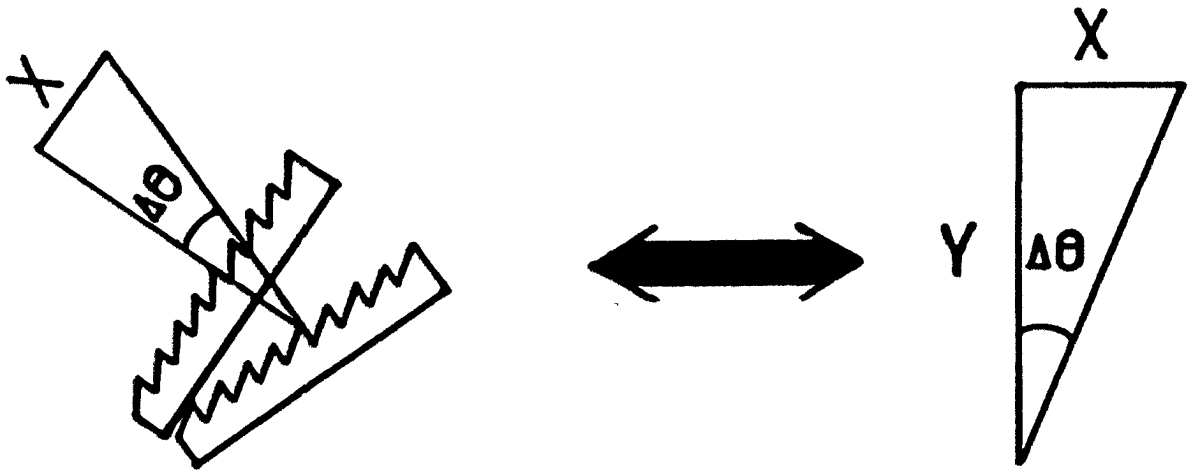

$\lambda = 2d \sin \theta$

for $\lambda_1 = 10.513\ \mu m$ (P(12))

$\lambda_2 = 10.532\ \mu m$ (P(14))

λ_2 to $\lambda_1 \rightarrow \Delta\theta = 8.4 \times 0^{-4}$ rad

$X = y(\Delta\theta)2\pi$

$= 113\ \mu m$ for $y = 13.5$ cm

Figure 15. Schematic representation of the vibrating grating mount. X-horizontal movement; Y-vertical length from center; $\Delta\theta$-angular movement

To achieve this range of length of travel, a piezoelectric (PZT) pusher (Burleigh, Fishers, NY, Model PZ-44) is used in place of one of the original mirror-alignment adjustment screws. The actual mechanical modifications are shown in Figure 16.

To operate, a square wave of the chosen frequency (100 Hz in this case) is derived from a wave generator (Wavetek, San Diego, CA, Model 162) and amplified by a high-voltage operational amplifier (Burleigh, Fishers, NY, Model PZ-70). At the same time, the square wave is used to provide synchronization to the lock-in amplifier. The laser power is monitored by a thermopile detector (Coherent Radiation, Palo Alto, CA, Model 210) inserted into the light beam. Only the average power is measured. The wavelength output of the laser is monitored after the sample cell by a spectrum analyzer (Optical Engineering, Santa Rosa, CA) which was previously calibrated with a HeNe laser (Spectra Physics, Mountain View, CA, Model 134). Measurements are also made in the amplitude modulation mode for control study purposes. This is accomplished by placing a mechanical chopper (Rofin, Newton Upper Falls, MA, Model 7500) in front of the laser beam. The slots of the chopper are larger than the CO_2 laser beam size to ensure a square wave modulation.

2. PAS cell

The design of the PAS cell is conventional (nonresonant) and is shown in Figure 17. The cell is made of pyrex glass with KCl windows glued to the ends. The transmittance of these windows are tested and

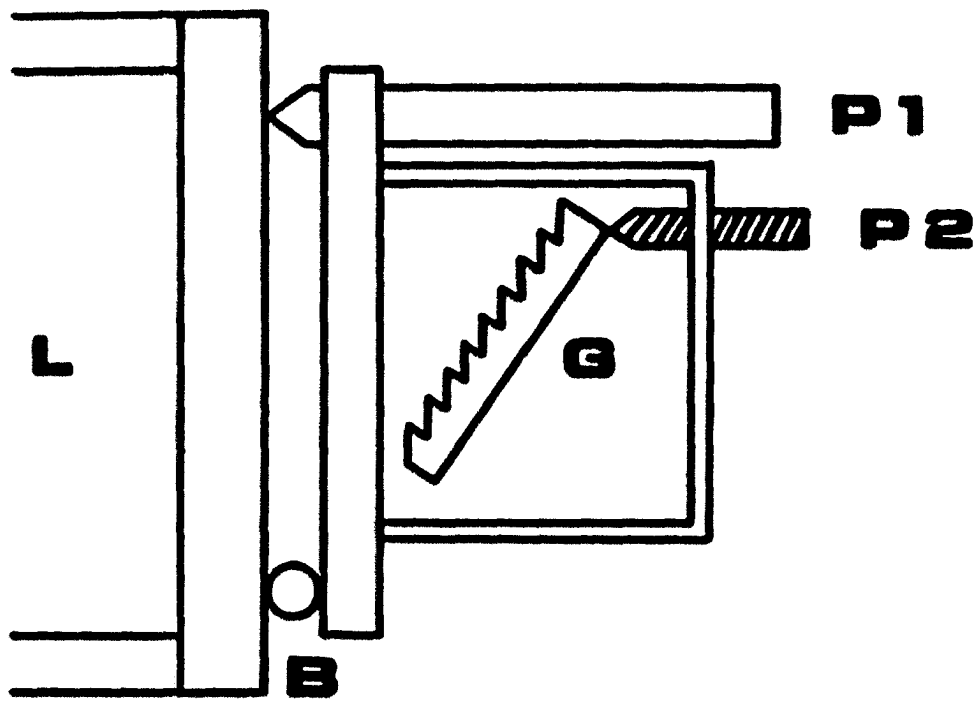

Figure 16. Mechanical arrangement for wavelength modulation. P1-piezoelectric pusher; P2-coarse adjustment screw; G-grating; L-laser cavity; B-ball bearing

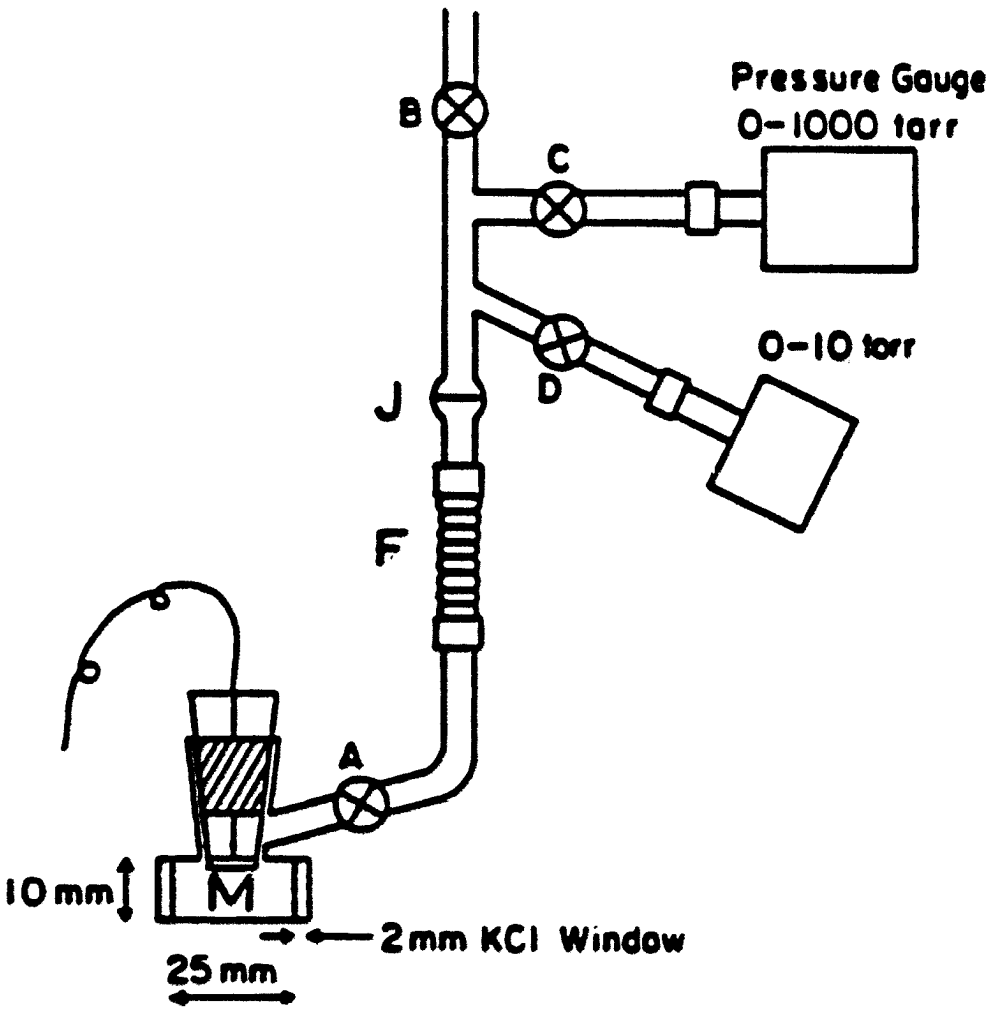

Figure 17. Photoacoustic cell. A through D-vacuum stopcocks; J-o-ring glass joint; F-flexible stainless steel coupling; M-microphone

found to be > 90%. The cavity of the cell is 25 mm long and 10 mm in diameter. The microphone used in this study is a Knowles Electronics BT-1759 miniature electret microphone with a built-in FET preamplifier. It is biased as suggested by the manufacturer. The dimensions, wiring and sensitivity curve of this microphone are shown in Figure 18. It has an overall response of 10 mV/Pa, and a broad band rms noise level of about 6.5 uV. The frequency response is flat between 100 Hz and 3 KHz. By using a lock-in amplifier tuned to the modulation frequency, the microphone noise level is reduced dramatically. The output independence of this microphone is from 2000 to 6000 ohms (3500 ohms nominally).

The microphone is mounted to the bottom face of a standard taper joint (14/35) with the wires feeding through a small opening to provide a vacuum seal. When the joint is inserted into the receptacle, the microphone is flush with the inner wall of the PAS cell and its position is midway between the cell windows. The output of the microphone (plus preamplifier) is connected directly to a lock-in amplifier (Princeton Applied Research, Princeton, NJ, Model HR-8), without any special device to match the impedances. A 1-s time constant was used throughout.

The cell is isolated from mechanical vibrations in the vacuum system by a piece of flexible tubing and from acoustical noise from the pump by turning off the stopcocks during measurements. To isolate the cell mechanically from the work bench, all support is through layers of different foam packing materials.

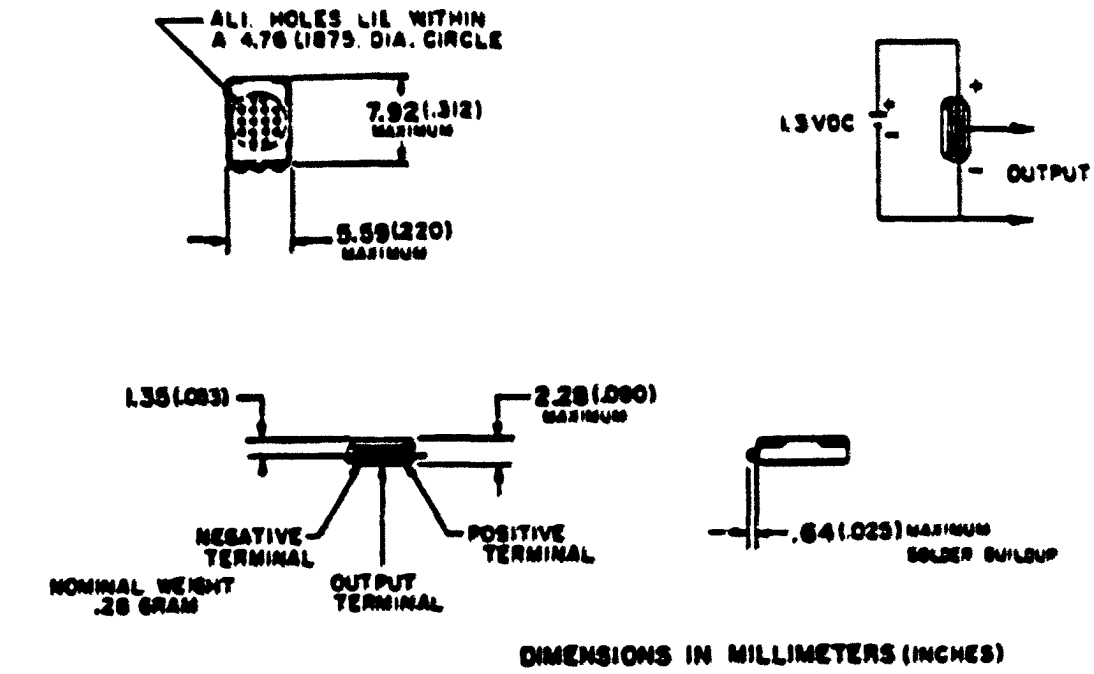

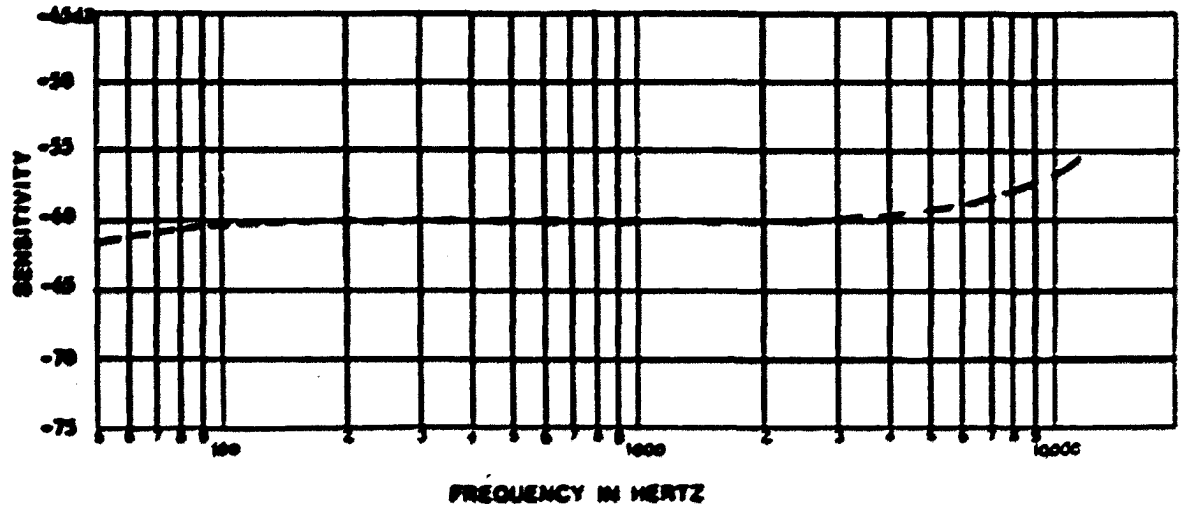

Figure 18. The dimensions, wiring and sensitivity curve of the Knowles BT-1759 electret microphone

3. Gas handling

The absorbing species chosen for this work is ethylene, C_2H_4. Samples of different concentrations were prepared from reagent grade gas (Matheson, E. Rutherford, NJ) without further purification. The buffer gas used was N_2. Mixtures down to 10 ppm were prepared by direct reading on a thermocouple gauge (Varian, Lexington, MA, Model 0531 with 801 electronics). The total pressure throughout the study is 760 torr. Below the 10 ppm level, mixtures were prepared by expansion of a 10 ppm mixture into calibrated volumes. For example, to go to 1 ppm from 10 ppm, the 10 ppm mixture (presumed to be homogeneous) at a total pressure of 760 torr, is evacuated from the cell until the total pressure is 76 torr. The cell is then refilled with pure N_2 to a pressure level of 760 torr again. To ensure there is no memory effects in the vacuum line, sufficient time was allowed for equilibration of the partial pressures before each experiment. The time required ranges from 10 to 24 hours. The more diluted the sample, the longer the time needed to minimize the memory effects from the previous mixture. All pressures are measured with a capacitance mamometer with 0-10 torr and 0-1000 torr full scales (MKS Instruments, Burlington, MA, Model 221A). Photoacoustic measurements were made in a static mode, i.e. all inlets leading to the cell were closed.

C. Results and Discussion

Photoacoustic signals of C_2H_4 were measured for both the wavelength and amplitude modulation modes. The laser lines chosen for wavelength modulation were the P(12) and P(14) lines in the 00°1 - 10°0 band. For control studies, the P(20) and P(22) lines were also used. A comprehensive list of absorption coefficients at various CO_2 laser wavelengths, measured by PAS, is available in the literature (188). Table 4 lists the four that were used in this study. The magnitude of the PAS signals, normalized by laser power, is presented in Table 5. The lock-in amplifier output signals for the 4.3 to 0.040 ppm mixtures are presented in Figure 19.

1. Extent of modulation

The first item of concern is the actual extent of modulation provided by this design. As discussed in the introduction section of this chapter, the success in reducing the background signal depends on the ability of the design to furnish two laser lines, P(12) and P(14), with equal power. That is, the mechanical movement provided by the PZT pusher must be large enough to force lasing in each of the two lines and must be centered so that equal powers are obtained in each half cycle of the modulation. This is complicated by the fact that adjacent CO_2 laser lines need not possess the same gain (see Figure 14). A good approximation is to reduce the wavelength modulation frequency to the order of 1 Hz so that a direct judgment can be made.

Table 4. List of absorption coefficients of ethylene at CO_2 laser wavelengths used in this study

Wavelength (μm)		Absorption in coefficient $(atm.cm)^{-1}$
P(12)	10.513	4.70
P(14)	10.532	32.17
P(20)	10.591	1.50
P(22)	10.611	1.42

Table 5. PAS signal normalized for laser power

concentration (ppm)	wavelength modulation signal (uv/w)	amplitude modulation signal at P(14)(uv/w)
100	4660	11800
40	2120	5420
10	974	1841
6	494	1020
4.3	383	808
0.90	110	735
0.53	68.4	612
0.17	45.9	474
0.076	29.0	579
0.040	14.1	467

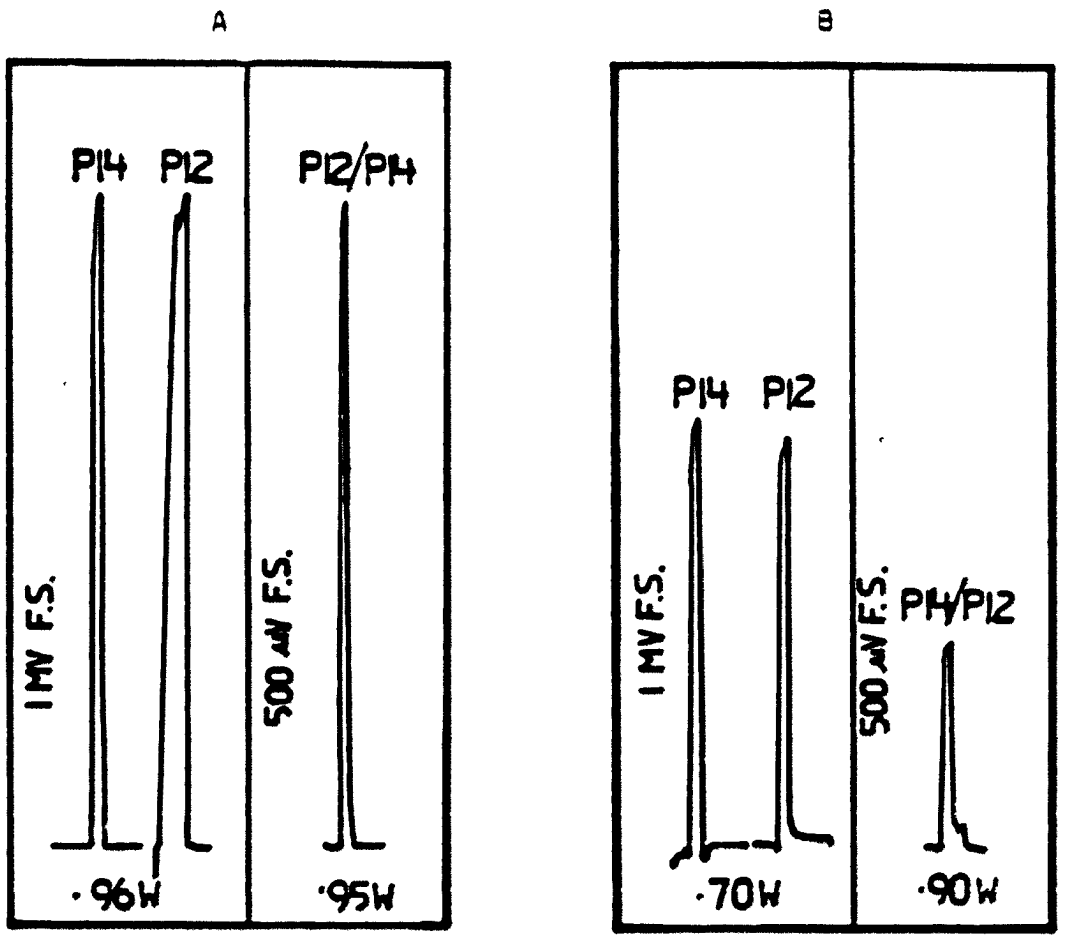

Figure 19. Comparison of photoacoustic signals. A,B. Photoacoustic signal for C_2H_4/N_2 mixtures. Lock-in amplifier output for A) 4.3 ppm B) .90 ppm. Left -amplitude modulation; Right -wavelength modulation

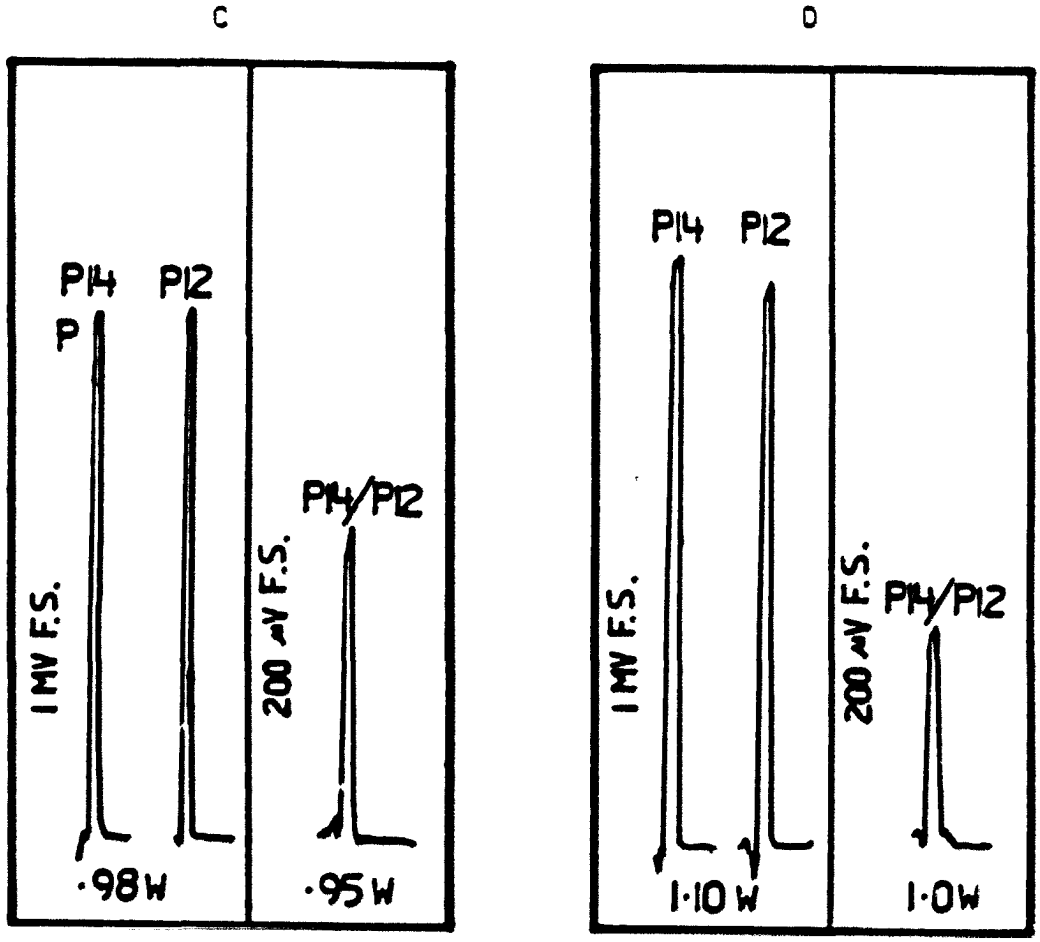

Figure 19. Comparison of photoacoustic signals. C,D. Photoacoustic signal for C_2H_4/N_2 mixtures. Lock-in amplifier output for C) .53 ppm D) .17 ppm. Left -amplitude modulation; Right -wavelength modulation

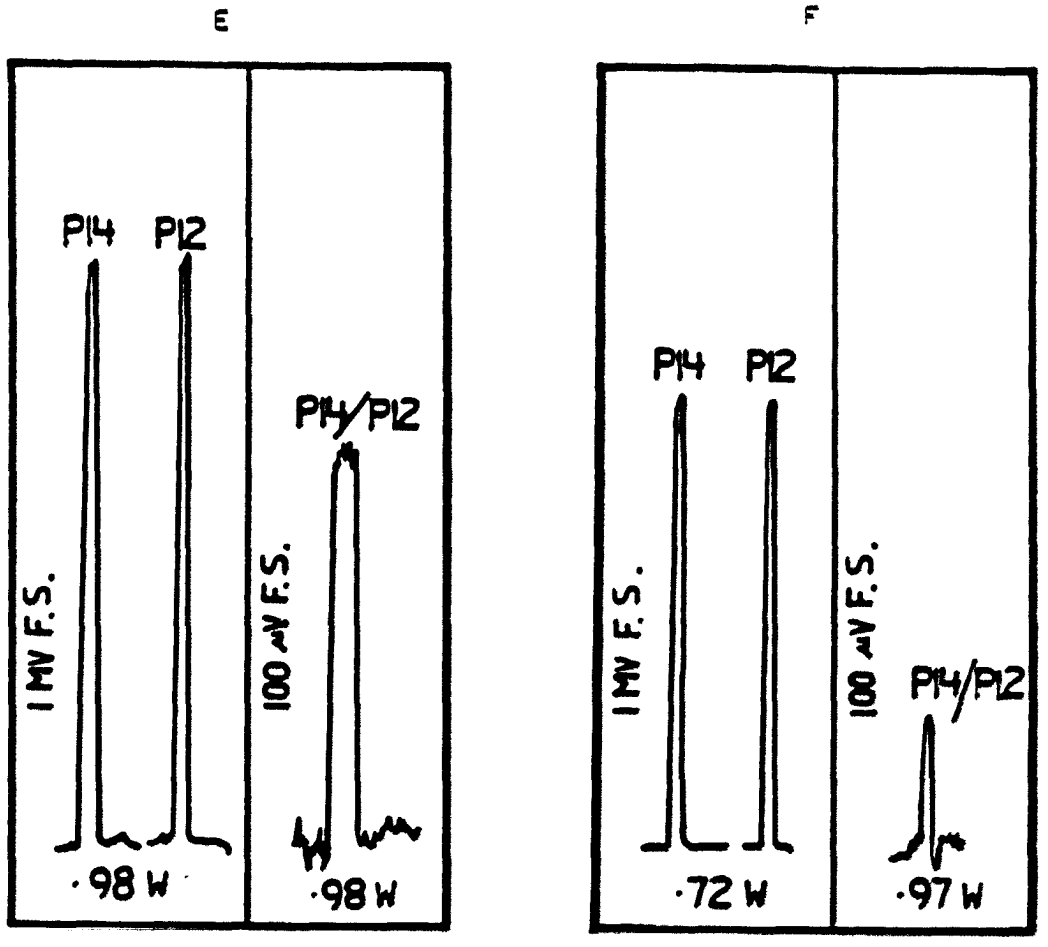

Figure 19. Comparison of photoacoustic signals. E,F. Photoacoustic signal for C_2H_4/N_2 mixtures. Lock-in amplifier output for E) .076 ppm F) .040 ppm. Left -amplitude modulation; Right -wavelength modulation

In looking through the spectrum analyzer, one can in fact see the two laser lines switching alternately with the applied square wave. The initial centering of the modulating position is achieved through adjusting the mirror-alignment screws of the grating mount. Finer adjustment is accomplished by the DC bias level on the PZT pusher available through the high-voltage operational amplifier (op amp). The entire waveform and the resultant wavelength output are schematically represented in Figure 20. The approximate center is located by observing the reading on a power meter (connected to the thermopile detector) with a sub-second response, such that the output level is essentially constant. In addition to these initial adjustments, it is necessary to check the transverse mode structure of the laser beam during modulation. Since the goal is to equalize the unwanted background in the PAS cell, the spatial characteristics of the laser beam must remain unchanged in each of the two half-cycles. This is accomplished by observing the far-field pattern of the beam (burn-pattern on a wood tongue depressor).

When the modulation frequency was increased to the order of 100 Hz, a couple of problems appeared. First, the high-voltage op amp used to provide the square waveform voltage to the PZT pusher is designed to drive a high capacitance load at high rates of speed. It does, however, have an automatic overload protection feature which will clip the output to limit the current to 20 mA RMS in case of a short or accidental overload. When the modulation frequency was brought up to 100 Hz, the overload protection was activated and the output voltage of

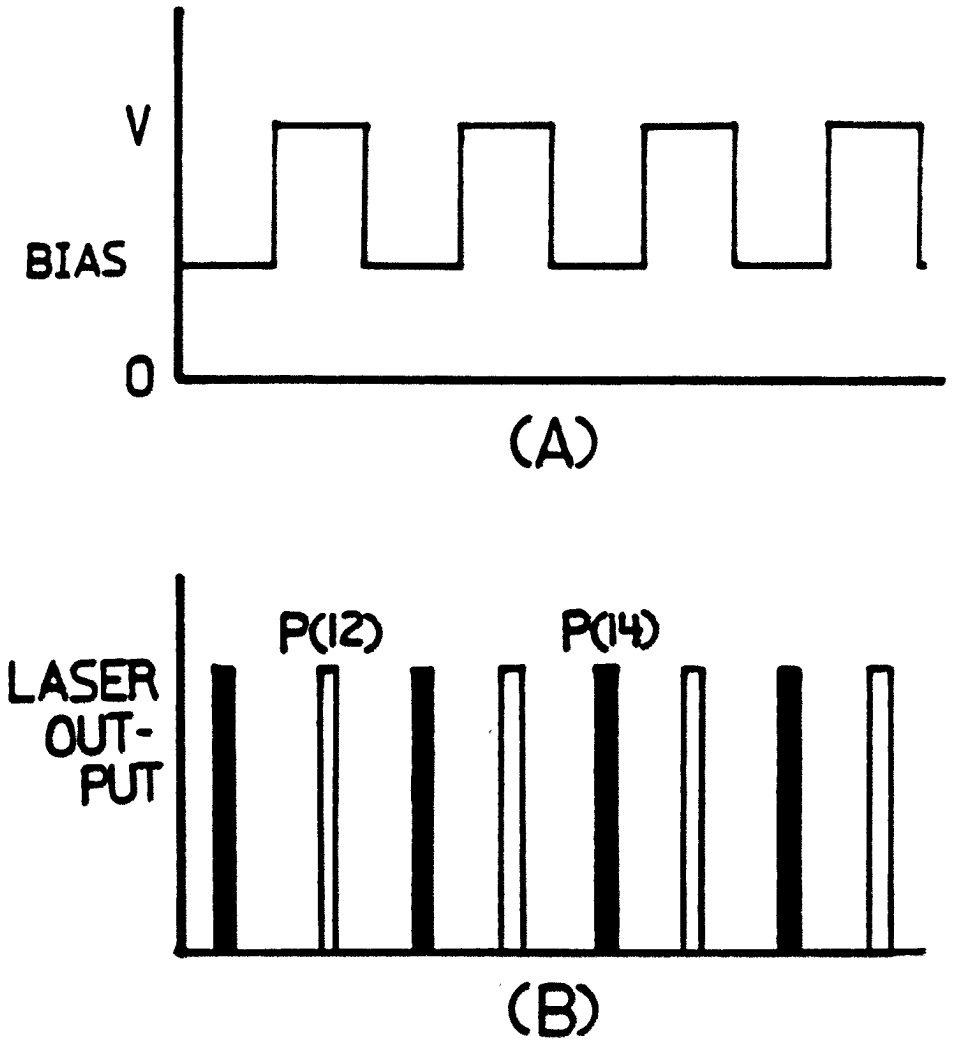

Figure 20. Schematic representation of wavelength modulation. (A) Modulation waveform; BIAS-DC bias voltage level; V-AC modulation voltage, (B) Resultant CO_2 laser output, assuming 100% modulation

the op amp dropped to zero, thus terminating the modulation. The cause of this phenomenon was initially thought to be due to the fact that the required current magnitude to drive the capacitive load of the PZT pusher exceeded the capability offered by the high-voltage op amp. To verify if this is indeed the case, the following calculations was performed.

Suppose Vm is the peak voltage (modulation voltage), f is the modulation frequency, then for a sinusoidal waveform, the voltage V at any instant t is given as (189)

$$V = Vm \sin 2\pi ft \tag{3.1a}$$

If C is the capacitance of the PZT pusher, then the charge Q on the capacitor is

$$Q = CV \tag{3.1b}$$

$$Q = CVm \sin 2\pi ft \tag{3.1c}$$

The current flowing at any instant, I, is equal to the rate at which the capacitor is being charged or discharged. Thus,

$$\begin{aligned} I &= \frac{dQ}{dt} \\ &= \frac{d}{dt}(CVm \sin 2\pi ft) \\ &= 2\pi f\, CVm \cos 2\pi ft \end{aligned} \tag{3.2}$$

For maximum current requirement, equation (3.2) becomes

$$I_{max} = 2\pi fCVm \tag{3.3}$$

Using typical values of Vm = 200 V, f = 100 Hz, C of PZT pusher = 95 nf, I_{max} is calculated to be about 11 mA. This value is less than the 20 mA RMS specified and, therefore, well within the capability of the high-voltage op amp. However, the preceding calculations were based on a sinusoidal waveform. In our study a square waveform was used to provide modulation. A square waveform may be considered the sum of one or more sinusoidal waves superimposed on each other. Specifically, it may be represented by the following equation (190), which contains only odd harmonics of sine waves:

$$F(2\pi ft) = \frac{4}{\pi}[\sin(2\pi ft) + \frac{1}{3}\sin(6\pi ft) + \frac{1}{5}\sin(10\pi ft) + \ldots\ldots + \frac{1}{n}\sin(2\pi nft)] \qquad (3.4)$$

This is illustrated graphically in Figure 21. It is evident that the addition of higher harmonics causes sharpening of the edges and flattening of the tops of the square wave. An ideal square wave can therefore be approximated to any desired degree of accuracy by the inclusion of a suitable number of high-frequency components of a sine wave. Consequently, when calculating the maximum driving current required for a square wave modulation from equation (3.2), the high-frequency components have to be included, making I_{max} considerably larger than the 20 mA RMS allowed by the high-voltage op amp.

To circumvent this problem, a trapezoidal waveform was used instead of a square one (see Figure 22). The current required to drive the PZT pusher, and hence the ability of the high voltage op amp to provide such a current, depends on the combined magnitude of the modulation frequency

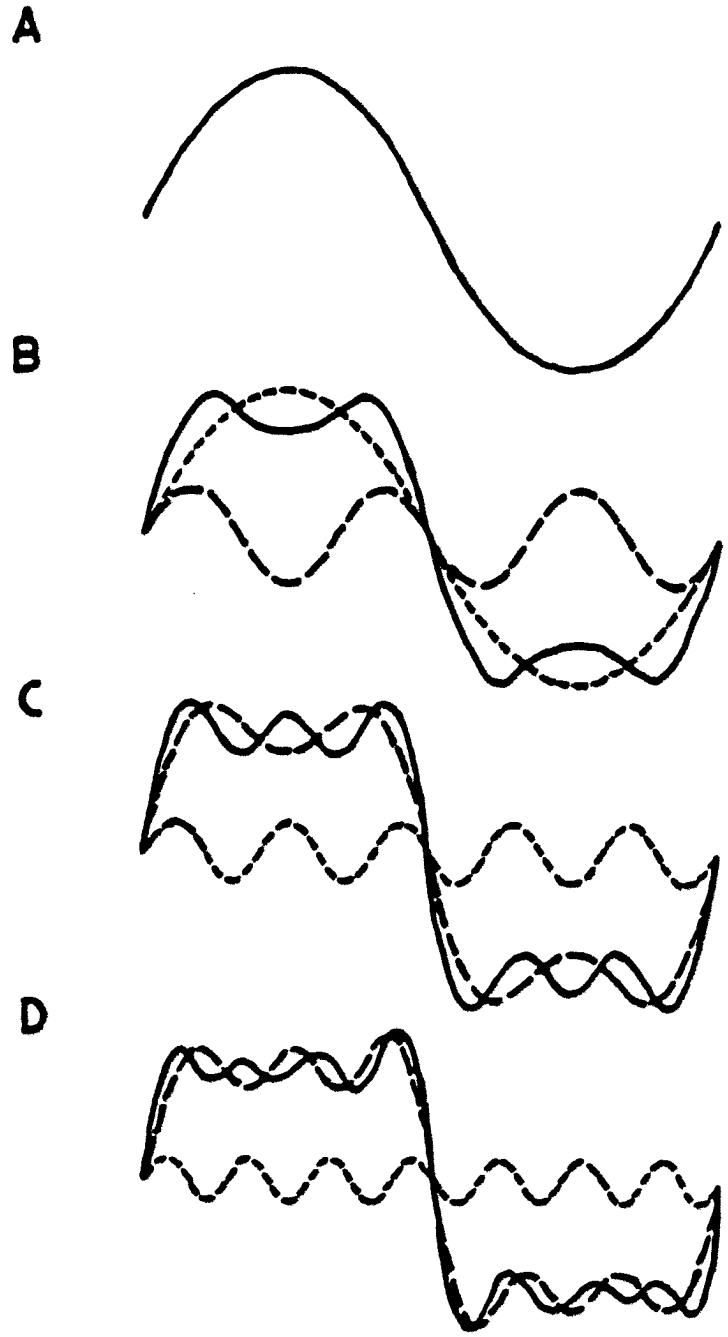

Figure 21. Approximation of a square wave by summation of a few sinusoidal components. A-$\sin(\omega t)$; B-$\sin(\omega t) + 1/3\sin(3\omega t)$; C-$\sin(\omega t) + 1/3\sin(3\omega t) + 1/5\sin(5\omega t)$; D-$\sin(\omega t) + 1/3\sin(3\omega t) + 1/5\sin(5\omega t) + 1/7\sin(7\omega t)$

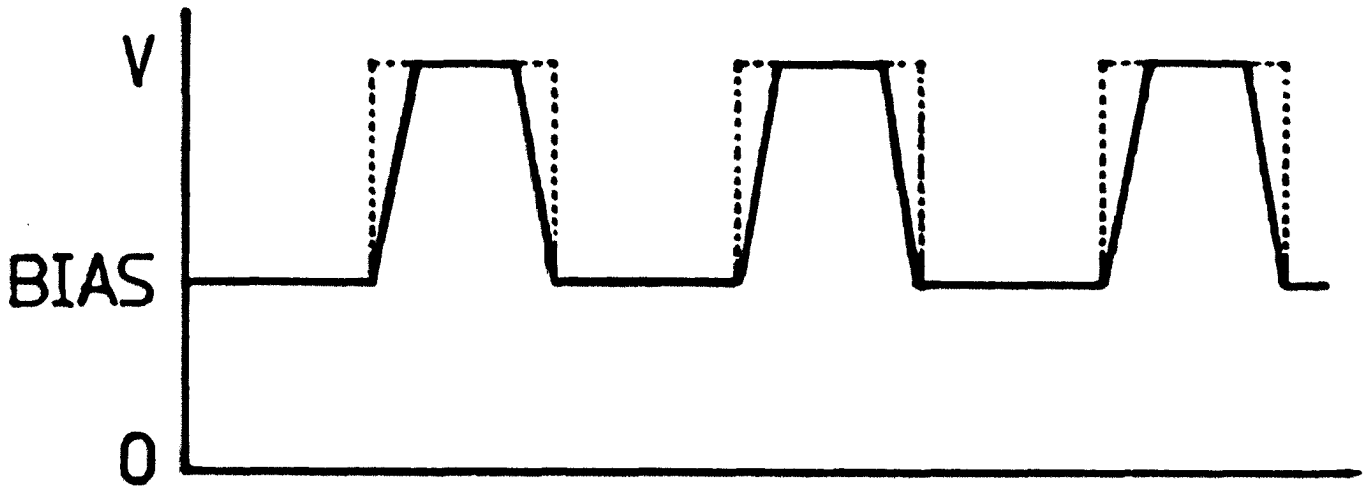

Figure 22. Trapezoidal waveform used in this study; BIAS - DC bias voltage level; V-Ac modulation voltage

f, the modulation voltage Vm, and the sharpness of the edge of the trapezoidal waveform. Higher Vm and a sharper edge generally produce greater degrees of modulation. This effectively puts an upper limit on the modulation frequency f that can be used. Couple this with the need to minimize the 1/f noise contributions to the PAS signal, a compromised value of 100 Hz was subsequently adopted for this study.

A second problem that merits consideration when the modulation frequency is increased from the initial 1 Hz operation to 100 Hz is the fact that no matter how well modulated the laser is at the lower frequency, there is no guarantee that the same condition automatically holds at the higher speed. This is because the mechanical movement of the grating mount, which consists of a pushing action of the PZt device on one-half cycle and a pulling action of a spring on the other, cannot be expected to be identical at both frequencies. The time response of the 100 Hz operation does not allow a similar evaluation used at the 1 Hz case. To make sure there was proper modulation at 100 Hz, a second, identical cell filled with pure nitrogen gas was used as a reference. This second cell is located symmetrically with respect to the focal point of the laser beam on the opposite side of, and behind the first (sample) cell (see Figure 23). The only PAS signal from the second cell originates from the absorption of the windows or the cell body. It is then sufficient to minimize this PAS signal by adjusting the bias and the gain on the high-voltage op amp that controls the PZT pusher.

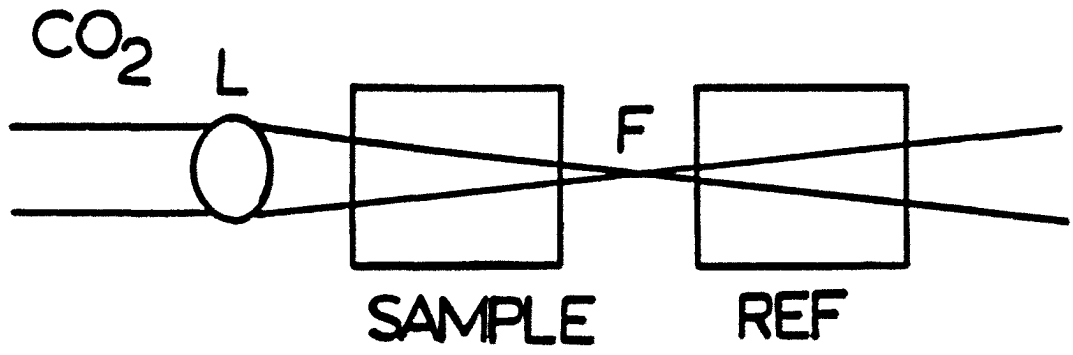

Figure 23. Two-cell configuration; L-focusing lens; F-focal point. The sample and reference cells are symmetrical with respect to F

The magnitude of this residual signal is not expected to be the same as the corresponding one in the sample cell, since the windows are, in all likelihood, not matched. However, the fact that the background in the second cell is minimized is an indication that the power levels in the two half-cycles are matched and that the background in the sample cell is also minimized.

It is entirely possible that the grating is in some average position which allows both laser lines to be active at all times, without alternately switching from one line to the other. The background, as determined by the second cell, will also be minimized, but the system will then be useless for measurements. The only way to test this is to compare the signal obtained in this manner (with absorbing species in the sample cell) with that obtained by using amplitude modulation (chopper) at the same modulation frequency and modulation function. As stated before, ethylene in nitrogen at atmospheric pressure was used as a test case. From Table 4, the absorption coefficients (in $atm^{-1}cm^{-1}$) for the CO_2 P(12), P(14), P(20), and P(22) lines in the 00°1 - 10°) band are respectively, 4.70, 32.2, 1.50, and 1.42. Wavelength modulation between the first pair of lines should provide a PAS signal 85% ($[\sigma_{P(14)}-\sigma_{P(12)}]/\sigma_{P(14)}$) of that using amplitude modulation with a square wave function on the P(14) line and the same modulation between the last pair of lines should yield a negligible signal on the same scale. Measurements were made on samples between 6.00 ppm and 100 ppm ethylene in nitrogen. The PAS response (mV/W) was found to be

roughly a factor of two higher for amplitude modulation. Since choosing the center and the amplitude for wavelength modulation only affects the power and not the actual lasing wavelengths (to within a few megahertz), this can be taken to imply a 59% modulation extent (50%/85%). The fact that the modulation is not 100% can be attributed to the less than ideal range of movement provided by the particular PZT pusher used in this study. The maximum range for this PZT pusher is 40 um, while 113 um is needed to go from line center to line center (see preceding section). The laser is essentially slightly misaligned all the time to allow switching from one line to the next and contains some of each wavelength all the time. Actually, the slight misalignment is necessary to compensate for the differences in the gain curve of the laser lines (see Figure 14). It is also possible to have intervals during each cycle when no lasing occurs. This is confirmed by the observation that the average power is somewhat lower for optimum wavelength modulation. Finally, as a control study to show that the PAS signal observed was not an artifact, wavelength modulation involving the last pair of lines (P(20) and P(22)) on the same samples was performed. As predicted, the signals measured were negligible. This is illustrated in Figure 24 which shows a comparison of signals obtained on the 10 ppm ethylene/N_2 sample with the wavelength modulation of P(12)/P(14), and P(20)/P(22). The incomplete nature of the modulation brings a corresponding decrease in sensitivity, which, as will be seen later, is a reasonable compromise in order to achieve lower detectabilities.

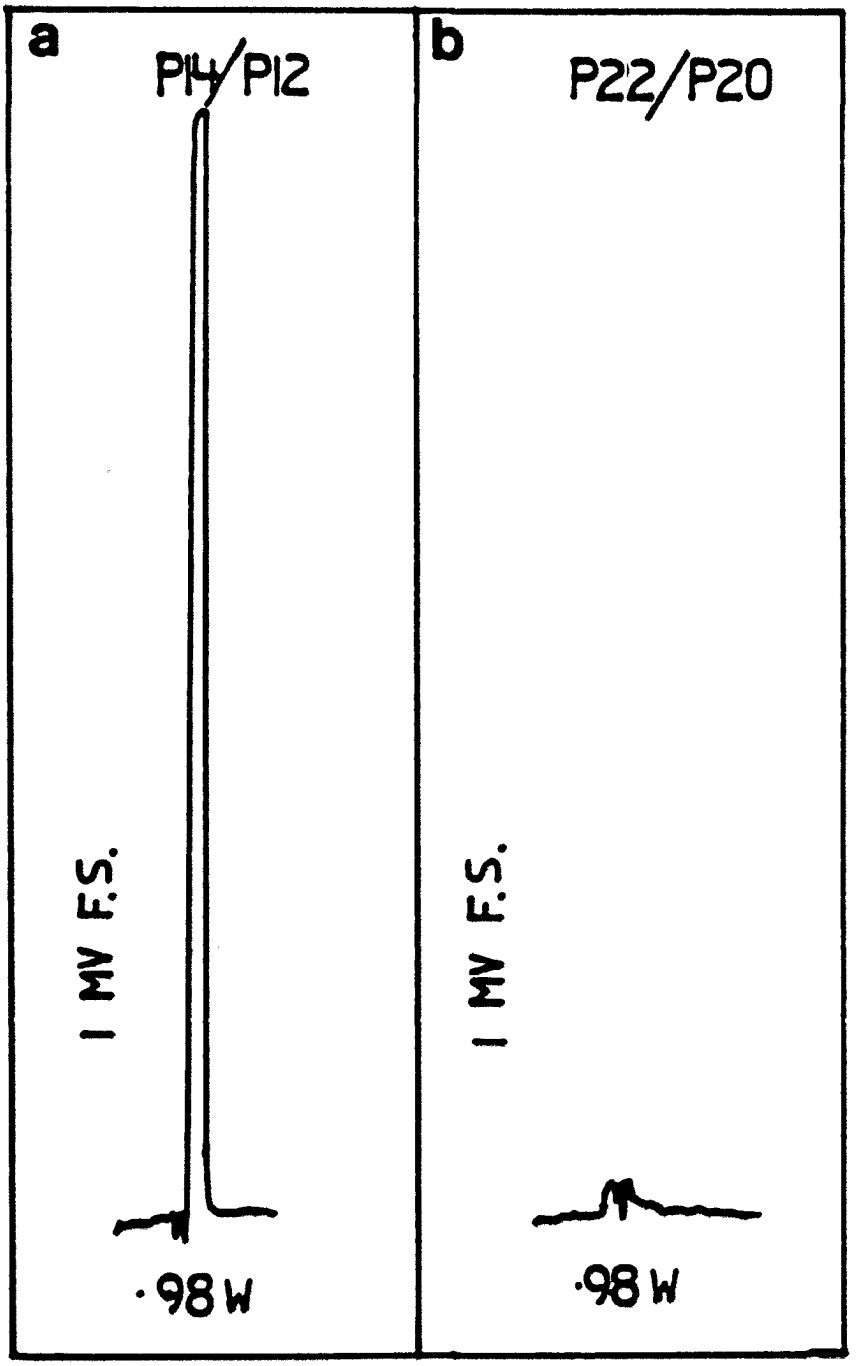

Figure 24. Comparison of wavelength modulation signal a) P(14)/P(12) b) P(22)/P(20). Sample: 10 ppm C_2H_4/N_2

2. Improvement in the detection limit

To see that there is a real advantage using this scheme for PAS measurements, the signal obtained as a function of concentration of ethylene in nitrogen for the cases of amplitude modulation using the P(14) line (Figure 25) and wavelength modulation using the P(12)/P(14) lines (Figure 26) were plotted. In each of the figures, a line with unit slope is drawn to aid in the interpretation. In Figure 25, the contribution of window absorption to the PAS signal was about 470 uV/W, so that measurements below 5 ppm were not possible. In Figure 26, the detection limit is extended by about two orders of magnitude. The residual background signal was due to a small amount of mechanical coupling between the vibrating grating mount and the cell and was of the order of only 1.4 uV. This vibrational coupling is dependent upon the amplitude of the vibration of the grating mount, which in turn depends on the modulation voltage, Vm. Better alignment of the CO_2 laser optics and initial centering can result in the same modulation extent with lower Vm applied to the PZT pusher, hence reducing the residual signal. It can also be eliminated if the PAS cell were set up on a different bench than that of the CO_2 laser. It is important to note that this last value is independent of the intensity of the laser light.

For operation at 1 W of output, the wavelength modulation scheme gives a detectability of 13 ppb (S/N = 3). Naturally, higher laser powers can be used to improve the detectability, since the background

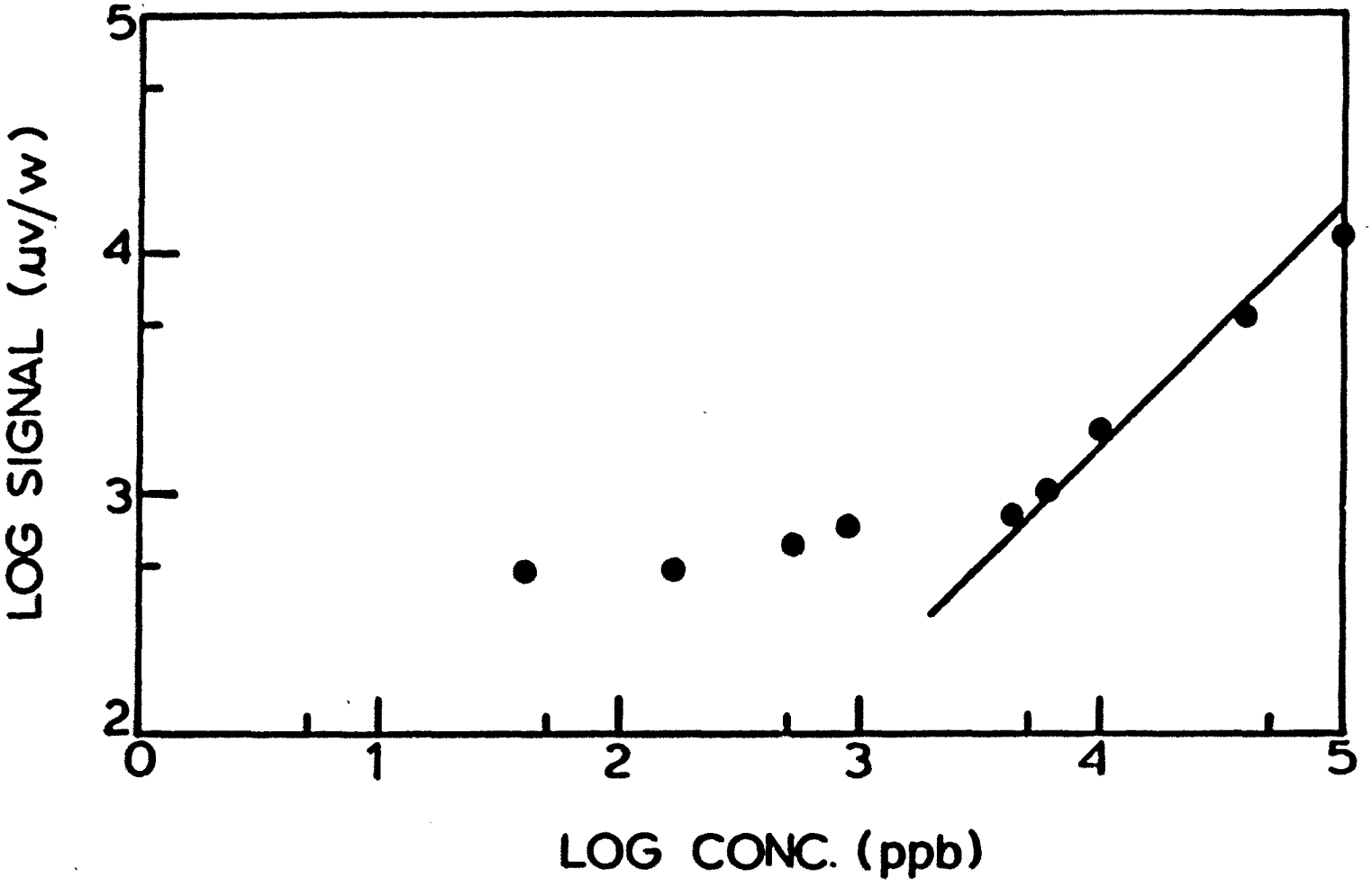

Figure 25. Analytical working curve for amplitude modulation

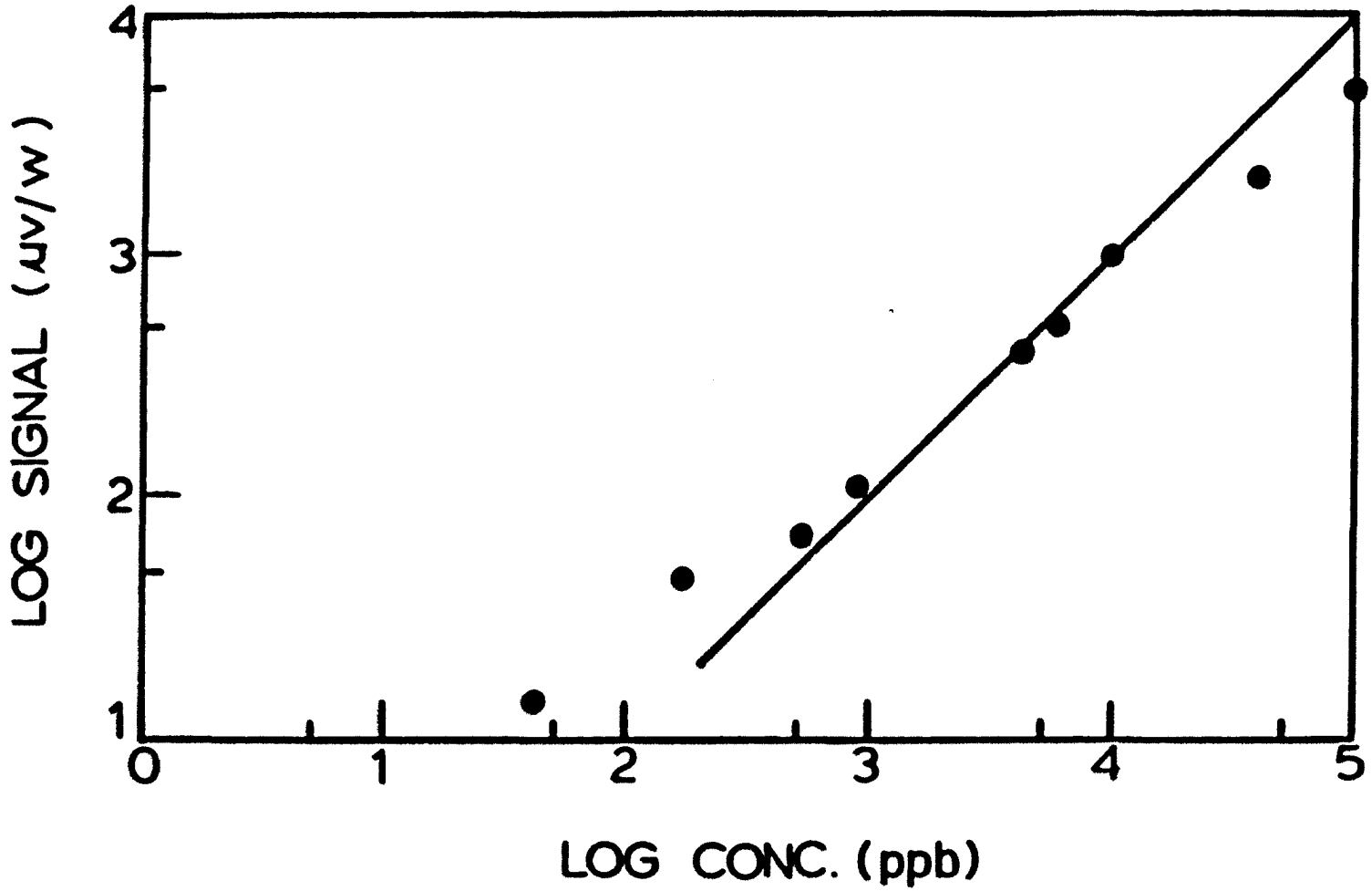

Figure 26. Analytical working curve for wavelength modulation

seems to be intensity independent. There is, of course, a practical limit to this approach. Care must be taken to avoid saturation of the absorption line. The useful range for PAS measurements is thus extended by wavelength modulation. The detectability is comparable to that possible in acoustically resonant cells (191), but without any of the critical requirements in the operation of those cells.

3. Deviations from unit slope

It may be noted that there are deviations in the experimental points from the line of unit slope in each of the last two figures. This can be attributed mainly to the fact that preparing exact mixtures of gases at these low concentrations is extremely difficult, even under carefully controlled conditions. Perhaps the best approach to solve this problem is to employ the use of permeation tubes made of Teflon, or similar chemically inert resins, as gas standards (192). The deviations are more pronounced in Figure 27, the analytical working curve for wavelength modulation. The deviations for the two high-concentration data points (100 ppm and 40 ppm) are negative, while those at the lower concentrations are positive. This is because after the initial measurements for the high-concentration samples, the CO_2 laser was "walked", a procedure which involved a series of adjusting and readjusting the laser optics to yield the rated power and good mode structure which results in more evenly distributed power and better retention of spatial characteristics in each of the two half-cycles of

modulation. Subsequent measurements for the low-concentration samples yielded stronger signals because of the better modulation. This is further confirmed by the fact that the background signals obtained in the second reference cell for these samples were consistently lower than their counterparts in the high-concentration trials.

D. Conclusion

By using a piezoelectric pusher, a commercial CO_2 laser was adapted to operate in the wavelength-modulated mode for photoacoustic measurements with good discrimination against background due to window absorption. The detection limit was extended by approximately 2 orders of magnitude. The minimum detectable concentration for ethylene in nitrogen was calculated to be 13 ppb. This last value can be further reduced if i) better acoustical and vibrational isolation for the PAS cell from the surroundings is provided, ii) higher laser power is used, and iii) a larger modulation depth can be established. The last condition can be easily satisfied by modifying the mechanical design of the grating mount. Recalling from Figure 16, the horizontal movement (X) for the angular displacement ($\Delta\theta$) of 8.4×10^{-4} rad. for line-center-to-line-center switching is 113 um on a 13.5 cm center (Y). Now X can be made closer to the maximum range of the PZT pusher (40 um) by reducing the length of Y for the same $\Delta\theta$. To reduce Y by a factor of, for example, 3, would bring X to about 38 um, well within the striking distance of the ability of the PZT pusher.

The concept of wavelength modulation is not necessarily limited to point sampling operations. Long-path absorption measurements can also benefit from this design to help discriminate against interferences such as scattering of aerosol particles and atmospheric turbulence.

IV. TRACE DETECTION IN GASES BY FABRY-PEROT INTERFEROMETRY

A. Introduction

The sensitivity of absorption measurements made on a gaseous sample whose excited-state decay is predominantly nonradiative, can often be improved over a conventional transmission method by monitoring some effects associated with the thermal relaxation following the absorption of radiation. The most convenient of these effects is the generation of heat, creating temperature changes in the sample. This calorimetric approach to determining small absorbances forms a class of techniques, which are particularly well-suited to the infrared spectral region due to the predominance of nonradiative relaxation of vibrationally excited molecules. Moreover, since the magnitudes of all these associated effects increase with the power of the excitation light source, one can, therefore, in principle achieve lower detectabilities compared to conventional measurements.

Depending on the method of detecting the temperature change in the sample, these techniques can be classified into the following categories: i) photoacoustic detection, ii) thermal lens calorimetry, iii) photothermal deflection detection, and iv) interferometry. Much has been discussed on the photoacoustic effect in the preceding chapters. Detailed discussion will be bypassed here.

The thermal lens effect, first reported by Gordon et al. (193), is caused by the nonuniform heating of the sample by a laser beam. An absorbance measurement using this effect is obtained by placing

the sample in a TEM_{00} laser beam at one confocal distance past the beam waist for maximum sensitivity (194). As the laser beam is unblocked, the intensity at the beam center in the far field decreases to a steady-state value resulting from the additional divergence of the beam by a thermally induced lens-like element in the sample. The thermal lens is a gradient in the refractive index which follows the temperature distribution formed by the conversion into heat of energy absorbed from the Gaussian intensity profile of the beam. The absorbance of the sample can then be determined from the relative change in the intensity at the center of the beam. Most of the measurements based on the thermal lens effect have been accomplished with condensed phase samples (liquid) (194-198). There are, however, several applications to gas-phase infrared absorption measurements in the study of vibrational energy transfer (199-201).

The photo-thermal deflection technique is based on the so-called "mirage effect", i.e., when an absorbing medium is irradiated with intensity-modulated radiation, its surface will exhibit periodic temperature fluctuations which will in turn induce a modulated refractive index gradient in a layer of gas (of thickness on the order of the thermal diffusion length) adjacent to the sample surface. This time-dependent gradient is then employed to periodically deflect a probe beam propogating parallel to and near the sample surface. The deflection amplitude can be related to the strength of the absorption in a straightforward manner. Originally developed as a technique for

condensed phase samples (202,203), photo-thermal deflection has also found application in the monitoring of gaseous molecules. Fournier et al. (204) reported a photothermal deflection scheme for the detection of trace gases and for measuring weak absorption in gas-phase samples. Using a CO_2 laser as the pump beam and a HeNe laser as the probe beam, a detection limit of 5 ppb of ethylene in nitrogen (S/N=1) has been reported. Typical experimental set-ups for thermal lens calorimetry and photothermal deflection spectroscopy are shown in Figure 27.

Perhaps the most sensitive way to monitor changes in the refractive index caused by temperature variations is through interferometry. Optical interference is the basis of interferometry and can be defined as the modification of the intensity of radiation waves by combining, or superimposing two or more waves. The resultant intensity is sometimes decreased, resulting in destructive interference, and sometimes increased, resulting in constructive interference. If monochromatic radiation is used, then for maximum constructive interference the total path difference between the superimposing waves should be an exact multiple of the wavelength. The phenomena of constructive and destructive interferences are manifested as alternating bright and dark fringes. If the optical path travelled by the waves is altered, either physically or by a change of the refractive index as a result of a temperature rise in the medium, the fringes will shift from their

Figure 27. Schematic representations of some thermooptic-based methods. a) Experimental set-up for photothermal deflection detection. SM-spherical mirror; M_1, M_2 - steering mirrors; PD-position detector; LIA - lock-in amplifier (204). b) Optical system for detecting the thermal lens effect A sample cell is placed a distance Z_1, from the beam waist 0. Z_2 indicates the distance between the cell and a pinhole, which samples the intensity at the beam center I_{bc}. The spot size of the beam at the waist, sample cell, the pinhole are W_0, W_1, W_2, respectively (194)

a)

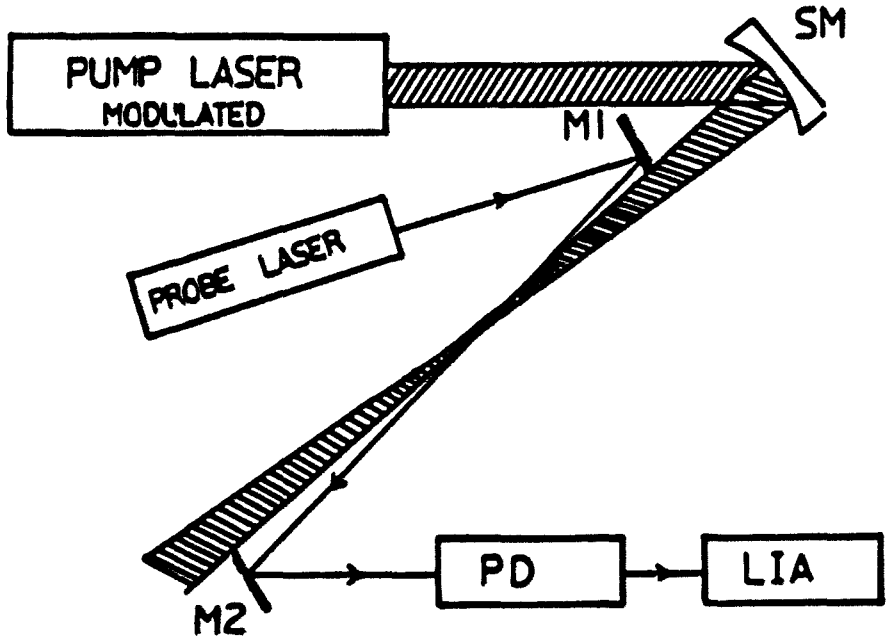
PUMP LASER
MODULATED
SM
M1
PROBE LASER
PD
LIA
M2

b)

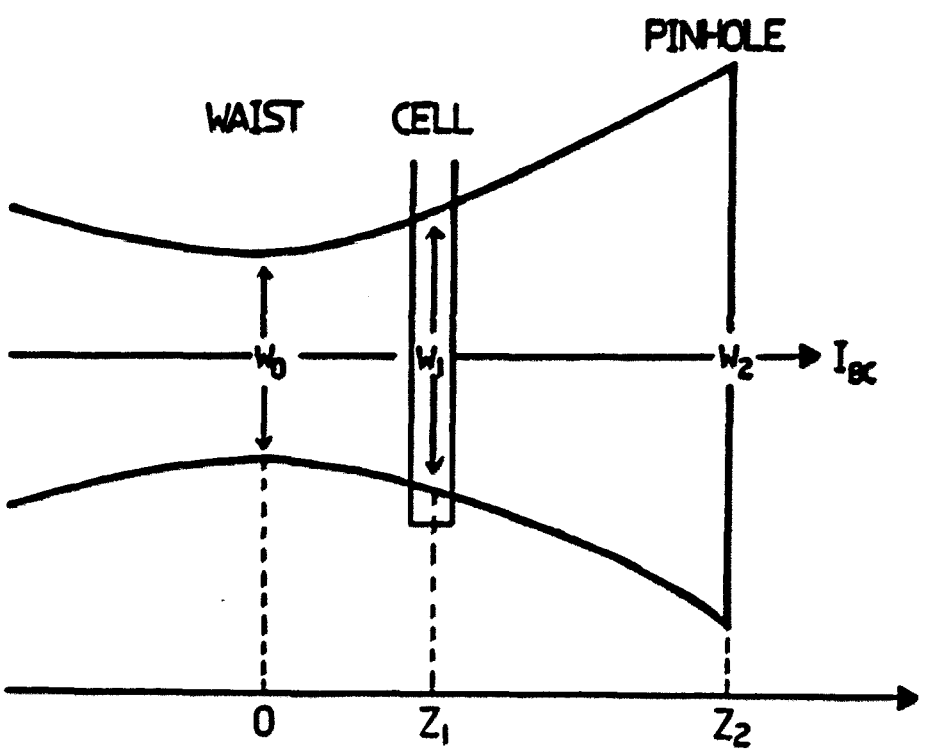
PINHOLE
WAIST
CELL
W_0
W_1
W_2
I_{BC}
0
Z_1
Z_2

original positions. And, as in the other thermo-optical techniques discussed so far, the shift amplitude can be related to the strength of absorption of whatever species present in the medium.

Interferometers have long been powerful tools for spectroscopic techniques that require high spectral resolution. For example, the study of hyperfine splittings has been achieved by using interferometers (205-207). Another frequent application is in the area of establishing high-frequency stability in lasers (208,209) for high resolution spectroscopic measurements. Finally, determination of laser wavelengths to great precision and accuracy has also been accomplished with the aid of interferometry (210,211). The same technology that makes these applications possible can easily be transferred to measure small changes in refractive index. In subsequent sections of this chapter, one particular interferometer, the Fabry-Perot, will be discussed in detail in terms of its unique features. A study of its application to detecting trace gases in conjunction with wavelength modulation previously described will also be presented.

B. Interferometry

Although interferometers have been used for over 100 years to compare the refractive indices of gases, the use of an interferometer to detect weak absorptions was only recently demonstrated by Stone (212). In his experiment, he used a dual-beam interferometer to monitor the change in optical path length due to heating of the sample solution. Since then, the use of an interferometer as an integral part of an

absorption measurement detector has been expanded, and is not limited to condensed phase samples alone. Instruments based on optical interference can take many forms and designs. Among the more common ones are: i) the Michelson interferometer, ii) the Mach-Zender interferometer, iii) the Jamin interferometer, and iv) the Fabry-Perot interferometer. The designs of the first three types of interferometers are schematically represented in Figure 28.

The Michelson interferometer is perhaps the oldest design. Originally designed by Michelson (213,214), its working principle is still being used as the basis for other types of interferometers. The general theory of interferometry, therefore, is most readily comprehended by first acquiring an understanding of the way in which a basic Michelson interferometer works.

The Michelson interferometer is a device that can split a beam of radiation into two paths and then recombine them so that the intensity variations of the exit beam can be measured by a detector as a function of path difference. The simplest form of the interferometer is shown in Figure 28a. It consists of two mutually prependicular plane mirrors, one of which can move along the axis shown. The movable mirror is either moved at a constant velocity, or is held at equidistant points for fixed time periods between these points. Between the fixed mirror and the movable mirror is a beamsplitter, where a beam of radiation from an external source can be partially reflected to the fixed mirror and partially transmitted to the movable mirror. After each beam has

Figure 28. Schematic representations of several types of interferometers. A) Michelson interferometer B) Mach-Zender interferometer, BS-beam splitter; M-plane mirror C) Jamin interferometer. G1, G2 - gas chambers; C1, C2 - compensators; M1, M2 - equally thick plane parallel glass plates of the same refractive index, opaquely silvered on one surface

A)

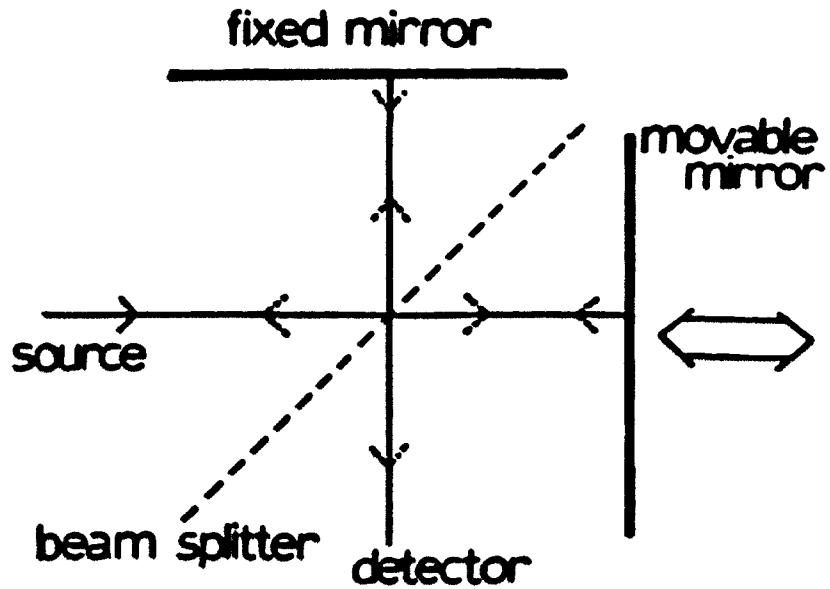
fixed mirror
movable mirror
source
beam splitter
detector

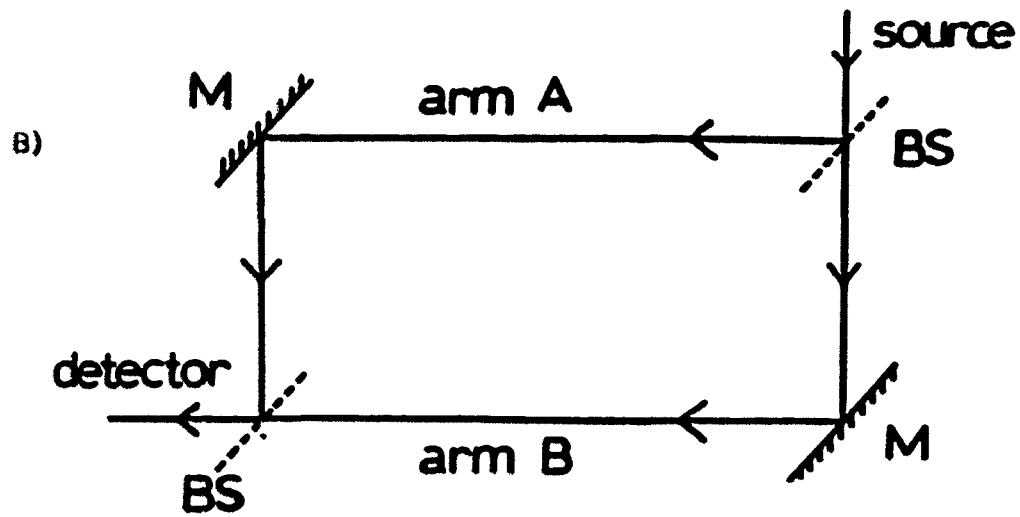

Figure 28. (Continued)

c)

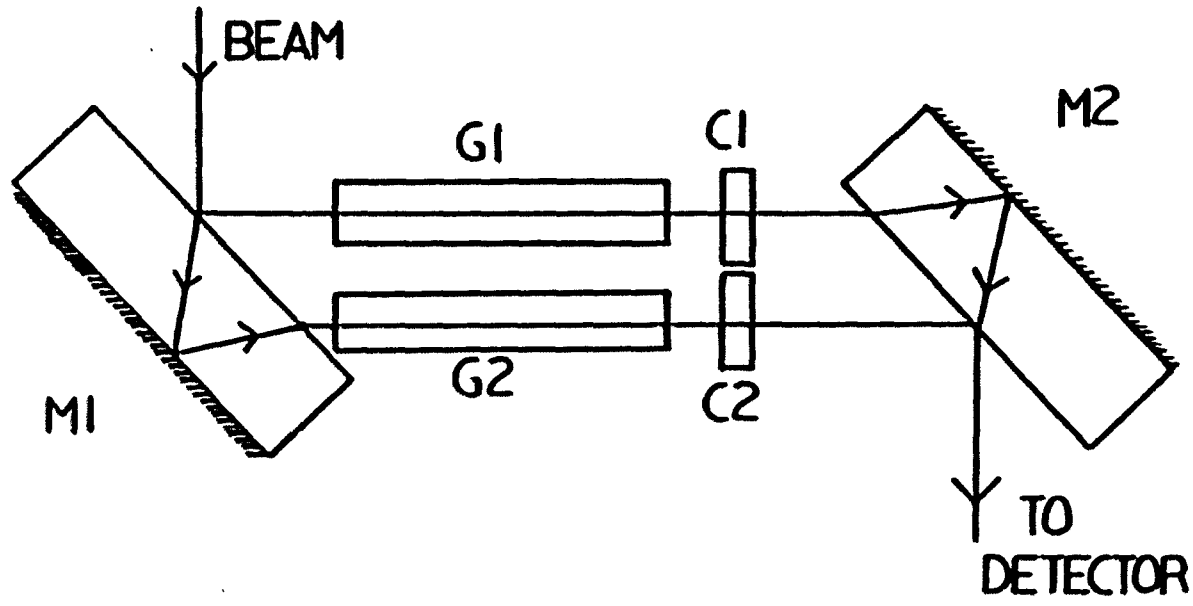

Figure 28. (Continued)

been reflected back to the beamsplitter, they are again partially reflected and partially transmitted. Thus, a portion of the beams which have travelled in the path to both the fixed and movable mirrors reach the detector. Now consider the case of a source of monochromatic radiation producing an infinitely narrow, perfectly collimated beam. Let the wavelength of the radiation be λ cm. When the fixed and movable mirrors are equidistant from the beam splitter, the two beams have travelled equal pathlengths and are perfectly in phase upon recombination. At this point, the signal at the detector is a maximum because the beams are interfering constructively (Figure 29a). However, if the movable mirror is displaced a distance of $\lambda/4$ cm, the optical path difference between the two beams is $\lambda/2$, the components are completely out of phase and destructive interference occurs. Now the signal at the detector is a minimum. As the movable mirror moves another increment $\lambda/4$, the beams are once again in phase (Figure 29c) and the signal at the detector again reaches a maximum. Therefore, as the movable mirror is uniformly moved, the signal at the detector goes through a series of maxima and minima in a cosine fashion directly proportional to the velocity of the moving mirror.

The basic Michelson interferometer has been successfully applied to infrared scanning spectrometry - Fourier transform infrared spectrometry (FTIR) (215) - where, instead of a monochromatic beam, a polychromatic source in the infrared region is used. It can also be

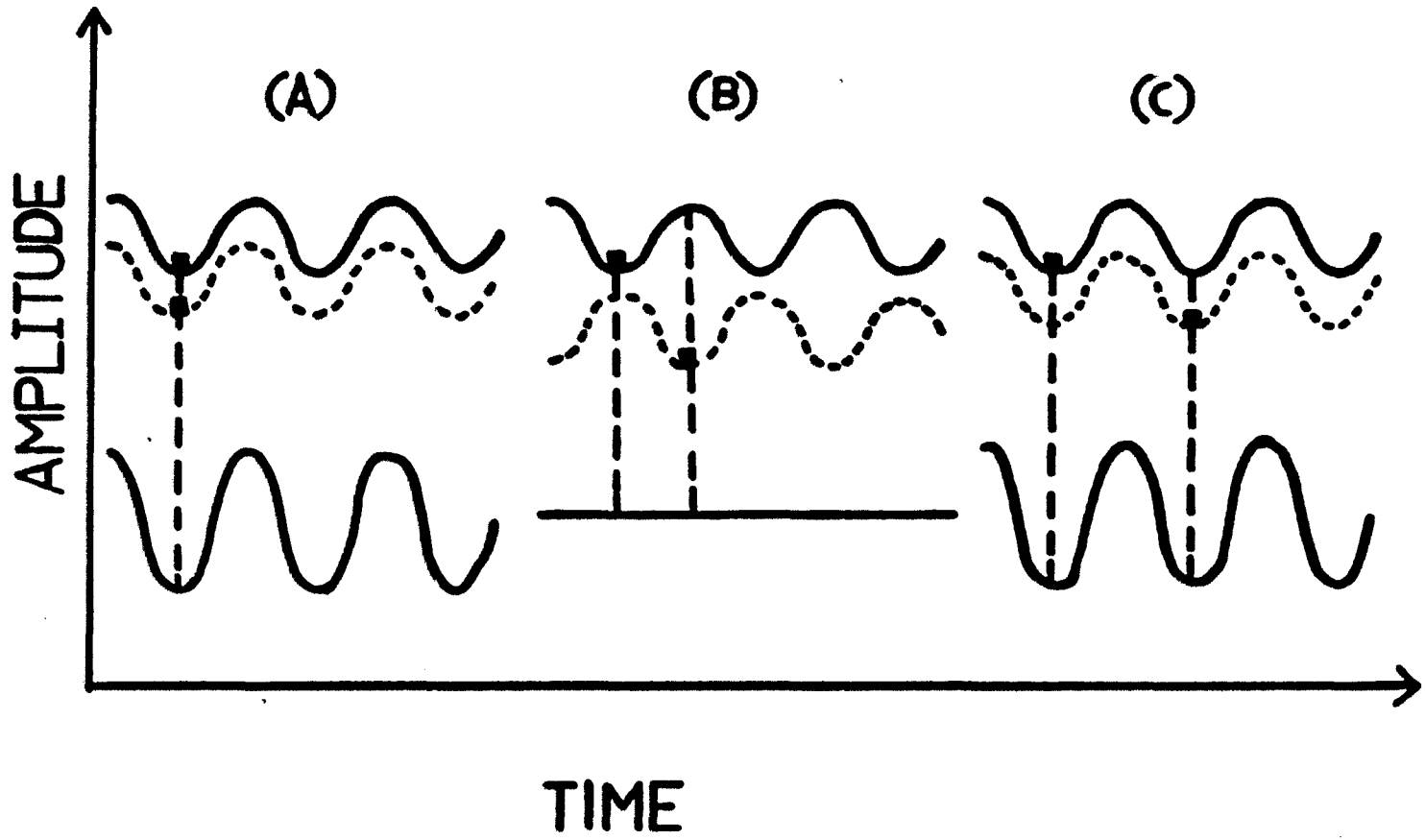

Figure 29. Superposition of waves in a Michelson interferometer. A) Constructive interference when path difference is zero. B) Destructive interference when path difference is $\lambda/2$. C) Constructive interference when path difference is λ

readily modified to operate in a dual-beam fashion as in the Fourier transform spectroscopic study of very far-infrared atmospheric absorptions (216), and in the determination of laser wavelengths with an accuracy of several parts in 10^9 (210).

Optical pathlength differences can also be created by changing the refractive index (RI) of the medium in which the beams travel. The resultant shift in interference fringes constitutes the basis for monitoring the refractive index change. Such a concept has been successfully adopted in a commercial detector for high performance liquid chromatography (HPLC), which typically uses a Michelson interferometer, or some variation thereof to monitor RI changes due to change in the composition of the liquid element passing through the detector.

The refractive index change, as suggested earlier, can also be thermally induced, in which case the interferometer will function as an absorption detector. An example to illustrate this thermooptic-based method is the work by Cremers and Keller (217). By using a Jamin interferometer and a single frequency laser, small changes in the optical pathlength ($\sim\lambda/200$) due to heating of weakly absorbing liquids was measured and solute absorptions (CCl_4) of $\sim 5 \times 10^{-6} cm^{-1}$ was reported.

Another interferometer that has been used as an absorption detector is the Mach-Zender design. Using this interferometer, the small phase change of a single frequency laser (probe beam) due to absorption and

the subsequent heating was monitored for trace gas detection (119). This type of phase-fluctuation optical heterodyne technique has also been combined with Stark-effect modulation to measure NH_3 in air with a reported detection limit of 5 ppb (121). It has also been adapted into a GC detector with reasonable sensitivity ($\sim 10^{-8} cm^{-1}$) (218).

It is important to note that the optical interference fringe pattern of the aforementioned interferometres takes the form of a cosine wave. Since interferometric detection of thermally induced refractive index or phase changes can best be described as fringe shift experiments, it is evident that detectability depends on the quality of the interference fringe that can be achieved. The key measure of this quality is the finesse of the individual interferometric systems. As will be seen later, the Fabry-Perot interferometer is far superior to the others in this particular aspect which in turn lends itself well to being a sensitive absorption detector for trace gases.

C. Fabry-Perot Interferometer

A Fabry-Perot (FP) interferometer is constructed with two partially transmitting mirrors that are parallel to each other. This is said to be the FP cavity. In an air spaced FP cavity, the two mirrors are coated on their inside surfaces with partially transmitting coatings of high reflectivity and antireflection coatings on the outside surfaces. Normally, the outside surface is slightly wedged (10 to 30 min.) with respect to the inside surface to avoid forming additional cavities (see

Figure 30a). If the transmitted beams are superposed, then maximum constructive interference occurs whenever

$$\lambda/n = 2d/m \qquad (4.1)$$

where λ is the wavelength of light, n is the refractive index of the medium, m is any integer, and d is the spacing of the mirrors. Equation (4.1) assumes normal incidence of the beam with respect to the mirrors. If one of the mirrors is made to travel a short distance repetitively while maintaining its parallelism, the interferometer is said to be operating in a scanning mode. Scanning is usually achieved by means of supplying a linear voltage ramp to a piezoelectrical element mounted to the movable mirror. The resultant interference fringe pattern as observed by a photodetector is schematically represented in Figure 30b. Typically, the FP interferometer is used in air for accurate wavelength determinations. If, however, a single-frequency laser is used, the RI of whatever medium inside the cavity can be monitored. From equation (4.1), it can be seen that $\Delta\lambda/\lambda = \Delta n/n$. Since FP interferometry has been used to determine laser frequencies to 3 parts in 10^{11} (211), one can expect a similar detectability in the change in RI in the ideal case.

1. Finesse

The sensitivity of any interferometer to detect small shifts in fringes (hence change in RI) is directly related to the sharpness of the fringes. This quality is conveniently measured by the half-width

FABRY PEROT INTERFEROMETRY

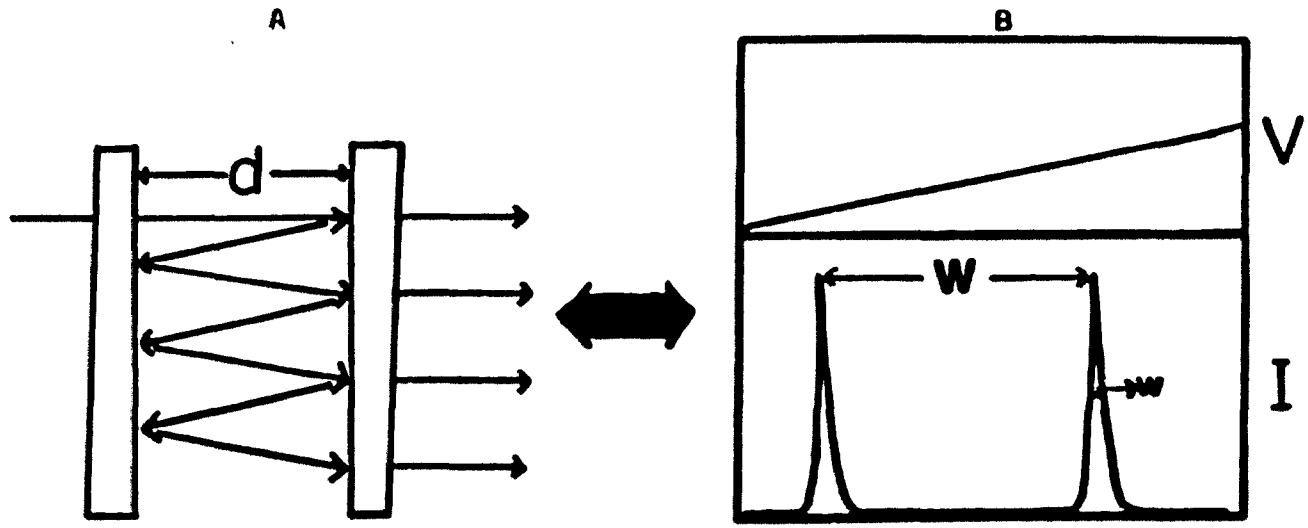

Figure 30. The Fabry-Perot interferometer. A) Multiple reflections within the Fabry-Perot cavity. The actual reflections are not separated in space, as shown, but move back and forth upon themselves, in a manner which cannot be drawn clearly. B) Upper: linear voltage ramp supplied to the scanning mirror. Lower: resultant interference fringe pattern, Finesse = W/w

of the fringes and is best expressed by the ratio of the separation of adjacent fringes and the half-width. Such a ratio is called the finesse (F) of the fringes. In the previously described interferometers (Michelson, Mach-Zender, etc), the inherent limit on finesse is 2 because of the cosine waveform of the interference fringe pattern. The finesse of a FP interferometer, on the other hand, can be as high as the individual optical components allow. In the most ideal case, the finesse of a FP system is governed by the reflectivity of the mirrors that form the FP cavity and is given by (219)

$$F = \pi\sqrt{R}/(1-R) \qquad (4.2)$$

where R is the reflectivity of each of the mirrors. Since this determines the resolution of the instrument, one wants as high a value as possible. To appreciate the relationship between the sharpness of the fringe and the reflectivity of the mirrors, a plot of the intensity contours of fringes as a function of reflectivity is presented in Figure 31.

From the foregoing, it is evident that as the reflectivity of the mirrors, and hence F (see Figure 32), is increased, the intensity distributions become more favorable for the measurement of fringe positions. In practice, however, the finesse is often less than the value given by equation (4.2). This is because equation (4.2) is derived under the assumption that the reflecting surfaces are perfectly plane and parallel. This is not the case as surfaces can never be

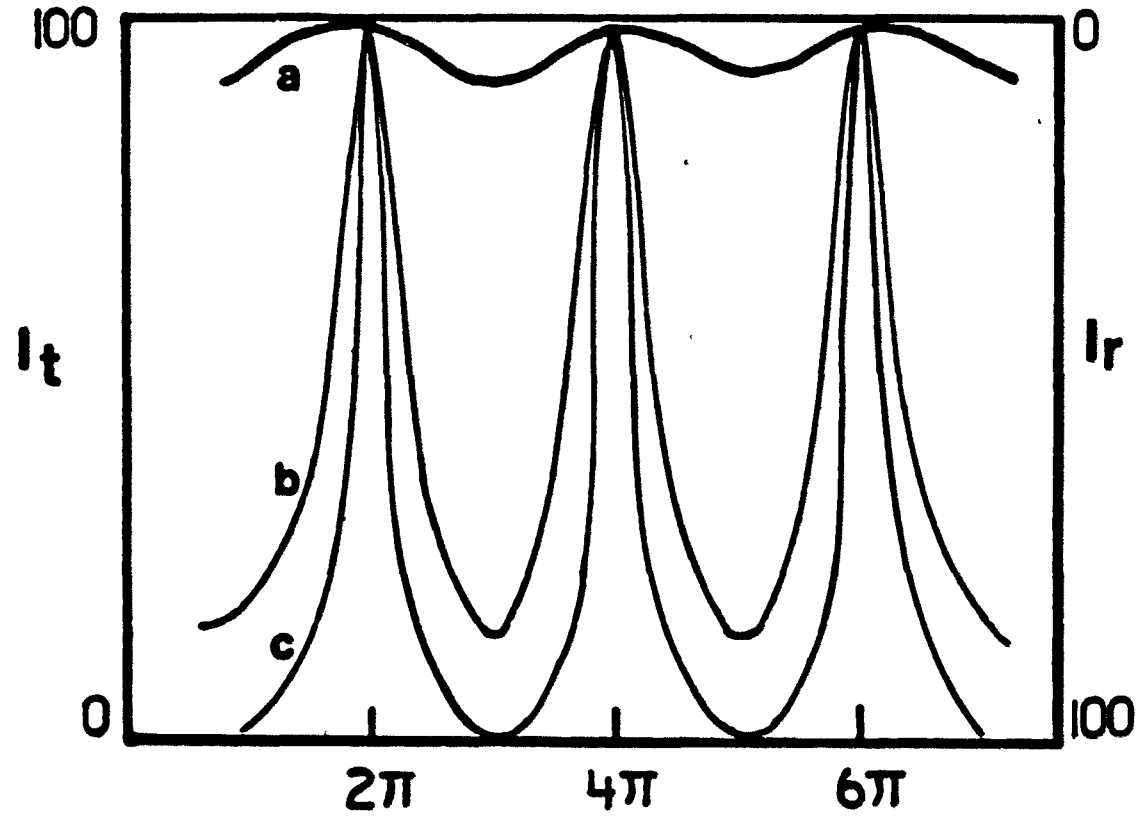

Figure 31. Intensity contours of fringes due to multiple reflections as a function of reflectivity. a) reflectivity = 4% b) reflectivity = 50% c) reflectivity 80%. I_t - percent intensity transmitted; I_r - percent intensity reflected (220)

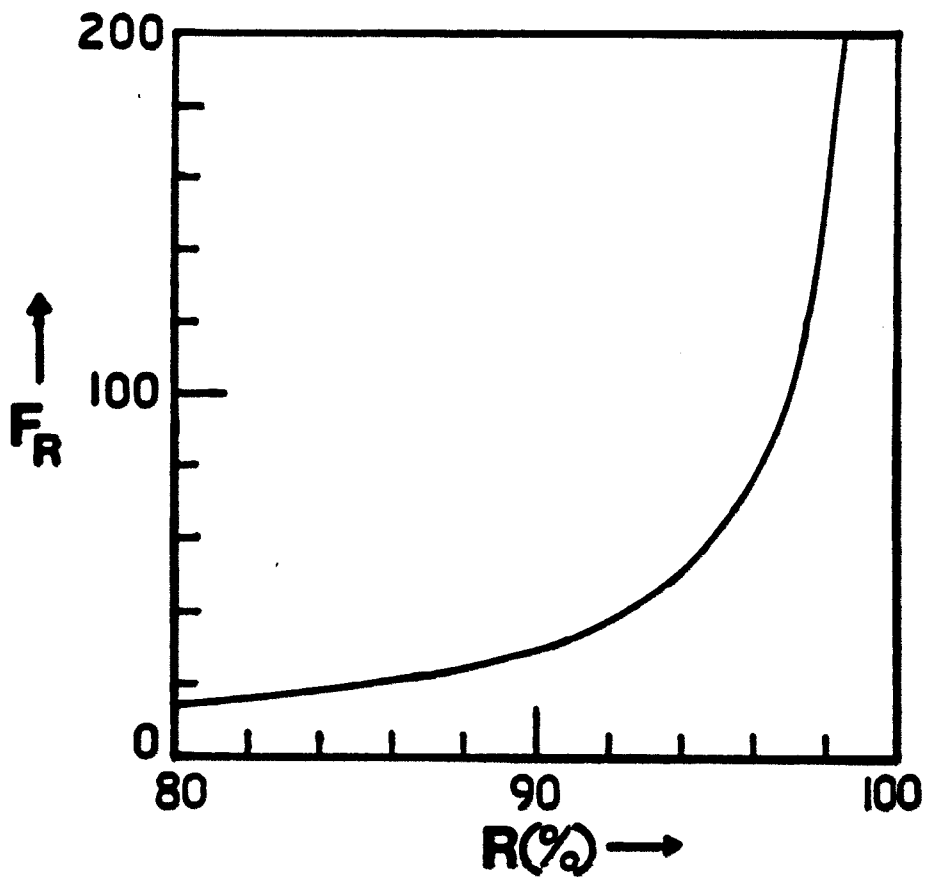

Figure 32. Reflectivity finesse vs. reflectivity (220)

worked perfectly plane, and in consequence, the mirror separation d always varies over the beam diameter. Therefore, as R approaches unity, the finesse approaches a limit which depends on the defects in the mirror surfaces, i.e. with given mirror surfaces there is an upper limit to the fringe sharpness which cannot be exceeded whatever the reflectivity of the coatings. The value of finesse due to the flatness, F_f can be calculated by

$$F_f = M/2 \text{ for a } \lambda/M \text{ surface} \qquad (4.3)$$

where M is the fractional wavelength deviation from planeness across the mirror aperture, and λ is normally specified at 550 nm.

There is yet another factor that can reduce the finesse of a FP system; the diffraction losses arising from the finite aperture of the interferometer. The net finesse of the entire system is found by treating the component finesses as if they were parallel impedances:

$$F_{net}^{-2} = \sum_i F_i^{-2} \qquad (4.4)$$

2. Throughput or transmission

The throughput (t) of a FP interferometer is defined as the transmission of a FP at resonance. One advantage of a FP is that it is an extremely efficient instrument. For infinitely flat reflecting surfaces, t depends primarily on the losses in the mirror and the coatings and is given as (219)

$$t = (1-\frac{A}{1-R})^2 \qquad (4.5)$$

where A is the losses due to scatter and absorption and is typically .2%/surface for modern coatings. At high values of R, which are of practical interest, an increase of R is accompanied by an increase of A/(1-R), and from equations (4.5) and (4.2), t decreases with increasing F. Thus, high values of both peak transmission (throughput) and finesse are incompatible requirements, and in practice some compromise must be made between them. Fortunately, with modern multilayer dielectric coatings, t can be substantial even with reflectivities of 98 to 99% (see Figure 33). It is important to note that the above definition of transmission assumes perfectly flat plates. If the plates have a surface error (of the type according to equation (4.3)), as they always do to some extent, the peak transmission will normally be reduced.

3. Detectability of FP interferometry

We can estimate the detectability allowed by a combination of commercially available components. Single-frequency HeNe lasers (λ = 633 nm) have a stability of about 1 MHz (1s), or about 2 parts in 10^9 ($633 \times 10^{-10}/30$). Interferometers readily provide d = 15 cm. The free spectral range (FSR) which, in the case of a FP illuminated by monochromatic light, can be defined as the separation between adjacent fringes, and is given by

$$FSR = c/2nd \qquad (4.6)$$

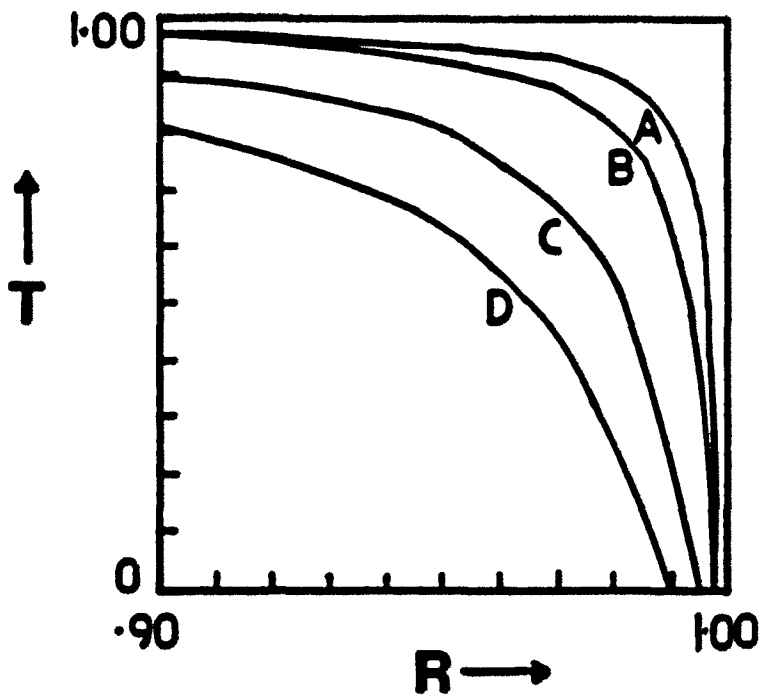

Figure 33. Throughput vs. reflectivity as a function of absorption (A) 0.1% absorption (B) 0.2% absorption (C) 0.5% absorption (D) 1.0% absorption (220)

where c is the speed of light (3×10^{10} cm sec^{-1}), and n is the refractive index of air (~1). This gives a FSR value of about 1 GHz. The half-width of the interference fringe is thus 10 MHz for a system finesse of 100. The peak of the interference fringe, however, can be located to better than one-tenth the width, so that the ultimate resolution is also 1 MHz. One can therefore expect excellent detectability (laser stability limited) from a FP interferometer in monitoring small changes in RI. Indeed, this concept is borne out by the improved detectability of a RI detector for HPLC based on FP interferometry developed by Woodruff and Yeung (221).

4. FP as an absorption detector

To function as an indirect absorption detector, a collimated, secondary light source matching the absorption band of the species of interest can be introduced along the optical path of the interferometer to thermally induce a RI change. One can explicitly relate the RI change, Δn, and the absorbance of the sample, A. For small absorptions, which is typically true in trace gas detection, the amount of light energy absorbed is 2.303 AE, where E is the source energy in joules. If the light pulse and the relaxation time are much shorter than the thermal conduction time, T_c across the interaction region of cross-sectional area a cm^2, the temperature increase ΔT per unit length of path is

$$\Delta T = \frac{2.303\ AE}{C_p Da} (^{\circ}K) \qquad (4.7)$$

where C_p is the specific heat in $Jg^{-1}K^{-1}$ and D is the density of the medium in g cm^{-3}. We then have

$$\Delta n = \Delta T(dn/dT) \qquad (4.8)$$

where dn/dT is the temperature dependence of the RI. In air, the actual RI change which results when molecules in a sample absorb energy and suffer V—>R, T relaxation follows from the Clausius-Mossotti equation, and is given by (121)

$$\Delta n = -(n-1)\frac{\Delta T}{T_{abs}} \qquad (4.9)$$

where T_{abs} is the absolute temperature of the gas, n is the equilibrium value of the RI. For very dilute gas samples in air (n-1) equals 2.92×10^{-4}. For $T_{abs} = 293$ k, $-(n-1)/T_{abs}$ is approximately -1.0×10^{-6} k^{-1}.

Using typical values: E = 1 J, Cp = 1.006 $Jg^{-1}k^{-1}$, D = 1.165×10^{-3} g cm^{-3}, a = 0.01 cm^2 and $dn/dt = -1.0 \times 10^{-6}$, one finds the minimum detectable absorbance is 1.0×10^{-8} for a RI detectability of 2×10^{-9}. For a gas sample of ethylene in 1 atm of nitrogen, excited by the P(14) CO_2 laser line ($\alpha = 32.2$ $cm^{-1}atm^{-1}$) (188). This translates to a detectable concentration of about 0.3 ppb. A subtle point here is that traditional absorption measurements gain linearly with increasing interaction length. In interferometry, increased length increases the absorbed energy, but at the same time more volume must be heated up.

Therefore, there is no net gain. However, the resolution of the interferometer generally increases with the distance d, so that longer light paths are still desirable.

5. Noise considerations

The above calculation is based upon the ultimate resolution of the FP interferometer (2×10^{-9} or 1 MHz) which is also the stability of the single frequency helium neon laser. Implicit in this calculation is the notion that the sensitivity of this scheme is ultimately limited by the stability of the probe beam. In practice, this limit is not achieved because at low concentration levels, many sources of noise become important. Mechanical vibration of the laboratory can be directly coupled to the interferometer, causing jitter in the fringe peak position. Acoustic noise in the room affects primarily the part of the interferometer cavity not covered by the interaction region. Ambient pressure changes in the laboratory can also lead to drifting of the fringes. Thermal expansion of the interferometer mounts and other optical components can also contribute to background noise. Most commercially available FP interferometers are constructed of materials with low coefficients of thermal expansion, such as super-invar ($\leq 0.36 \times 10^{-6}\ k^{-1}$). So, the problem of thermal drift can be somewhat alleviated. But the most serious disturbance caused by temperature changes is the open FP cavity. The best solution is to use a thermostat-controlled enclosure. Some improvement can also be expected through proper vibrational and acoustical isolation.

Most of the above-mentioned contributions from noise can be compensated for in a dual-beam arrangement. Two parallel optical paths can be introduced into the interferometer by splitting the output of the single-frequency laser, one for the sample interaction chamber which contains the species of interest, the other for a reference chamber containing the buffer gas only. The difference in the positions of the fringes in the two paths, as opposed to the absolute positions in the single-beam arrangement, can then be registered using separate photoelectric detectors. If the two chambers are made to match as much as possible, thermal effects are minimized. In fact, drifts in the interferometer and in the laser, vibrations, and acoustic noise are automatically compensated for. There is also an added advantage in that residual background absorption by water vapor, gaseous interferents, etc., which ultimately limit the detection of trace gases when the system is operated in situ, can be accounted for, assuming, of course, both the reference and sample chambers are irradiated with the excitation beam.

A dual-beam arrangement for Fabry-Perot interferometry adapted into a refractive index detector for HPLC was developed in our laboratory (222). The actual flow cells were machined out of the same aluminum cylinder. A single-frequency HeNe laser was split into parallel beams and directed through the flow cells located inside the FP cavity. After the exit from the cavity, the two light beams were directed to two separate photomulitplier tubes for individual monitoring of fringe shifts. With the reference cell operating in a static mode, and the

sample cell in a flowing mode, the net difference between the fringe shifts of the two beams was monitored by a minicomputer which also generated a linear ramp to scan the interferometer through the piezo-electric element attached to the movable mirror. Using known concentrations of benzene in acetonitrile, a detectability of 4×10^{-9} RI units (S/N = 3) was reported. The ultimate detectability of this optical scheme is limited by the residual differences in the two optical paths, resulting from limitations in machining the flow cells to identical physical lengths, d. However, it is evident that the quantity of interest here is not the absolute value of the refractive indices, but Δn, the change in RI when the chromatographic effluent passes through the detector and that $\Delta n/n = -\Delta d/d$, where Δd is the shift in the position for constructive interference. Any fractional mismatch in the physical lengths of the two optical paths will translate only into a fractional error in the amount of correction applied to Δn as dictated by the reference beam. For example, a mismatch of the order of 0.2 mm over a 10 cm path will result in the reduction of certain types of noise (discussed above) to the order of 0.002 compared to the single-beam case. Therefore, there is still overall improvement in noise compensation in this optical scheme.

In the next two sections, an experiment based on dual-beam Fabry-Perot interferometry for trace gas detection will be described. Along with this discussion, the failure of this scheme to reach its potential as an absorption detector because of instrumental limitations will also be presented.

D. Experiment Based on Dual-Beam Fabry-Perot Interferometry for Gas Detection

1. Experimental section

The experimental arrangement is shown in Figure 34. The individual components are summarized in Table 6. A single frequency HeNe laser (Tropel, Fairport, NY, Model 100) is split into two parallel beams by a 2.5 cm diameter, 0.6 cm thick uncoated optical flat with the surfaces polished to $\lambda/10$ and parallel to 2 sec (Oriel, Stamford, CT, A-43-143-60). When used in the s-polarization mode and at 45°, this provides laser intensities of 11% and 9% for the reference and sample chambers. With this arrangement the return beams to the laser are of the order of 1% and are insufficient to affect the mode stability of the laser. The reference and sample chambers are T-shaped stainless steel tubings 10 cm long, ¼ in i.d., with the stem of the sample chamber connected to a needle value which controls the flow of gas sample into the interaction region. The flow is carefully regulated so that it is barely perceptible to feel. The chambers are windowless i.e., no windows are glued to the ends of the stainless steel tubing. The reason for a windowless cell is because the introduction of windows with surface errors (deviation form planeness) into the FP cavity will reduce the finesse of the system. Moreover, if windows were mounted, there would be reflection loss of the HeNe beam. The interferometer used is of standard design (Burleigh, Fishers, NY, Model-110 with RC-670-C2.3 mirrors). The two light beams are steered through the

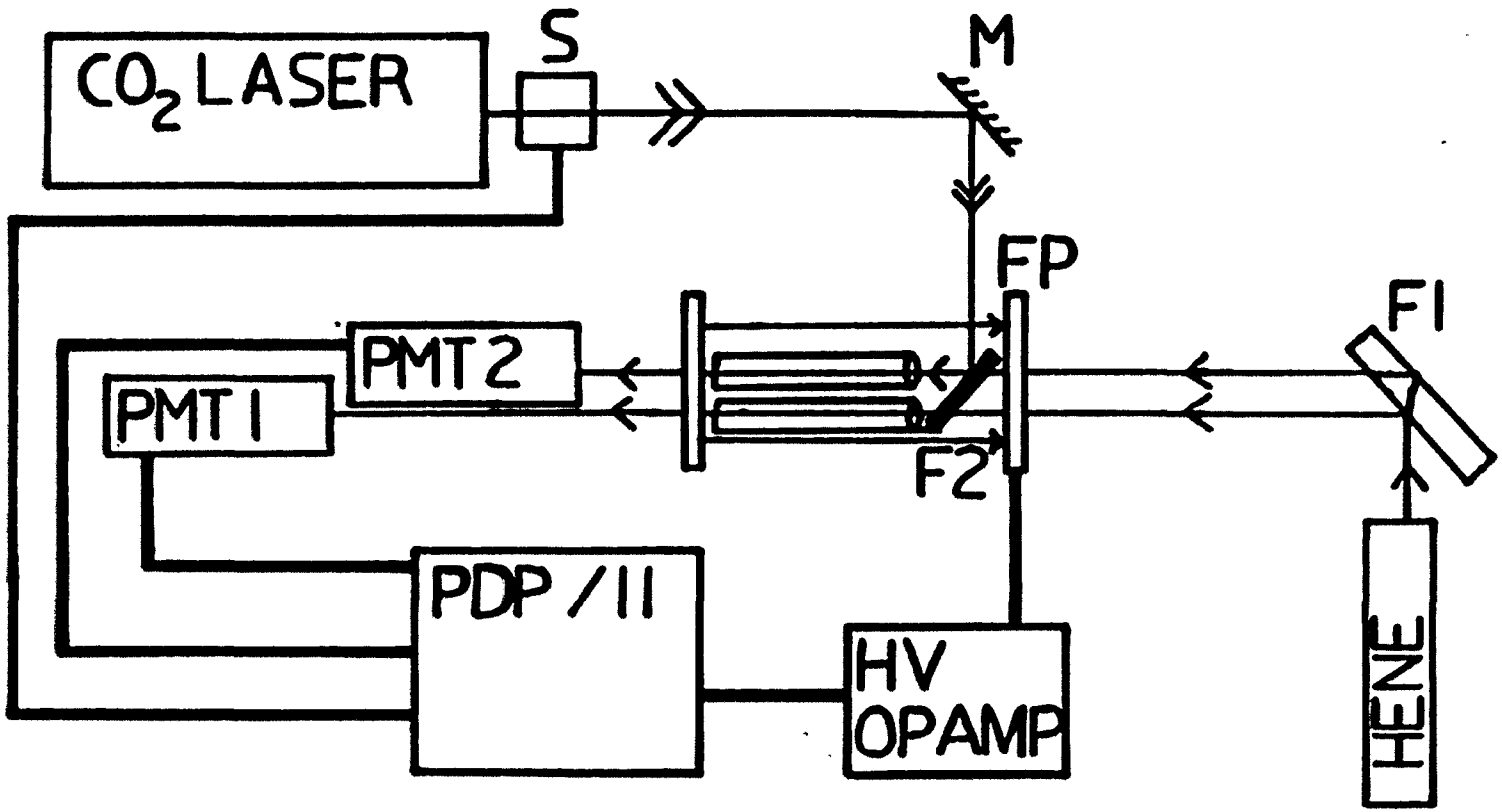

Figure 34. Schematic of the set-up for the dual-beam Fabry-Perot experiment. S-mechanical shutter; F1, F2 - optical flats; PMT1, PMT2 - photomultiplier tubes, FP-Fabry-Perot interferometer

Table 6. Components for dual-beam Fabry-Perot experiment

Component	Model No.	Manufacturer
CO_2 laser	C-250	Molectron, Sunnyvale, CA
HeNe laser	100	Tropel, Fairport, NY
Fabry-Perot Interferometer	RC-100	Burleigh, Fishers, NY
Fabry-Perot mirrors	RC-670-C2.3	Burleigh, Fishers, NY
High voltage operational amplifier	PZ-70	Burleigh, Fishers, NY
Minicomputer with LPS-11 interface	PDP 11/10	Digital Equipment, Maynard, MA
Photomultiplire tube 1	6342A	RCA, Lancaster, PA
Photomultiplier tube 2	1P28	RCA, Lancaster, PA
Mechanical shutter		Tektronix Inc., Beaverton, OR
Thermopile	210	Coherent Radiation, Palo Alto, CA
Microvoltmeter	155	Keithley Instruments, Cleveland, OH
CO_2 Spectrum analyzer		Optical Engineering, Santa Rosa, CA
Capacitance manometers	221A	MKS Instruments, Burlington, MA
Oscilloscope	7904	Tetronix, Beaverton, OR

reference and sample chambers and upon exit from the cavity, are separately directed to two photomultiplier tubes (RCA, Lancaster, PA, 6342A and 1P28) operated at 800V and 400V, respectively. Each PMT is fitted with an interference filter (Rolyn, Arcadia, CA, 66.4540) to reject room light. A CW CO_2 laser of conventional design (Molectron, Sunnyvale, CA, Model C-250) was used as the excitation beam. To introduce this beam, an optical flat made of BaF_2 with an effective flatness of $\lambda/10$ is mounted inside the FP cavity at Brewster's angle with respect to the HeNe beam (see Figure 35). The intensity of the reflected CO_2 laser beam is 14%. The Brewster's angle arrangement ensures minimal reflection loss of the HeNe beam as well as preserves the beam's polarization. The CO_2 laser beam is aligned collinearly with one of the HeNe beams through the sample chamber for maximum overlap between the beams. No effort was made to collimate the CO_2 laser to match the size of the HeNe laser (0.03 cm^2 cross-sectional area). The reason for this rather cumbersome and inefficient arrangement for introducing the CO_2 laser is because the FP mirrors do not transmit infrared radiation. All the optical components were mounted on a base plate and the entire system is set directly on a bench without further vibrational isolation.

To operate, a linear ramp is generated by a minicomputer (Digital Equipment, Maynard, MA, Model PDP 11/10 with LPS-11 laboratory interface), and is amplified by a high-voltage operational amplifier (Burleigh, Fisher, NY, Model PZ-70) to scan the interferometer. For

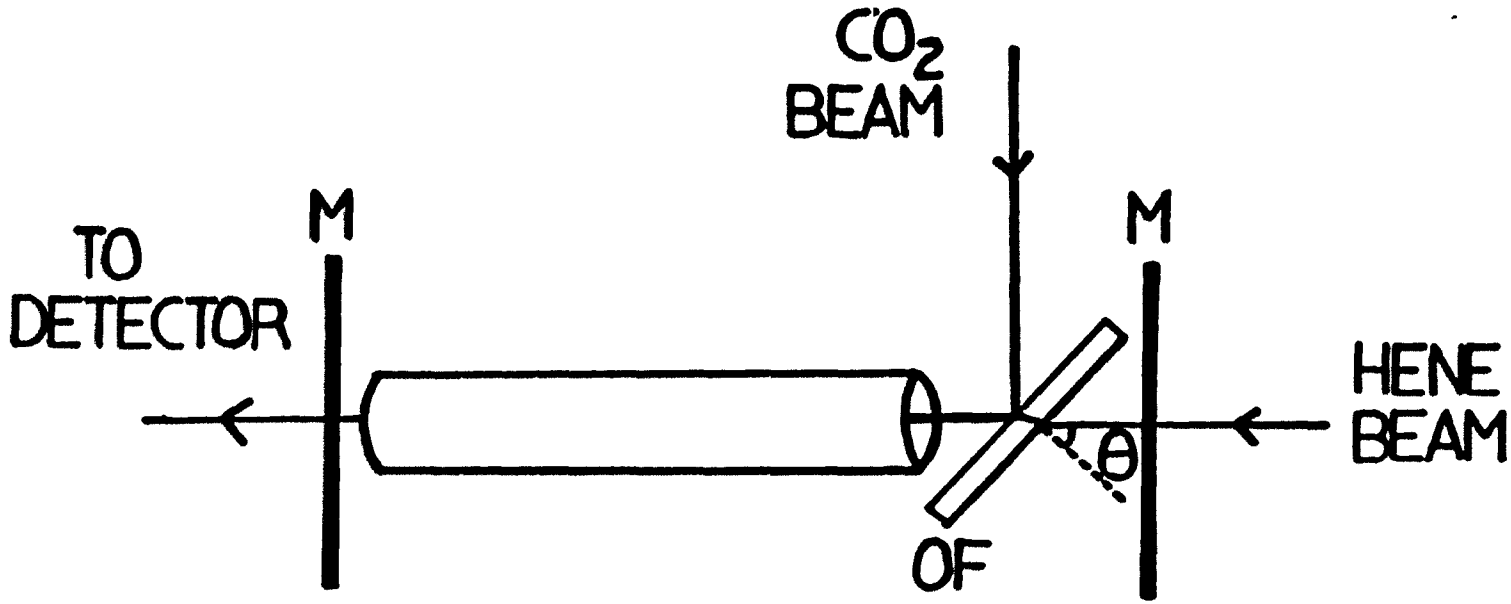

Figure 35. Brewster's angle arrangement. M-Fabry-Perot interferometer mirrors; OF - optical flat made of BaF_2. θ-Brewster's angle

each step in the ramp, the output of each photomultiplier tube is digitized and stored in the computer. After each scan, the computer locates the constructive interference peak for each photo-tube. The free spectral range of the interferometer is adjusted so that there is always one peak, but never more than two peaks per scan for each beam. It is then easy to use an algorithm to monitor the difference in the two beams, regardless of whether one of the peaks in either beam has drifted off the scan range on consecutive scans.

For absorption measurements, gas mixtures of ethylene in pure nitrogen (Matheson, E. Rutherford, NJ) are introduced into the sample chamber by opening the needle valve. When the interfence fringes are finally stabilized, (after a period of equilibration necessary to adjust to the steady flow of gas sample) the CO_2 laser is introduced into the optical path of the sample beam by means of a manually operated mechanical shutter for 0.2 or 0.3 s. The instant the shutter is opened, the computer is triggered to go to a time delay before it takes the first scan and stores the information as described above. Then, it goes to a second time delay before it takes the second scan. The reason for the provision of the two time delays in the computer algorithm is as follows. Assume the induced temperature rise, ΔT, surges to a maximum and undergoes a decay similar to that depicted in Figure 36. Ideally the length of the first time delay should be such that the first scan records the maximum peak shift in the sample beam relative to that of the reference beam, i.e., at the instant when the induced

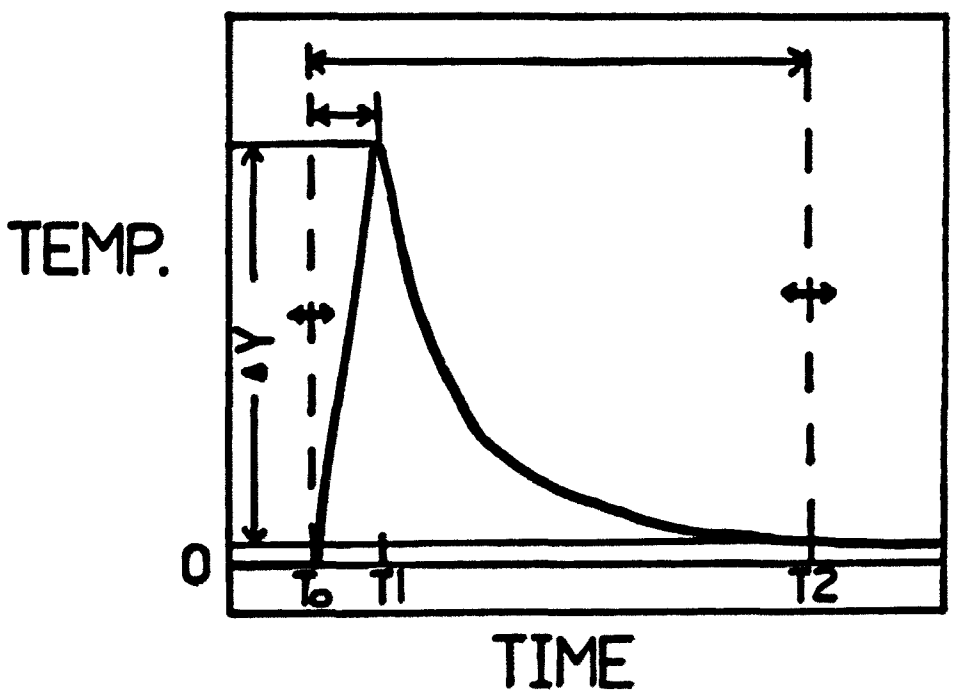

Figure 36. Transient temperature rise and decay model. T_0 - time when the shutter is opened; T_1 - first time delay; T_2 - second time delay. T_1 and T_2 are varied empirically to yield maximum change in terms of temperature, ΔY

temperature rise, ΔT, is highest. This last value depends on the excitation and energy relaxation time of the species. The second time delay, on the other hand, should be so chosen that the second scan "catches" the peak in the sample beam when it shifts back to its pre-irradiated position. This corresponds to a steady state value of the temperature after its initial surge. The time it takes to achieve this value depends on the thermal conduction time of the system and the rate of replenishment of gas sample by the flow. With proper time delays, the computer will be able to measure the maximum net difference in the shift due to absorption, Δd, when the digitized value of the peak position in the second scan is subtracted from that in the first one. The computer program for this study is so written that the values of the two time delays can be adjusted. This way, the maximum signal can be determined empirically.

2. Results and discussion

To test the detectability of this scheme, a gas mixture of C_2H_4 in pure nitrogen with a concentration of 495 ppm was used as the sample. The CO_2 laser line used was the P(14) in the 00°1-10°0 band (α = 32.2 cm^{-1} atm^{-1}). The interference fringe pattern was checked for finesse and free spectral range by displaying the output of each of the photomultiplier tubes on an oscilloscope (Tetronix, Beaverton, OR, Type 205-2, Model A). A typical display of the interference fringe patterns of the two beams is presented in Figure 37.

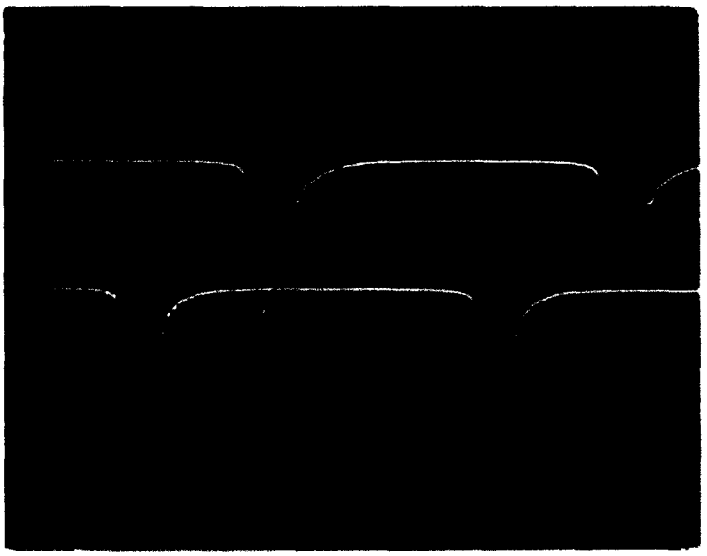

Figure 37. Oscilloscope display of the dual-beam Fabry-Perot interference fringe pattern. Horizontal scale = 10 ms/cm. Vertical scale = 0.2 v/cm

The first item of concern is to establish the values of the two time delays. To do this, the following approach is taken. First, the first time delay is assigned an arbitrary value (typically of the order of tens of ms) and kept constant while the second value is varied in magnitude in a descending order. Meanwhile, the digitized values of the net difference between the two scans, Δd, corresponding to the different values of the second time delay are compared until the maximum is acertained. With this last value, the optimum length of the second time delay is also determined. Next, with the second time delay fixed, the value of the first time delay is varied to see if the magnitude of the previous maximum can be improved upon. By trial and error, the first time delay is determined in this manner. Once these two values are established, subsequent measurements on more diluted samples will be made based upon this set of values. From the initial display on the oscilloscope, it was determined that the range of values assigned to the second time delay should be of the order 10-500 ms. That is we expect that at some point during this time span the system will have completely relaxed and the original peak position re-established. However, when actual measurements were made, it was observed that the magnitude of Δd remained relatively constant over a range of values of the second time delay. This can only be explained by the fact that the decay of ΔT occurs at a much faster rate than anticipated (sub-ms). Upon reviewing the computer algorithm used for this study, it was discovered that each scan which involves the generation of a linear ramp, the digitization of the output of the

photomultiplier tube, the location of interference peak, etc. takes approximately 0.3 s. By the time the first scan is completed, the system will have completely relaxed and the original peak position reestablished, thus defeating the purpose of the second time delay.

While the second time delay was rendered useless by the "untimely" discovery of the scan rate, the first time delay could still be used to yield information regarding the optical excitation and energy relaxation of gaseous species. Subsequent measurements using different values of the first time delay indicate that the energy relaxation process occurs immediately after optical excitation and produces heat in a very short period (sub-ms). This observation agrees with the experimental results of the thermal lens spectroscopic study of nonradiative processes in NO_2 by Imasaka et al. (223) which indicate a rise time of the temperature on the order of 1 μs or less.

3. Conclusion

Although the advantage of the dual-beam arrangement was never quite fully exploited in this study, the basic concept was still sound as evidenced by the success of its adaptation into a RI detector for HPLC (222). To make the present scheme work as an absorption detector for trace gas, several changes have to be made for improvement. First, instead of a manually operated mechanical shutter, an electronic shutter whose "on-off" operation is controlled by a computer should be used. This can be readily accomplished by writing into the algorithm a command that would ask the laboratory interface system (LPS-11) to send a trigger pulse to the shutter to activate it. A

scan can be made right before irradiation (opening of the shutter), with the necessary information stored. Immediately after the shutter is opened, or concurrent with it, a second scan is performed. The information gathered during the two scans can then be compared, and the net difference in shift due to absorption can be calculated. Better synchronization is derived as a result of this alteration.

There is still one problem, the scan rate. If, as determined before, the complete scan with its accompanying digitization and computation takes approximately 0.3 s, then by the end of the first scan, various events (noise) might lead to the shifting of the peak to positions different than that at the beginning of the scan. Subsequent comparison between the two scans will not yield the true, net difference in shift due only to absorption. A faster scan rate will definitely correct this problem. Presently, work is being done in our laboratory to build a faster scanning unit for this purpose (224).

Another advantage of a faster scanning rate is the potential for multi-scans. This will allow more frequent data collection which in turn makes signal averaging possible resulting in improved S/N. The present system, with one scan before and after irradiation, and slow scan rate, does not allow extensive averaging to neutralize noise signals caused by fluctuations in the 0.1 - 1.0 s time scale. Although somewhat reduced by the dual-beam arrangement, these fluctuations can best be minimized by signal averaging.

In addition to a faster scan rate, a pulsed laser can be used as the excitation source. The same amount of energy can be deposited in a shorter time, allowing the instantaneous shift to be registered with minimal effect from other fluctuations.

E. Single-beam Fabry-Perot Interferometry for Gas Detection

An alternative to the dual-beam arrangement described above for trace detection of gas is the single-beam geometry using modulated CW excitation and narrow-band detection. By using a 1-Hz bandwidth tuned at the modulation frequency, thermal and shot noise that are broad band in nature can be reduced substantially. The excitation source can be modulated either mechanically by means of a chopper, or piezoelectrically by means of a PZT pusher as in the PAS study. Using Davis' estimation (119,121), the Fourier component of an induced refractive index change at ω_m, the chopping frequency, in the beam-chopped mode is given by

$$\Delta n(t) \approx \frac{(n-1)I_o A \sin(\omega_m t)}{2D\omega_m C_p T_{abs}} \qquad (4.10)$$

where n is the refractive index, I_o is the intensity of the excitation source in Watt cm^{-2}, A is the absorbance, D is the density of the gas sample in g cm^{-3}, C_p is the specific heat in J $g^{-1}K^{-1}$ and T_{abs} is the absolute temperature in K. Equation (4.10) is derived by assuming

that I_o is nonsaturating and that the thermal conduction time of the system is greater than ω_m^{-1}. From equation (4.10), the minimum detectable absorbance with a 1-Hz detection bandwidth is

$$A_{min} = 2\omega_m \rho C_p T_{abs} \Delta n_{min} / (n-1) I_o \qquad (4.11)$$

One finds sensitivity generally increases with lower modulation frequency, higher laser power being focused into smaller areas, and smaller Δn_{min}. For Fabry-Perot interferometry, Δn_{min} can be as low as 2×10^{-9}. Better collimation of the excitation source will result in a smaller area and hence higher photon flux. But there is a practical limit to the extent of collimation - the cross-sectional area of the probe beam. Reducing the excitation beam to a size smaller than that of the probe beam will result in the inefficient use of the latter beam. Worse yet, it may even create a temperature gradient within the profile of the probe beam. The 1/f behavior of electronic drift and flicker noise effectively puts a limit as to how low the modulation frequency can be reduced. A trade-off has to be made in order to choose an optimum value for ω_m.

The significance of an appropriate modulation frequency actually goes beyond the normal compromise of signal magnitude versus noise. For a system based on a single-beam arrangement with modulated excitation source to work, the interference fringe pattern must be stabilized. In the case of a Fabry-Perot interferometer, it is preferable to maintain the interferometer at its optimum operating point which is the half maximum along either the rising or falling edge of an

interference peak. At this point, Δd, the shift in the position for constructive interference, is most sensitive to the change of the refractive index inside the cavity, Δn. The intensity, as observed by a photodetector monitoring the probe beam (HeNe laser) will be a DC signal corresponding to the intensity at half maximum of the peak. The modulated signal, a result of the instantaneous shift caused by absorption of the excitation source, will appear as an AC component superimposed on the DC signal. Coherent detection of this AC signal is achieved by a phase sensitive device, e.g. a lock-in amplifier, synchronized to the modulation frequency. This arrangement is schematically depicted in Figure 38.

Recalling from the discussion on the types of noise that limit the detectability of a Fabry-Perot interferometer, any device to stabilize the interferometer must also consider the drifting of the interference peak caused by the same types of noise. Examples are laser frequency instability, room pressure changes, thermal expansion of the interferometer mounts, ambient acoustic noise, and mechanical vibrations. From the previous study (222), it was determined that fluctuation caused by these sources of noise were typically in the 0.1-1.0 s time scale. A device designed to maintain the interferometer at its optimum point of operation must therefore be able to respond in the same time scale. The best approach is to use a low-frequency response feedback device which monitors the intensity of the probe beam before and after the beam passes through the FP cavity, compares

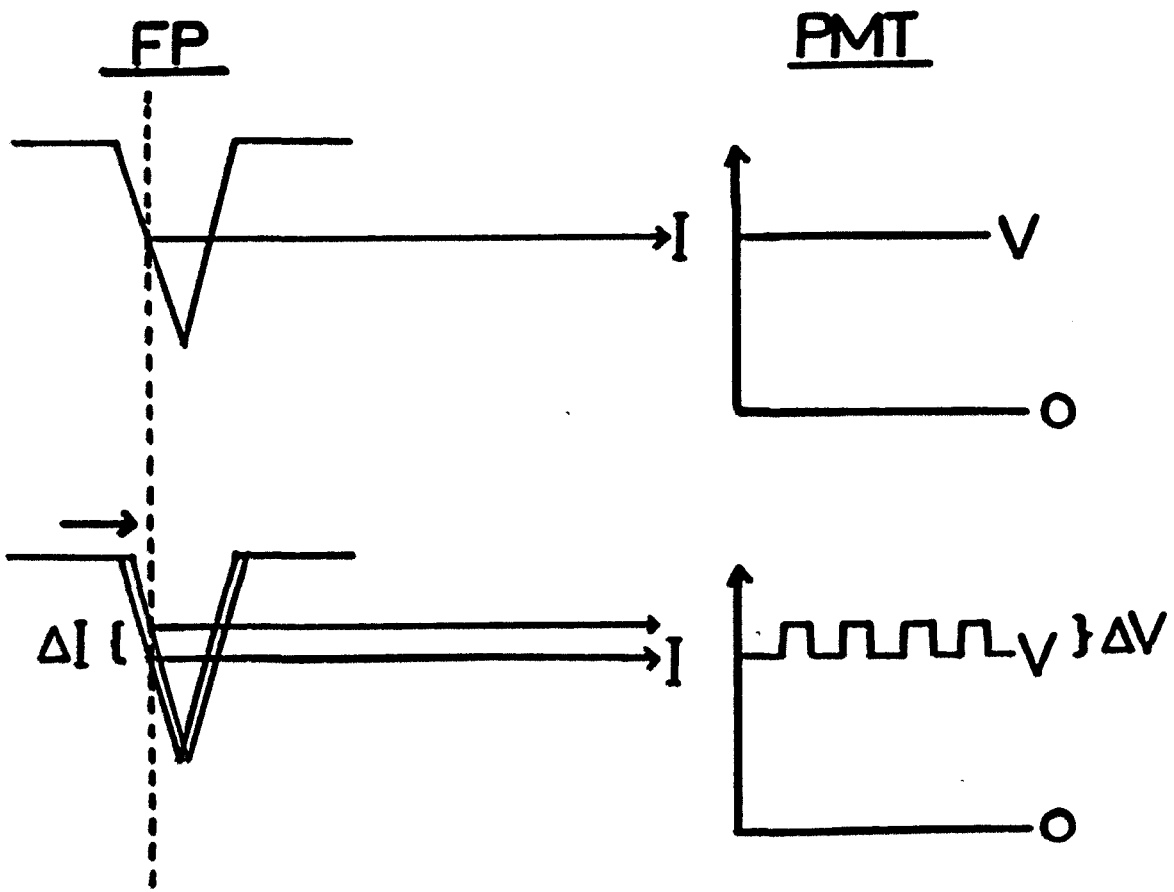

Figure 38. A diagram depicting the generation of a modulated signal in the single-beam Fabry-Perot experiment. FP represents the optimum point of operation at half maximum of a peak slope. PMT represents the corresponding signal observed by the photomultiplier tube. I- light intensity at half maximum; ΔI- instantaneous change in light intensity due to peak shift; V- initial DC output of the photomultiplier tube; ΔV- AC component corresponding to ΔI

these two values, and corrects any drifting by driving accordingly the piezoelectric transducer mounted on the scanning mirror of the interferometer.

There is yet another factor that merits consideration in a single-beam experiment by modulation excitation; the background signal due to residual absorption of the excitation radiation by water molecules, gaseous interferents, and by the heating of chamber walls. In addition, there is heating of the back mirror of the FP interferometer, since the beam never quite exits the FP cavity. All these constitute a modulated background contribution to the observed signal. Several approaches can be used to discriminate against this background contribution, and, one of them is wavelength modulation. The principle behind the operation here is similar to that in the PAS experiment. In subsequent sections, we report the absorption measurements based on Fabry-Perot interferometry utilizing a laboratory build feedback system for stabilization. The performance of this system, together with wavelength modulation will also be presented.

1. Experimental section

The experimental arrangement for the single-beam absorption measurement is similar to that of the dual-beam experiment and is shown in Figure 39. A list of the instruments used is presented in Table 7. The single frequency HeNe laser is split into two beams in the same manner as the dual-beam arrangement. Only one beam is used to traverse through the windowless sample chamber. Samples are flowed into the

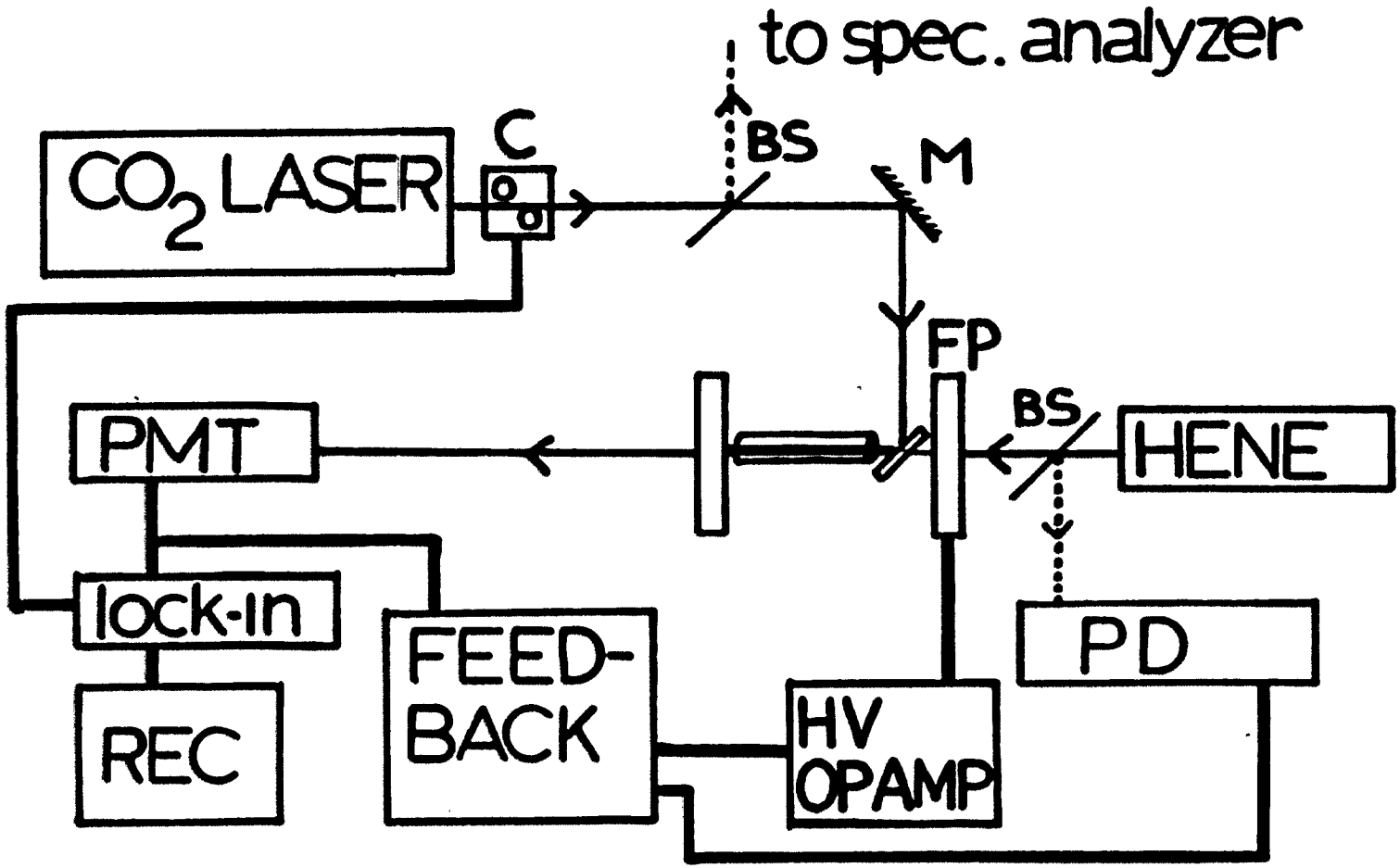

Figure 39. Schematic of the set-up for the single-beam Fabry-Perot experiment with position stabilization feedback system. C - chopper, optional; BS - beam splitter; FP - Fabry-Perot interferometer; PD - photo-diode; PMT - photomultiplier tube

Table 7. Components for single-beam Fabry-Perot experiment

Component	Model	Manufacturer
CO_2 laser	C-250	Molectron, Sunnyvale, CA
HeNe laser	100	Tropel, Fairport, NY
Fabry-Perot interferometer	RC-100	Burleigh, Fishers, NY
Fabry-Perot mirrors	RC-670-C2.3	Burleigh, Fishers, NY
High voltage operational amplifier (2)	PZ-70	Burleigh, Fishers, NY
Wave generator	162	Wavetek, San Diego, CA
Chopper	7500	Rofin, Newton Upper Falls, MA
PZT pusher	PZ-44	Burleigh, Fishers, NY
Photodiode	4220	Hewlett Packett, Palo Alto, CA
Lock-in amplifier	HR-8	Princeton Applied Research, Princeton, NJ
Position stabilization circuit		Laboratory built
Photomultiplier tube	1P28	RCA, Lancaster, PA
Thermopile	210	Coherent Radiation, Palo Alto, CA
Microvoltmeter	155	Keithley Instruments, Cleveland, OH
Digital voltmeter	160B	Keithley Instruments, Cleveland, OH
Microphone	BT-1759	Knowles Electronics, Franklin Park, IL
Chart recorder	B5117-5I	Houston Instrument, Austin, TX
Oscilloscope	7904	Tetronix, Beaverton, OR
Capacitance manometer	221A	MKS Instruments, Burlington, MA
CO_2 spectrum analyzer		Optical Engineering, Santa Rosa, CA

chamber through the same adjustable valve. The CO_2 laser beam is introduced into the FP cavity collinearly with the HeNe laser in the same way as before. All the optical components and the interferometer are mounted on a base plate and, initially, the entire system is set upon a bench directly coupled to the floor without further isolation. Subsequent measurements revealed the need for isolation from floor vibration and other mechanical vibrations encountered in the wavelength modulation mode, discussion of which will be deferred until the next section. Wavelength modulation of the CO_2 laser is provided in similar fashion as in the PAS measurement.

The laboratory-built position stabilization circuit (PSC) is made from 741 operational amplifiers and other stock electrical components. Its schematic is shown in Figure 40. It consists of the following units: two voltage followers with variable gains, a difference amplifier which compares the output voltages of the two previous operational amplifiers, and another difference amplifier which compares the output of the first one to a reference voltage. To function, a portion of the HeNe beam is intercepted by a beam splitter (glass flat) before it enters the FP cavity and directed to a photodiode (PD) which monitors the fluctuations of the beam intensity. The output of the PD is subsequently fed into the positive input terminal of one of the voltage followers of the PSC which amplifies this signal according to the setting of the variable gain. The HeNe beam, upon exit from the FP cavity, is monitored by a second photoelectric

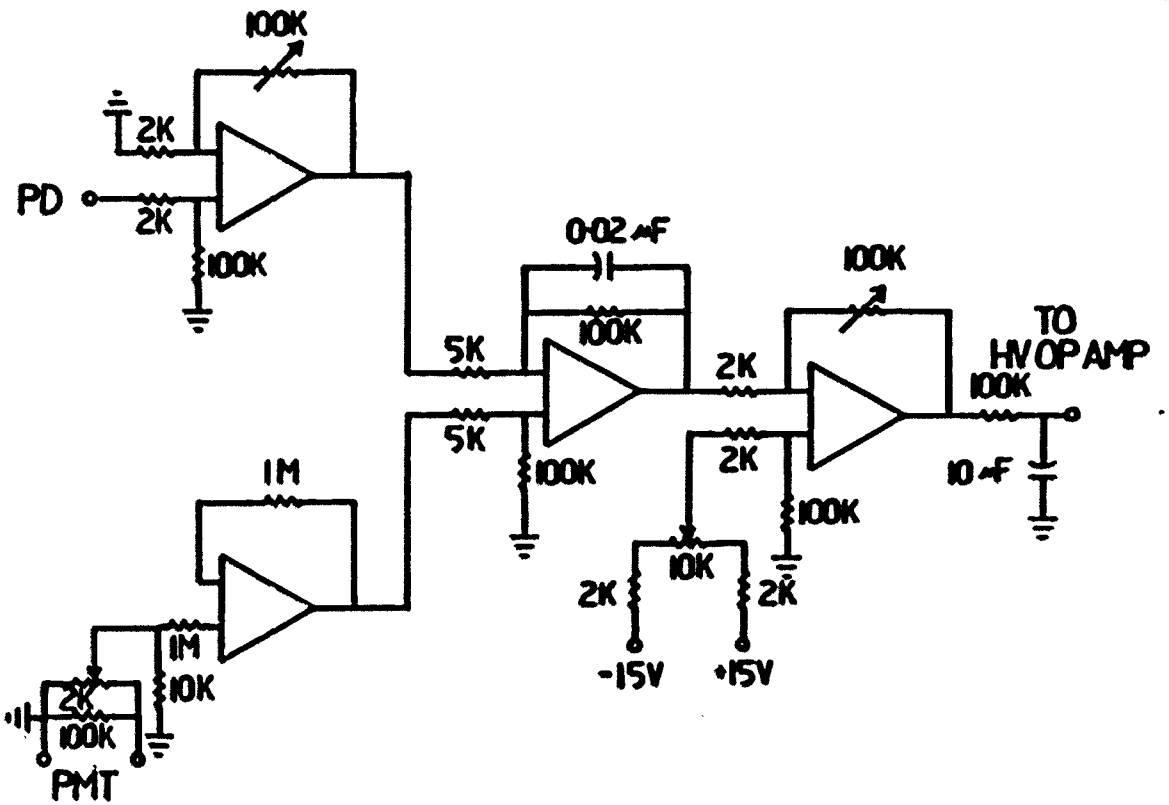

Figure 40. Schematic of the position stabilization circuit

detector, which, in this case, is a photomultiplier tube (PMT) (RCA, Lancaster, PA, 1P28). The output of the PMT is fed to a T-connector, one branch goes to the lock-in amplifier for the eventual absorption signal detection, while the other is forwarded to the positive input terminal of the remaining voltage follower of the PSC. If the interferometer is maintained at any point along the slope of an interference peak, a DC signal will be observed by the PMT. At any other positions along the destructive interference regime, no signal will be registered by the PMT. The outputs of the voltage followers are then compared by the first difference amplifier which amplifies the difference between the voltage levels (x20). This last value is then compared to a reference voltage by the second difference amplifier with an adjustable gain. The final output of the PSC is forwarded to a high-voltage operational amplifier (op amp) (Burleigh, Fishers, NY, Model PZ-44), which amplifies the input signal, and completes the position stabilization feedback loop by sending an output voltage to the piezoelectric transducer mounted on the scanning mirror of the FP interferometer.

To set the scanning mirror at a position where the interferometer is maintained at the half maximum point of an interference peak, the following steps are taken. First, with the circuit on the feedback loop open, positioning of the scanning mirror is achieved by a bias voltage on the piezoelectric transducer available through the high-voltage op amp. When the maximum signal is registered by the PMT, indicating the peak maximum of a fringe, the gains on the two voltage

followers of the PSC are adjusted so that the output of the voltage follower which monitors the PD input (before FP), equals exactly one half of that of the other which monitors the input of the PMT (after FP). This way, the gains are in the ratio of 1:2 (before:after). Subsequent positioning of the scanning mirror at the half maximum will allow the PMT-amplifier to register an output voltage equal to that of the PD-amplifier. This makes the two inputs going into the first difference amplifier of the PSC equal, and hence the output of this amplifier zero. Under such conditions, no correction will be made. If, however, drifts due to noise enumerated before cause the interferometer to "stray" to positions other than the half maximum point, the input signals to the difference amplifier will no longer be equal. As a result, the subsequent output signal will be nonzero. A certain voltage level will be forwarded from the PSC to the high-voltage op amp which, with proper amplification, sends a signal to the piezoelectric transducer to move the scanning mirror to correct for the drifts. The last amplifier of the PSC is to ensure that the polarity and magnitude of the final output signal are compatible with the high-voltage op amp.

2. Results and discussion

The first item of concern is the actual ability of the PSC to maintain the interferometer at the optimum point of operation. The device must respond fast enough to correct for fluctuations that are on the 0.1 - 1.0 s time scale, and yet not too fast so as to cut in the

modulation frequency regime, thus compromising the detection of the AC signal. This is further complicated by the fact that the modulated signal is generally stronger at lower modulation frequency, to the limit that 1/f types of noise do not begin to dominate. A good estimation of the optimum response speed of the PSC to be used is to display the DC output of the PMT on an oscilloscope while the feedback system is operational. With the interferometer approximately maintained at the half maximum point of a slope, the output of the PMT, on initial display, resembled a triangular waveform of high frequency. At the same time, a buzzing sound was generated from the FP cavity. The logical explanation for this phenomenon is that the feedback system is correcting the drifts at too fast a rate. To remedy the situation, two approaches were attempted. First, it was surmised that the gain of the feedback system might exceed the optimum value, causing the circuit to overcompensate. However, when the gain was subsequently turned down, no improvement was observed. The second approach was then adopted which involved putting a time constant on the PSC to deliberately slow down its response speed. The time constant used was basically a RC device and was incorporated into the first difference amplifier stage of the PSC (see Figure 40). With this modification, buzzing was eliminated and the circuit was able to lock in a particular position for an extended period of time. Depending on the relative gains of the two voltage followers as well as the DC bias and gain of the high-voltage op amp, the interferometer can be maintained at any

point along the slope of an interference peak. The general trend seems to be that the overall gain of the feedback system has to be increased as the half maximum point is approached. This is not unreasonable as, nearing the half maximum point, Δd is more susceptible to changes in the refractive indices, Δn.

The DC output of the PMT, however, still has the remnant of a sinusoidal wave of 120 Hz, the second harmonic of the power line frequency, 60 Hz. Since the eventual modulation frequency used is 100 Hz, the presence of 120 Hz noise will affect signal detection to some extent. To suppress this background noise, a simple low pass filter is inserted at the final output of the PSC (see Figure 40). Various combinations of resistance and capacitance were tried before the final 100 KΩ-1 μf was adopted, which has an added advantage of matching the input inpedance of the high-voltage op amp (121 KΩ). The 120 Hz was reduced by a factor of 5 as illustrated in Figure 41.

It is entirely possible that the feedback system, in the process of correcting drifts, also compensates for the modulated signal which would make the detection system useless. The only way to test this is to run a gas sample through the sample chamber and observe the signal generated by a modulated excitation source. Figure 42 shows the signal due to absorption of the P(14) CO_2 laser line by a sample of ethylene in nitrogen (495 ppm) which appears as an AC component superimposed on the quasi-DC output of the PMT.

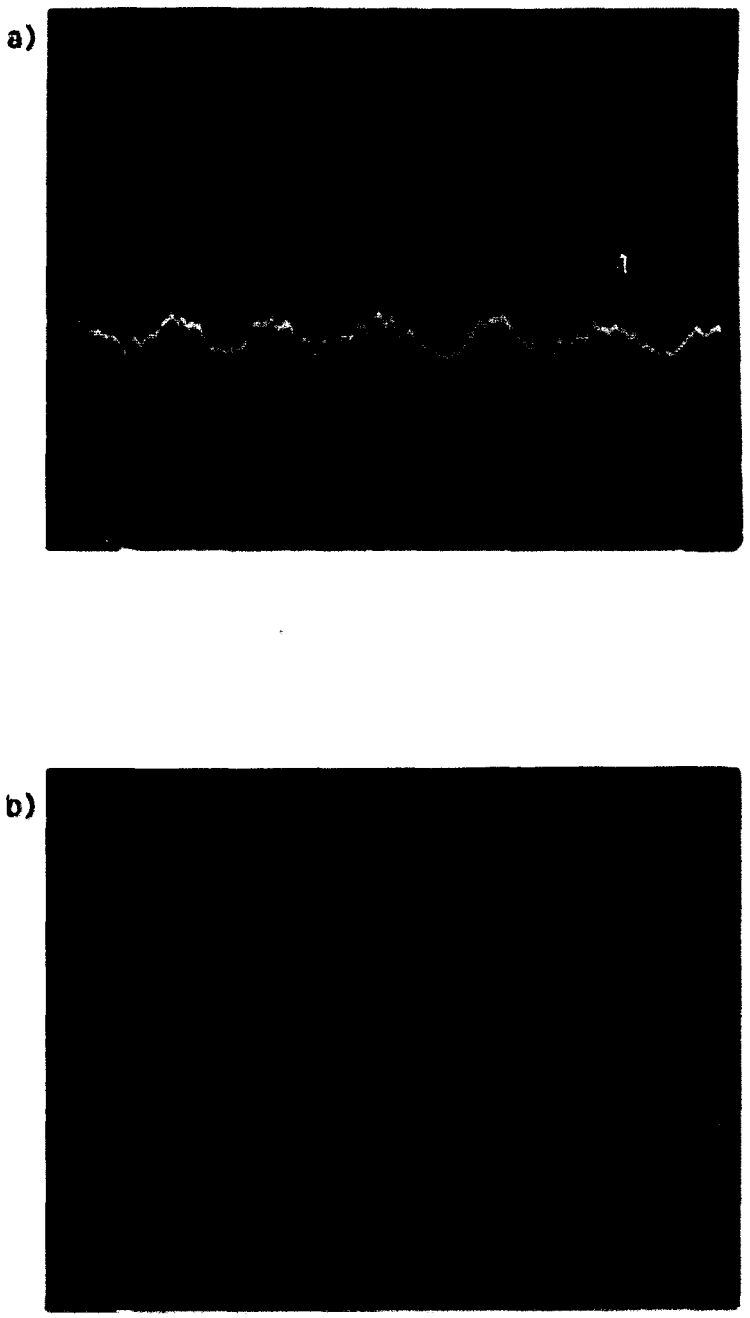

Figure 41. Oscilloscope display of the reduction of the 120 Hz interference by the feedback system. a) No feedback. b) Feedback on. Horizontal scale: 5 ms/cm. Vertical scale: 0.2 V/cm

Figure 42. Oscilloscope display of the modulation signal. a) N_2 flown into the chamber. b) C_2H_4/N_2 (~500 ppm) flown into the chamber. Modulation frequency: 100 Hz. Power = 2.5 W. Horizontal scale: 10 ms/cm. Vertical scale: 0.2 V/cm. Note: upper trace corresponds to zero output of PMT

a)

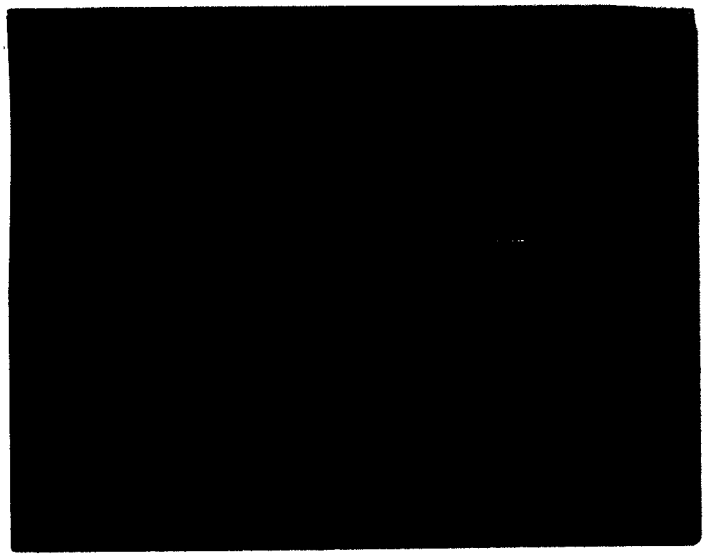

b)

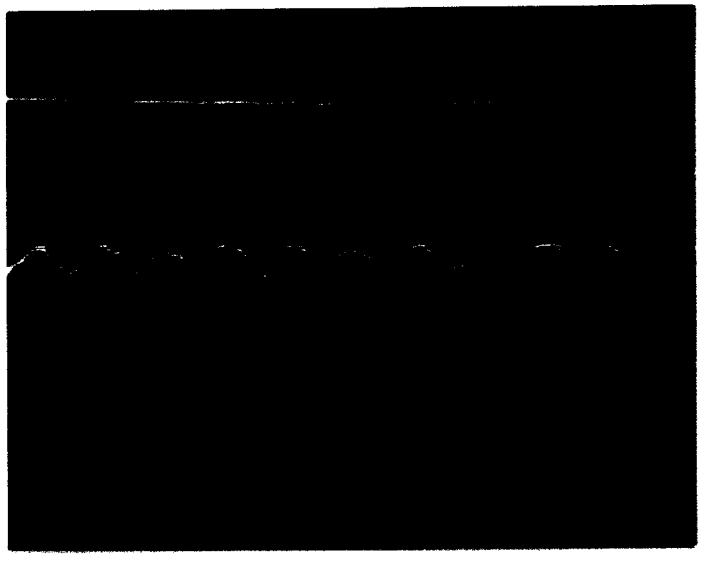

Because of the optical arrangement to introduce the CO_2 laser beam, the windowless sample chamber does not cover the entire FP cavity. The BaF_2 optical flat used to reflect the CO_2 beam has to be mounted at Brewster's angle with respect to the HeNe beam. The air space not covered by the cell amounted to about 5 cm, approximately one third of the entire FP cavity length. As a result, the main contributor of noise is ambient acoustic interference (221) when the interferometer is maintained at its optimum point of operation. The system is not unlike the sensing diaphragm of a sensitive microphone, picking up and amplifying acoustic noise in the surrounding. In addition to acoustic interference, it can also pick up sudden and sporadic vibrations in the room. Examples of these are footsteps, vibrations of floor pumps, etc. This inadvertent pick-up of ambient noise is manifested as tiny ripples superimposed on the DC output of the PMT as shown in Figure 41. The presence of these AC components may or may not affect the ultimate signal detection, depending on the proximity of their equivalent frequencies to the modulation frequency. The problem is somewhat alleviated by narrow-band detection. But, in general, the best approach is through vibration and acoustic isolation.

The problem of acoustic and vibrational interferences became more acute when the system was operating in the wavelength modulation mode. Recalling from the PAS experiment in Chapter 3, the modulation is accomplished through the vibration of the grating mount of the CO_2

laser under the push and pull action of a PZT device. The vibrating mount creates two types of interference: 1) acoustic noise through the laser cavity which acts as an acoustic resonator, and 2) mechanical vibration which is propagated through the bench on which both the CO_2 laser and the FP system rest.

To solve the problem, a series of isolation steps were taken. These included vibration isolation of the CO_2 laser from the bench through layers of foam packing material, vibration isolation of the FP system from the bench first through an air mattress, then by removing the system to a different bench, and acoustic isolation of the FP interferometer by a home-built sound-proof box. With each isolation step, the output of the PMT was observed through the lock-in amplifier (1-s time constant). The trace of noise profiles are presented in Figure 43 for modulation frequency = 100 Hz to illustrate the successive reductions of the interference effect. In sum, a total reduction factor of 3 orders of magnitude was obtained.

To ascertain the detection limit of this system, a gas mixture of ethylene in nitrogen (Matheson, E. Rutherford, NJ) with a concentration of 52.5 ppm was used for measurement. The reference cell used in the PAS experiment was inserted into the CO_2 laser beam to ensure proper adjustments for optimum wavelength modulation. The absolute magnitude of the signal (wavelength modulation) was 114 mV (1-s time constant). The fraction of the CO_2 laser power actually used for excitation was calculated as follows. The two windows of the PAS transmitted about

Figure 43. Noise profile reduction. a) Background signal plus noise profile with no vibration and acoustic isolation. Sensitivity: 500 mV full scale (F.S.). b) Background signal plus noise with CO_2 laser isolated from the bench. Sensitivity: 500 mV F.S. c) Background plus noise with the experimental set-up isolated by air mattress from the CO_2 laser. Sensitivity: 50 mV F.S. d) Background plus noise with the set-up on a different bench. Sensitivity: 20 mV F.S. e) Noise profile with sound proof box. Sensitivity: 20 mV F.S. f) Best noise profile obtained at 3:00 a.m. Friday morning. Sensitivity: 20 mV F.S.

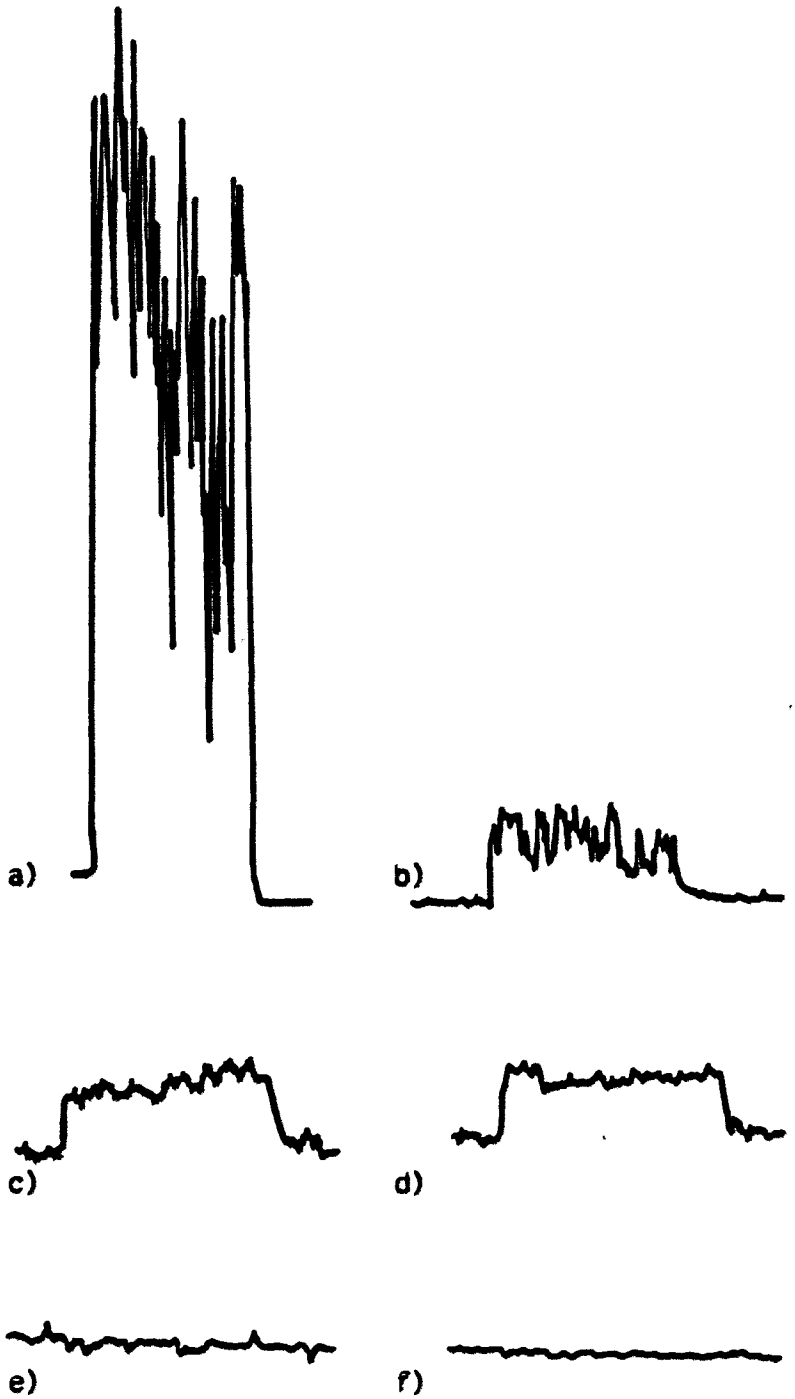
a)
b)
c)
d)
e)
f)

81% of the power ((90%) transmission each). The window on the sound-proof box which acted as an inlet for the CO_2 laser beam also transmitted 90% of the remaining portion. Part of the beam was reflected off to a spectrum analyzer for monitoring the wavelength output. This accounted for a 15% attenuation in the beam power. Finally, the fraction of the beam reflected off the BaF_2 flat for collinear propagation with the HeNe laser amounted to 15%. The cumulative attenuation was therefore about 90.7% or ~ 9.3% of the CO_2 laser power was actually used for excitation. The signal magnitude for the 52.5 ppm sample was normalized against the actual fraction of power used. This came out to be 1226 mV/W. Since the sample mixture has undergone deterioration over the period of this study, a correction factor was applied to recalculate this last value. By estimation, the deterioration factor was determined to be 30%. But a second independent study (225) indicated a more severe sample deterioration factor of 42%. Taking the average of these two values, a final correction factor corresponding to 36% sample deterioration was used. The final corrected signal magnitude was 1915 mV/W. For a residual background noise of 0.24 mV, this amounted to a S/N of 7979. Note that this last value (0.24 mV) is independent of the intensity of the laser light. For operation at 1 W of output, the projected detectability is 20 ppb (S/N = 3). Naturally, higher laser power can be used to improve the detectability, since the background seems to be intensity independent. That the laser power was not increased to achieve better detectability in this study

was due to the fact that the highly reflective coating of the FP mirrors might be stripped had higher power been used. If, however, the mirrors are made of substance (coating included) that is transparent to IR radiation, such precautions can be lifted. This will also permit direct introduction of the CO_2 laser beam into the FP cavity which in turn allows a more efficient use of the laser power, and more spatial overlap between the probe beam and the CO_2 laser because of easier optical alignment. All this will improve the signal strength of this scheme. An added advantage is the more compact FP cavity as a result of removing the Brewster's angle arrangement of the BaF_2 flat. Better finesse and noise rejection will result. Present state of the art technology can manufacture mirrors from substrates such as zinc selenide (ZnSe) which are transparent to both visible and IR radiation with high reflectivity ($\gtrsim$ 90%). The only drawback seems to be the degree of flatness that can be achieved. While the present set of mirrors have a surface finish of $\lambda/200$, the best flatness that can be expected from ZnSe substrate is of the order of $\lambda/50$. However, it is generally believed that such a specification value is an average over the entire surface. In truth, there may be local spots on these mirrors that have a surface finish of better than $\lambda/50$. In any event, the slight decrease in finesse as a result of surface imperfections will be more than compensated for by the other advantages.

The detectability of this study, when compared to those obtained by the phase fluctuation optical heterodyne interferometry coupled with Stark modulation (121), is about a factor of 4 larger (20 ppb vs.

5 ppb). This disparity can readily be lessened by collimating the excitation laser beam to match the size of the probe beam, as in the case of the other study. In our system, the CO_2 laser beam has a diameter of 5 mm whereas the size of the HeNe laser is ~ 2 mm. Reducing the former to the size of the latter will result in an improvement of the present detectability by a factor of ~ 6, thus making it comparable to that of the other study (121). In fact, we believe a significant improvement in performance of the present system can be achieved by further engineering. For example, the position stabilization system described before operated well but was not optimized in that the troublesome 120 Hz line interference, although reduced by a factor of 5, could still pose as a limiting factor for signal detection for ultra trace level of pollutants. A notable reduction of this disturbance may be obtained by simply using a battery to power the position stabilization circuit. Also, there is certainly room for improvement in the vibration and acoustic isolation aspect of this study. These, plus some of the other suggested changes described before can conceivably improve the detectability of the present scheme to approach the minimum detectable change in refractive index, Δn_{min}, which is 2×10^{-9} RI units in a FP interferometer based on the combined performance of commercially available components (221). In addition, the Fabry-Perot geometry has a clear advantage over the other interferometers in that a system finesse of 10 or better is readily achieved compared to the inherent limit of 2 for the Michelson, Mach-Zender (121), or Jamin (217) arrangements.

F. Conclusion

In this chapter, trace detection in gases using Fabry-Perot interferometry was presented. Two experiments were conducted: one based on the direct measurement of signal in a dual-beam arrangement, the other on the coherent detection of signal in a single-beam arrangement utilizing a laboratory-built feedback loop to maintain the interferometer at its optimum point of operation. While the first experiment failed to realize its potential as a sensitive detection scheme because of certain instrumental limitations, the single-beam experiment yielded a projected detection limit of 20 ppb C_2H_4/N_2, comparable to other techniques. This last value can be improved upon by some suggested changes as enumerated before.

V. CONCLUSION

In this dissertation, two thermooptic-based detection systems for gases were developed and studied for their performance in monitoring air pollutants. First, a scheme based on the photoacoustic effect is permitted to operate in the wavelength-modulated mode by a simple adaptation of a commercial CO_2 laser, with good discrimination against background due to window absorption. The same concept can be readily extended to applications in long-path monitoring of atmospheric pollutants, where problems caused by scattering and turbulence severely limit the detectability of most existing systems. Wavelength modulation can also be employed in situations which require the detection of trace levels of certain pollutants in the presence of other interfering species. The ability of a wavelength-modulated scheme in this case to extract a trace signal from a substantial background depends mainly on the ability of the excitation source to provide adjacent lines for which the difference in absorption coefficients of the respective absorbing species is large. In the present study, the incomplete nature of the modulation brings a corresponding decrease in sensitivity. But this can be readily corrected by simple mechanical modifications to allow a deeper modulation extent for the same degree of vibration.

Second, the feasibility of using Fabry-Perot interferometry for in situ trace detection of gases was studied. Two experiments were performed. The first one was based on a dual-beam arrangement, with direct measurement of the shift of an interference fringe as a result

of a change in refractive index caused by the absorption of excitation radiation by the species of interest. Because of certain instrumental limitations, the full benefits of a dual-beam arrangement were never quite exploited to make this a sensitive system for trace gas detection. However, faster scanning rates and better synchronization will definitely improve the present scheme. A faster scanning rate will allow multiscan operation, which in turn permits more frequent data collection. This makes signal averaging possible, resulting in improved S/N.

The second Fabry-Perot interferometric experiment was based on a single-beam geometry using modulated excitation and coherent detection of the signal. The success of this system lies mainly in the ability of a laboratory built position stabilization circuit to maintain the interferometer at its optimum point of operation. By combining this with the wavelength modulation scheme previously used in the photoacoustic experiment, the detectability of the resulting system is comparable to other work. However, ultimately the wavelength modulation fashioned in this work is not the best means possible to eliminate background absorption due to interfering species, heating of chamber wall, etc. This is because of the inherent acoustical and vibrational noise generated by the vibrating grating mount when operating in the wavelength-modulated mode. Elaborate acoustic and vibration isolation is needed to eliminate these types of modulation noise. A possible approach in place of wavelength modulation is to convert the present scheme into a dual-beam detector. The exciting laser can be directed

to both a sample and reference chamber, and the difference in the two paths is recorded by a lock-in amplifier synchronized with the modulated exciting lsaer. In addition to a feedback system to maintain the interferometer at its optimum point of operation, a compensator plate has to be used (inserted into one of the optical paths, preferably the reference) to initially bring the respective interference peaks of the two beams together. This way, when the feedback loop is on and the interferometer is at its optimum point of operation, the photodetectors monitoring the two beams will be able to register a nonzero signal. Subsequent irradiation of both the reference and sample chambers by a modulated source will generate two modulated signals of the same frequency, the difference between which will yield the net absorption signal, assuming nearly equal background in both chambers.

VI. BIBLIOGRAPHY

1. Singer, S. F. "Global Effects of Environmental Pollution"; Springer-Verlag: New York, 1970.

2. Diamant, R. M. E. "The Prevention of Pollution"; Pitman: London, 1974.

3. Singer, S. F. "The Changing Global Environment"; D. Reidel: Boston, 1975.

4. Shaheen, E. I. "Environmental Pollution - Awareness and Control"; Engineering Technology Inc.: Mahomet, Illinois, 1974.

5. Sax, N. I. "Industrial Pollution"; Van Nostrand Rheinhold: New York, 1974.

6. Saunders, P. J. W. "The Estimation of Pollution Damage"; Manchester University Press: Manchester, 1976.

7. Lund, T. "Surveillance of Environmental Pollution and Resources by Electromagnetic Waves"; D. Reidel: Dordrecht, Holland, 1978.

8. Thompson, C. R.; Kates, G.; Cameron, J. W. J. Environ. Qual. 1976, 5, 410.

9. Altshuller, A. P. "Analytical Problems in Air Pollution Control", EPA. Washington, DC, Proc. Environ. Qual. Sensor Workshop, Las Vegas, NV, 1971, 11.

10. Beryand, M. E., Ed., "Air Pollution and Atmospheric Diffusion"; Halstead Press: New York, 1973.

11. Spiro, T. G.; Stigliani, W. M. "Environmental Issues in Chemical Perspective"; State University of New York Press: Albany, New York, 1980.

12. Lippmann, M.; Schlesinger, R. S. "Chemical Contamination in the Human Environment"; Oxford University Press: New York, 1979.

13. American Chemical Society "Cleaning Our Environment - A Chemical Perspective"; 2nd ed.; ACS: Washington, D.C., 1978.

14. Hughes, E. E.; Taylor, J. K. "Accurate Gas Standards for Air Pollution Analysis"; World, Health Organization, Technical Conference on Observation and Measurement of Atmospheric Pollution, Helsinki, Finland, Aug. 4, 1973.

15. American Chemical Society "Cleaning Our Environment - A Chemical Perspective"; 2nd ed.; ACS: Washington D.C., 1978; Chapter 4.

16. Byerly, R. IEEE Trans. 1975, NS-22, 856-869.

17. Morgan, G. B.; Ozolines, G.; Tabos, E. C. Science 1970, 170, 289.

18. Ziegler, E. N. "Advances in Environmental Sciences and Engineering"; Pfafflin, J. R.; Ziegler, E.N., Eds.; Gordon and Breach: New York, 1979; Vol. 1, 184.

19. Likens, G. E. Chem. Eng. News 1976, 54 (48), 29.

20. Molina, M. J.; Rowland, F. S. Nature 1974, 249, 810.

21. Cicerone, R. J.; Stolarski, R. S.; Walters, S. Science 1974, 185, 1165.

22. Su, C.-W.; Goldberg, E. D. Nature 1973, 245, 27.

23. Panofsky, H. A. "Advances in Environmental Science and Engineering"; Pfafflin, J. R.; Ziegler, E. N., Eds.; Gordon and Breach: New York, 1979; Vol. 1, 149.

24. Schneider, S. H.; Kellogg, W. W. "The Chemical Basis for Climate Change", in "Chemistry of the Lower Atmosphere"; Rasool S. I., Ed.; Plenum Press: New York, 1979.

25. Heisler, S. L.; Friedlander, S. K.; Husar, R. B. Atmos. Environ. 1973, 7, 633.

26. de Nevers, N.; Morris, J. R. J. Air Pollut. Control Assoc. 1975, 25, 999.

27. Schiermeir, F. A. Environ. Sci. Technol. 1978, 12, 644.

28. Perry, R.; Young, R. J. "Handbook of Air Pollution Analysis"; Chapman and Hall: London, 1977.

29. Brodelius, S. J.; Smith, L. L. Anal. Chem. 1977, 49 (3), 424.

30. Bruno, P.; Caselli, M.; Della Monica, M.; DiFano, A. Talanta 1979, 26, 1011.

31. Hauser, T. R.; Shy, C. M. Environ. Sci. Technol. 1972, 6 (10), 890.

32. Scaringelli, F. P.; Saltzman, B. E.; Frey, S. A. Anal. Chem. 1967, 39 (14), 1709.

33. Federal Register 38, 1973, No. 110, 15174.

34. Stetter, J. R.; Sedlak, J. M.; Blurton, K. F. J. Chromatogr. Sci. 1977, 15, 125.

35. Kuster, W. C.; Golden, P. D.; Fehsenfeld, F. C. J. Chromatogr. 1981, 2, 271.

36. Bozzelli, J. W.; Kebbekus, B. B. ASTM Spec. Tech. Publ. 1980, 721, 70.

37. Bruner, F.; Ciccioli, P.; Bertoni, G. J. Chromatogr. 1976, 120, 200.

38. Cowen, W. F.; Baynes, R. K. J. Environ. Sci. Health, Part A, 1980, A15 (5), 413.

39. Pellizarri, E. D. Environ. Sci. Technol. 1982, 16 (11), 781.

40. Crow, F. W.; Bjorseth, A.; Knapp, K. T.; Bennett, R. Anal. Chem. 1981, 53 (4), 619.

41. Bove, J. L.; Dalven, P. Int. J. Environ. Anal. Chem. 1981, 10 (3-4), 189.

42. Hodgeson, J. A.; McClenny, W. A.; Stevens, R. K.; "Analytical Methods Applied to Air Pollution Measurements"; Stevens, R. K.; Herget, W. F., Eds.; Ann Arbor Science: Ann Arbor, MI, Chapter 2.

43. Kummer, W. A.; Pitts, J. N. Jr.; Sleer, R. P. Environ. Sci. Technol. 1971, 5, 1045.

44. Winer A. M.; Peters, J. W.; Smith, J. P.; Pitts, J. N. Jr. Environ. Sci. Technol. 1974, 8 (13), 1118.

45. Yeung, E. S.; Spurlin, S. R. Anal. Chem. 1982, 54 (2), 318.

46. Eaton, W. C. "Use of flame photometric detector method for measurement of sulfur dioxide in ambient air"; EPA - 600/4-78-78-024, 1978.

47. Okabe, H.; Splitstone, P. L.; Ball, J. J. J. Air Pollutant Control Assoc. 1973, 32 (6), 514.

48. Scott, W. E.; Stephens, E. R.; Haust, P. L.; Doerr, R. C. Proc. Am. Petrol. Inst. Sect. III, 1957, 37, 171.

49. Crable, J. V.; Taylor, D. G. "NIOSH Manual for Analytical Methods"; HEW Pub. No. (NIOSH) 75-121, 1974.

50. Wilks, P. A. Jr. "Microscopy/Pollution Analysis", Ser. 2; International Scientific Communications: Fairfield, Connecticut, 1977; Vol. 3, 252.

51. Maugh, T. H., II. Science 1972, 177, 685.

52. Collis, R. T. H.; Russel, P. B. "Laser Monitoring of the Atmosphere"; Hinkley, E. D., Ed.; Springer-Verlag: Berlin, 1976; Chapter 4.

53. Menzies, R. T. "Laser Monitoring of the Atmosphere"; Hinkley, E. D., Ed.; Springer-Verlag: Berlin, 1976; Chapter 7.

54. Hall, F. F., Jr. "Laser Applications"; Ross, M. Ed.; Academic Press: New York, 1974; Vol. 2, 161.

55. Kildal, H.; Byer, R. L. Proc. IEEE 1971, 59, 1644.

56. Yeung, E. S. "Laser in Chemical Analysis"; Lytle, F. E.; Hieftje, G. M.; Travis, J. C., Eds.; Humana Press: Clifton, NJ, 1981; Chapter 14.

57. Menzies, R. T.; Shumate, M. S. Appl. Opt. 1976, 15, 2080.

58. Shumate, M. S.; Menzies, R. T.; Grant, W. B.; McDougal, D. S. Appl. Opt. 1981, 20, 545.

59. Kobayaki, T.; Inaba, H. Appl. Phys. Lett. 1970, 17, 139.

60. Golden, B. M.; Yeung, E. S. Anal. Chem. 1975, 47, 2132.

61. Melngailis, I. "Laser Spectroscopy"; Brewer, R.G.; Mooradian, A., Eds.; Plenum Press: New York, 1974; 237.

62. Hinkley, E. D.; Nill, K. W.; Blum, F. A. "Laser Spectroscopy of Atoms and Molecules"; Walther, H., Ed., Springer-Verlag: Berlin, 1976; Chapter 2.

63. Steinfeld, J. I. "Molecules and Radiation - An Introduction to Modern Molecular Spectroscopy"; Harper and Row: New York, 1974.

64. Hinkley, E. D.; Harman, T. C.; Freed, C. Appl. Phys. Lett. 1968, 13, 49.

65. Hinkley, E. D.; Ku, R. T.; Kelley, P. L. "Laser Monitoring of the Atmosphere"; Hinkley, E. D., Ed.; Springer-Verlag: Berlin, 1976, 249.

66. Hinkley, E. D.; Freed, C. Phys. Rev. Lett. 1969, 23, 277.

67. Chang, T. Y.; Morris, R. N.; Yeung, E. S. Appl. Spectrosc. 1981, 35, 587.

68. Hinkley, E. D.; Kelley, P. L. Science 1971, 171, 635.

69. Hinkley, E. D. Opto-Electron. 1972, 4, 69.

70. Ku, R. T.; Hinkley, E. D.; Sample, J. D. Appl. Opt. 1975, 14, 854.

71. DeSilets, C. S.; Patel, C. K. N. Appl. Phys. Lett. 1973, 22, 543.

72. Patel, C. K. N.; Shaw, E. D. Phys. Rev. Lett. 1970, 24, 451.

73. Patel, C. K. N.; Burkhardt, E. G.; Lambert, C. A. Opt. Quant. Electron 1976, 8, 145.

74. Kreuzer, L. B.; Patel, C. K. N. Science 1971, 173, 45.

75. Kerr, E. L.; Atwood, J. G. Appl. Opt. 1968, 7, 915.

76. Schnell, W.; Fischer, G. Opt. Soc. Am. 1978, 2, 67.

77. Krueger, G. Appl. Opt. 1982, 21 (15), 2841.

78. Menzies, R. T. Appl. Opt. 1971, 10 (7), 1532.

79. Kreuzer, L. B.; Kenyon, N. D.; Patel, C. K. N. Science 1972, 177, 347.

80. Kaldor, A. Science 1972, 176, 508.

81. Sweger, D. M.; Freund, S. M.; Travis, J. C. NBS Special Publ. 464, 1977, 317.

82. Freund, S. M.; Sweger, D. M.; Travis, J. C. Anal. Chem. 1976, 48 (13), 1944.

83. Sweger, O. M.; Travis, J. C. Appl. Spectrosc. 1979, 33 (1), 46.

84. Alcock, A. J.; Leopold, K.; Richardson, M. C. Appl. Phys. Lett. 1973, 23, 562.

85. Kildal, H., Deutsch, T. F. Appl. Phys. Lett. 1975, 27, 500.

86. Harris, N. W.; O'neill, F.; Whitney, W. T. Appl. Phys. Lett. 1974, 25, 148.

87. Abrams, R. L. Appl. Phys. Lett. 1974, 24, 304.

88. Harris, S. E. Proc. IEEE 1969, 57, 2096.

89. Hennigsen, T.; Garbury, M.; Byer, R. L. Appl. Phys. Lett. 1974, 24, 242.

90. Baumgartner, R. A.; Byer, R. L. Appl. Opt. 1978, 17, 3555.

91. Pinard, J.; Young, J. F. Opt. Comm. 1972, 4, 425.

92. Yeung, E. S.; Moore, C. B. J. Am. Chem. Soc. 1971, 93, 2059.

93. Dewey, C. F., Jr.; Hocker, L. O. Appl. Phys. Lett. 1971, 18, 58.

94. Pine, A. S. J. Opt. Soc. Am. 1974, 64, 1683.

95. Rothe, K. W.; Brinkmann, U.; Walther, H. Appl. Phys. 1974, 3, 115.

96. Grant, W. B.; Hake, R. D., Jr.; Liston, E. M.; Robbins, R. C.; Procter, E. K., Jr. Appl. Phys. Lett. 1974, 24, 550.

97. Grant, W. B., Hake, R. D., Jr. J. Appl. Phys. 1975, 46, 3019.

98. Strotter, H. W. "Advances in Infrared and Raman Spectroscopy", Clark, R. J. H.; Hewter, R. E., Eds.; Heydon and Son: London, 1981; Vol. 8, Chapter 1.

99. Inaba, H. "Laser Monitoring of the Atmosphere"; Hinkley, E. D., Ed.; Springer-Verlag: Berlin, 1976; Chapter 5.

100. Schrotter, H. W.; Klockner, H. W. "Raman Spectroscopy of Traces and Liquids"; Wever, A.; Ed., Springer-Verlag: Berlin, 1979; Chapter 3.

101. Menzies, R. T.; Shumate, M. S. IEEE/OSA Conf. on Laser Engineering and Applications, Washington, D.C., 1975, Paper 9.2.

102. Zipf, E. C.; Keyser, L. F.; Kaufman, F. Chem. Phys. Lett. 1968, 2 (6), 523.

103. Sakurai, K.; Bioida, H. P. J. Chem. Phys. 1969, 50 (6), 2404.

104. Sackett, P. B.; Yardley, J. T. Chem. Phys. Lett. 1970, 6 (4), 323.

105. Abe, K.; Myers, F.; McCubbin, T. K.; Polo, S. R. J. Mol. Spectrosc. 1971, 38, 552.

106. Stevens, C. G.; Swagel, M. W.; Wallace, R.; Zare, R. N. Chem. Phys. Lett. 1973, 18 (4), 465.

107. Fincher, C. C.; Tucher, A. W.; Birnbaum, M.; Paur, R. F.; McClenny, W. A. Appl. Opt. 1977, 16 (5), 1359.

108. Gelbwachs, J. A.; Birnbaum, M.; Tucker, A. W.; Fincher, C. L. Opto. Electronics 1972, 4, 155.

109. Tucher, A. W.; Birnbaum, M.; Fincher, C. L. Appl. Opt. 1975, 14 (6), 1418.

110. Katayama, N.; Robinson, J. W. Spectros. Lett. 1975, 8 (1), 61.

111. Robinson, J. W.; Reid, W. M. Environ. Lett. 1974, 7 (9), 195.

112. Robinson, J. W.; Nettles, D.; Jowett, P. L. H. Anal. Chem. Acta 1977, 92 (1), 13.

113. Reid, J.; Shewchun, J.; Garside, B. K.; Ballik, E. A. Appl. Opt. 1978, 17, 300.

114. Reid, J.; Garside, B. K.; Shewchun, J. Opt. Quant. Electron. 1979, 11, 385.

115. Griffith, J. A. R. Philos. Trans. R. Soc. London 1982, A307, 563.

116. Menzies, R. T.; Shumate, M. S. Science 1974, 184, 570.

117. Mumma, M.; Kostiuk, T.; Cohen, S.; Buhl, D.; von Thuna, P. C. Nature 1975, 253, 514.

118. Menzies, R. T.; Rutledge, C. W.; Lanteson, R. A.; Spears, D. L. Appl. Opt. 1981, 20 (4), 536.

119. Davis, C. C. Appl. Phys. Lett. 1980, 36 (7), 515.

120. Davis, C. C.; Petuchowski, S. J. Appl. Opt. 1981, 20 (14), 2539.

121. Campillo, A. J.; Lin, H.; Dodge, C. J.; Davis, C. C. Optics Lett. 1980, 5 (10), 424.

122. Kreuzer, L. B. J. Appl. Phys. 1971, 42, 2934.

123. Patel, C. K. N.; Burkhardt, E. G.; Lambert, C. A. Science 1974, 184, 1173.

124. Burkhardt, E. G.; Lambert, C. A.; Patel, C. K. N. Science 1975, 188, 1111.

125. Claspy, P. C.; Ha, C.; Pao, Y.-H. Appl. Opt. 1977, 16 (11), 2972.

126. Vansteenkiste, T. H.; Faxvog, F. R.; Roessler, D. M. Appl. Spectrosc. 1981, 35, 194.

127. Rosengren, L. G. Appl. Opt. 1975, 14, 1960.

128. Dewey, C. F., Jr.; Kamm, R. D.; Hackett, C. E. Appl. Phys. Lett. 1973, 23 (11), 633.

129. Goldan, P. D.; Goto, K. J. Appl. Phys. 1974, 45, 4350.

130. Max, E.; Rosengren, L.-G. Opt. Comm. 1974, 11, 422.

131. Deaton, T. F.; Depatie, D. A.; Walker, T. W. Appl. Phys. Lett. 1975, 26, 300.

132. Boncyck, P. A.; Ultee, C. J. Opt. Comm. 1972, 6, 196.

133. Kaldor, A.; Olson, W. B.; Maki, A. G. Science 1972, 176, 508.

134. Kavaya, M. F.; Margolis, J. S.; Shumate, M. S. Appl. Opt. 1979, 18, 2602.

135. Chakerian, C., Jr.; Weisbach, M. F. J. Opt. Soc. Am. 1973, 63, 342.

136. Shtrikman, S.; Slatkine, M. Appl. Phys. Lett. 1977, 31, 830.

137. Gerlach, R.; Amer, N. M. Appl. Phys. Lett. 1978, 32, 228.

138. Koch, K. P.; Lahman, W. Appl. Phys. Lett. 1978, 32, 289.

139. Claspy, P. C.; Pao, Y. H.; Kwong, S.; Nodov, E. Appl. Opt. 1976, 15, 1506.

140. Terhune, R. W.; Anderson, F. E. Opt. Lett. 1977, 1, 70.

141. Bruce, C. W.; Sojka, B. Z.; Hurd, B. G.; Watkins, W. R.; White, K. O.; Dersko, Z. Appl. Opt. 1976, 15, 2970.

142. Perlmutter, P.; Shtrikman, S.; Slatkine, M. J. Opt. Soc. Am. 1980, 70, 1006.

143. Bell, A. G. Proc. Am. Assoc. Adven. Sci. 1880, 29, 115.

144. Tyndall, J. G. Proc. R. Soc. Lond. 1881, 31, 307.

145. Rontgen, W. C. Philos. Mag. 1881, 11, 308.

146. Viengerov, M. L. Dokl. Akad. Nauk SSSR 1938, 19, 687.

147. Viengerov, M. L. Izv. Akad. Nauk SSSR 1940, Fiz 4, 94.

148. Gorelik, G. Dokl. Akad. Nauk SSSR 1946, 54, 779.

149. Slobadskaya, P. V. Izv. Akad. Nauk SSSR 1948, Fiz. 12, 656.

150. Cottrell, T. L.; Macfarlane, I. M.; Read, A. W.; Young, A. H. Trans. Faraday Soc. 1966, 62, 2655.

151. Houghton, J. T.; Smith, D. S. "Infrared Physics"; Oxford: England, 1966, 276.

152. Roessler, D. M.; Faxvog, F. R. J. Opt. Soc. Am. 1979, 69, 1699.

153. Moffat, A. J.; Robbins, J. R.; Barringer, A. R. Atmos. Environ. 1971, 5, 511.

154. Williams, D. T.; Hagar, R. N., Jr. Appl. Opt. 1970, 9, 1597.

155. Dewey, C. F., Jr. Opt. Eng. 1974, 13, 483.

156. Kritchman, E.; Shtrikman, S.; Slatkin, M. J. Opt. Soc. Am. 1978, 68, 1257.

157. Kreuzer, L. B. "Optoacoustic Spectroscopy and Detection"; Pae, Yoh-Han, Ed.; Academic Press: New York, 1977.

158. Wake, D. R.; Amer, N. M. Appl. Phys. Lett. 1979, 34, 379.

159. Goldring, H.; Szöke, A.; Zamir, E.; Ben-Reuven, A. J. Chem. Phys. 1968, 49, 4253.

160. Fraim, F. W.; Murphy, P. V.; Ferram, R. J. J. Acoust. Soc. Am. 1973, 53, 1601.

161. Rosengren, L.-G. Infrared Phys. 1973, 13, 109.

162. Parker, J. G. Appl. Opt. 1973, 12, 2974.

163. McCoy, J. H.; Reusch, D. B.; Long, R. K. Appl. Opt. 1969, 8, 1471.

164. Kamm, R. G. J. Appl. Phys. 1976, 47, 3550.

165. Leslie, D. H.; Trusty, G. L. Appl. Opt. 1981, 20, 1941.

166. Patel, C. K. N.; Kerl, R. J. Appl. Phys. Lett. 1977, 30, 578.

167. Chang, T. Y. "Spectroscopic Analysis of Gaseous Air Pollutants with Tunable Diode Lasers", Ph.D. Thesis, Iowa State University, Ames, Iowa, 1981.

168. Dewey, C. F., Jr. "Optoacoustic Spectroscopy and Detection", Pao, Y.-H., Ed.; Academic Press: New York, 1977, 47.

169. Shimizu, F. J. Chem. Phys. 1970, 52, 3572.

170. Freund, S. M.; Ousbury, G.; Römheld, M.; Tiedje, J. T.; Oka, T. J. Mol. Spectrosc. 1974, 52, 38.

171. Knapp, K.; Hanson, R. K. Appl. Opt. 1983, 22, 1980.

172. Freund, S. M.; Hongen, J. T.; Lafferty, W. J. Can. J. Phys. 1975, 53, 1929.

173. Koloshnikov, V. G.; Kuritsyn, Y. A.; Pak, I.; Ulitsky, N. I.; Kharlamov, B. M.; Brutov, A. D.; Zasavitsky, I. I.; Shotov, A. P. Opt. Comm. 1980, 35, 213.

174. Brand, J. C. D.; Harwick, J. L.; Humphrey, D. R.; Hamada, Y.; Merer, A. J. Can. J. Phys. 1976, 54, 186.

175. Kelley, M. J.; Thomas, J. E.; Monchalin, J.-P.; Kurnit, N. A.; Javan, A. Phys. Rev. Lett. 1976, 37, 686.

176. O'Haver, T. C. Anal. Chem. 1979, 51, 91A.

177. Snellman, W.; Rains, T.; Yee, H.; Cook, H.; Menis, O. Anal. Chem. 1970, 42, 394.

178. Epstein, M. S.; Rains, T. C.; O'Haver, T. C. Appl. Spectrosc. 1976, 30, 324.

179. Skogerboe, R. K.; Lamonthe, P. J.; Bastiaans, G. J.; Freeland, S. J.; Coleman, G. N. Appl. Spectrosc. 1976, 30, 495.

180. Snellman, W. Spectrochim. Acta 1968, 23B, 403.

181. Harnly, J. M.; O'Haver, T. C. Anal. Chem. 1977, 49, 2187.

182. Lipari, E.; Plankey, F. W. Anal. Chem. 1978, 50, 386.

183. Goff, D. A.; Yeung, E. S. Anal. Chem. 1978, 50, 625.

184. Zander, T. A.; O'Haver, T. C.; Keliher, P. N. Anal. Chem. 1977, 49, 838.

185. Castleden, S. L.; Kirkbright, G. F.; Spillane, D. E. M. Anal. Chem. 1981, 53, 2228.

186. O'Haver, T. C. "Contemporary Topics in Analytical and Clinical Chemistry"; Hercules, D., Ed.; Plenum Press: New York, 1978; Vol. 2, Chapter 1.

187. Welling, H.; Litfin, G.; Beigang, R. "Laser Spectroscopy III"; Hall, J. L.; Carlsten, J. L., Eds.; Springer-Verlag: New York, 1977; 370.

188. Konjevic, N.; Jovicevic, S. Spectrosc. Lett. 1979, 12, 259.

189. Nelkon, M.; Parker, P. "Advanced Level Physics"; Heinemann Educational Books Ltd.: London, 1971, 970.

190. Mann, C. K.; Vickers, T. J.; Gulick, W. M. "Basic Concepts in Electronic Instrumentation"; Harper & Row: New York, 1974, 17.

191. Perlmutter, P.; Shtrikman, S.; Slatkine, M. Appl. Opt. 1979, 18, 2267.

192. Stellmack, M. L.; Street, K. W., Jr. Amer. Lab. 1982, 14, No. 12, 25.

193. Gordon, J. P.; Leite, R. C. C.; Moore, R. S.; Porto, S. P. S.; Whinnery, J. R. J. Appl. Phys. 1975, 36, 3.

194. Harris, J. M.; Dovichi, N. J. Anal. Chem. 1980, 52, A695.

195. Dovichi, N. J.; Harris, J. M. Anal. Chem. 1979, 51, 728.

196. Imasaka, T.; Miyaski, K.; Ishibashi, N. Anal. Chim. Acta 1980, 115, 407.

197. Haushalter, J. P.; Morris, M. D. Appl. Spectrosc. 1980, 34, 445.

198. Swofford, R. L.; Morrell, J. A. J. Appl. Phys. 1978, 49, 3667.

199. Flynn, G. W. "Chemical and Biochemical Applications of Lasers"; Moore, C. B., Ed.; Academic Press: New York, 1974; Vol. 1, Chapter 6.

200. Forneth, W. E.; Flynn, G. W.; Slater, R.; Turro, N. J. J. Am. Chem. Soc. 1976, 98, 7877.

201. Bailey, R. T.; Cruickshank, F. R.; Johnstone, W.; Pugh, P. J. Mol. Struct. 1980, 60, 25.

202. Boccara, A. C.; Fournier, D.; Badoz, J. Appl. Phys. Lett. 1980, 36, 130.

203. Boccara, A. C.; Fournier, D.; Jackson, W.; Amer, N. M. Opt. Lett. 1980, 5, 377.

204. Fournier, D.; Boccara, A. C.; Amer, N. M.; Gerlach, R. Appl. Phys. Lett. 1980, 37, 519.

205. Edwin, R. P.; King, W. H. J. Phys. B 1969, 2, 260.

206. Epstein, G. L.; Davis, S. P. Phys. Rev. A 1971, 4, 464.

207. Lewis, E. L. Am. J. Phys. 1977, 45, 38.

208. Allkins, J. R. Anal. Chem. 1975, 47, 752A.

209. Hartig, W.; Walther, H. Appl. Phys. 1973, 1, 171.

210. Monchalin, J.-P.; Kelly, M. F.; Thomas, J. E.; Kurnit, N. A.; Szöke, A.; Zernike, F.; Lee, P. H.; Javan, A. Appl. Opt. 1981, 20, 736.

211. Woods, P. T.; Shotton, K. C.; Rowley, W. R. C. Appl. Opt. 1978, 17, 1048.

212. Stone, J. J. Opt. Soc. Am. 1972, 62, 327.

213. Michelson, A. A. Philos. Mag. 1891, Ser. 5, 31, 256.

214. Michelson, A. A. Philos. Mag. 1892, Ser. 5, 34, 280.

215. Becker, E. D.; Farrar, T. C. Science 1972, 178, 361.

216. Burroughs, W. J.; Chamberlain, J. Infrared Phys. 1971, 11, 1.

217. Cremers, D. A.; Keller, R. A. Appl. Opt. 1982, 21, 1654.

218. Lin, H. G.; Gaffney, J. S.; Campillo, A. J. J. Chromatogr. 1981, 206, 205.

219. Born, M.; Wolf, E. "Principles of Optics", 4th ed.; Pergamon Press, Oxford: 1970; 331.

220. Technical memo for model RC-110 Fabry-Perot interferometer, Burleigh, Fishers, NY.

221. Woodruff, S. D.; Yeung, E. S. Anal. Chem. 1982, 54, 1174.

222. Woodruff, S. D.; Yeung, E. S. Anal. Chem. 1982, 54, 2124.

223. Imasaka, T.; Shimanoe, K.; Ishibashi, N. J. Chem. Phys. 1983, 79, 3201.

224. Chen, G.-Y.; Yeung, E. S. Unpublished results, Iowa State University, Ames, Iowa.

225. Spurlin, S.; Yeung, E. S. Unpublished results, Iowa State University, Ames, Iowa.

VII. ACKNOWLEDGEMENTS

I am deeply grateful to my major professor, Dr. Edward S. Yeung for his invaluable guidance, advice, encouragement, and above all, patience with me throughout my graduate career.

I would like to thank the members of my research group, past and present included, for providing a stimulating and yet congenial environment. Space would not allow me to list their names individually. To each of them, I say, "Thank you for the good times, but, even more so for the not so good ones!" Special note of thanks must go to Don Bobbitt for gamely doing the tedious and yet necessary chore of proofreading this manuscript.

I also wish to thank the many friends that I have made during my stay in Ames. Their friendship and company have provided me with a healthy balance against the rigor of my academic pursuit.

Finally, I am eternally grateful to my parents and members of my family back home in Hong Kong. Their support and understanding have helped me through some of the bleak moments throughout my entire educational venture in this country.

VIII. APPENDIX: COMPUTER PROGRAMS USED

This appendix contains listings of the computer programs used for the dual-beam Fabry-Perot experiment in Chapter 4. The overall function of the master program (DG2) plus the subroutines, (LOC, FIND, S1) is to generate a linear ramp which, upon amplification by a high voltage operational amplifier, will scan the interferometer. For each step in the ramp, the output of each photomultiplier tube is digitized and stored in the computer. After each scan, the computer locates the constructive interference peaks at each phototube. The free spectral range of the interferometer is adjusted so that there is always one peak but never more than two peaks per scan for each beam. An algorithm is used to monitor the difference in the two beams. Two time delays (D1, D2) are incorporated into the master program for reasons stated in the text. The difference in the two beams for the first scan is compared to that of the second scan. The net result (IDIF) is displayed as digitized values.

```
      COMMON NC(3,3100),LOC(3,3),NUM,RANGE
      INTEGER FSR,RANGI
      EXTERNAL IADC
      ITOS= 10000
10    CALL SCAN(N)
      RANGE=1600
      WRITE (5,11)
11    FORMAT (' START ')
      READ (5,1) D1,D2,ICHAN
1     FORMAT (2F5.0,I5)
3     CALL SCAN(N)
      CALL LOCATE
      FSR=LOC(1,2)+LOC(1,1)
      RANGE=FSR*100
      INIT=LOC(2,1)+LOC(1,1)
      WRITE (5,9) INIT,FSR
9     FORMAT (2(1X,I6))
      CALL IADC(ICHAN,IOUT)
      WRITE (5,2) IOUT
      IF (IOUT.GT.3000) GO TO 2
      GO TO 8
      ISTART=IADC(2)
      IF (ISTART.GT.3000) GO TO 3
      GO TO 7
      ICNT=0
      CALL SETDC(4,0,01,ICNT)
      CALL LWAIT(ICNT,0)
      CALL SCAN(N)
      CALL LOCATE
      IF (NUM.EQ.0) GO TO 4
```

```
      NEW1=LOC(2,1)-LOC(1,1)
      IDEL1=NEW1-INIT
      IF (IDEL1.GT.1000) IDEL1=IDEL1-FSR
      IF (-IDEL1.GT.1000) IDEL1=IDEL1+FSR
      IPOS1=IPOS+IDEL1
      WRITE (5,5) IPOS1,IDEL1,INIT,FSR,NUM,LOC(1,1),LOC(2,1)
5     FORMAT (7(1X,I6))
      ICNF=0
      CALL SETR(4,0,02,ICNF)
      CALL LWAIT(ICNF,0)
      CALL SCAN(N)
      CALL LOCATE
      IF (NUM.EQ.0) GO TO 6
      FSR=(FSR+LOC(1,2)-LOC(1,1))/2
      RANGE=FSR+100
6     NEW2=LOC(2,1)-LOC(1,1)
      IDEL2=NEW2-INIT
      IF (IDEL2.GT.1000) IDEL2=IDEL2-FSR
      IF (-IDEL2.GT.1000) IDEL2=IDEL2+FSR
      IPOS2=IPOS+IDEL2
      WRITE (5,5) IPOS2,IDEL2,INIT,FSR,NUM,LOC(1,1),LOC(2,1)
      IDIF=IPOS1-IPOS2
      WRITE (5,7) IPOS1,IPOS2,IDIF,01,02
7     FORMAT (3(1X,I6),2(1X,F7.6))
      GO TO 10
      END
```

```
.TYPE LOC.FOR
      SUBROUTINE LOCATE
      COMMON N(2,2100),LOC(2,2),NUM,RANGE
      INTEGER RANGE
      NUM=0
      DO 40 I=1,2
      N1=21
      N2=2027
      CALL FIND (N1,N2,I,NN)
      IF ((NN-RANGE).LE.0) GO TO 20
      N1=NN-RANGE
      N2=N1+200
      LOC(I,2)=NN
      LOC(I,1)=NN
      CALL FIND (N1,N2,I,NN)
      IF (NN.LT.30) GO TO 40
      IF (I.EQ.1)NUM=1
      LOC(I,1)=NN
      GO TO 40
20    IF ((NN+RANGE).GT.2047) GO TO 30
      N2=NN+RANGE
      N1=N2-200
      LOC(I,1)=NN
      CALL FIND (N1,N2,I,NN)
      IF (NN.GT.2027) GO TO 40
      IF (I.EQ.1)NUM=1
      LOC(I,2)=NN
      GO TO 40
30    LOC(I,1)=NN
40    CONTINUE
      RETURN
      END
```

```
        ;S1.MAC
        .GLOBL SCAN
        .NCALL ..V2...,.REGDEF
        ..V2..
        .REGDEF
        .NCALL .EXIT
        STATUS = 170400
        BUFFER = 170402
        XDA = 170420
SCAN:   TST     (R5)+
        MOV     (R5)+,R0
        MOV     #4000,XDA
        MOV     #0001,STATUS
LOOP:   TSTB    STATUS
        BPL     LOOP
        MOV     BUFFER,(R0)+
        MOV     #0401,STATUS
LP:     TSTB    STATUS
        BPL     LP
        MOV     BUFFER,(R0)+
        MOV     #0001,STATUS
        INC     XDA
        MOV     XDA,R1
        SUB     #7777,R1
        BNE     LOOP
LP1:    SUB     #10,XDA
        MOV     XDA,R1
        SUB     #3777,R1
        BNE     LP1
        RTS     PC
        .END
```

```
.EDIT FIND.FOR
      SUBROUTINE  FIND(N1,N2,I,NN)
      COMMON N(2,2100),LOC(2,2),NUM,RANGE
      INTEGER RANGE
      MIN=1000
      NN=N1+100
      DO 2 II=N1,N2
      IF (N(I,II).GT.MIN) GO TO 2
      MIN=N(1,II)
      NN=II
2     CONTINUE
      RETURN
      END
```